The Impact of Molecular Adsorption on the Quantized Electronic Structure of Oxide-Supported Nanoparticles

A Model System for Heterogeneous Catalysis

Dissertation
zur Erlangung des akademischen Grades
Doctor rerum naturalium

eingereicht im
Fachbereich Physik der Freien Universität Berlin

Diplom-Physiker Christian Stiehler

Berlin, April 2015

angefertigt am Fritz-Haber-Institut der Max-Planck-Gesellschaft

Diese Dissertation wurde von November 2011 bis April 2015 in der Abteilung Chemische Physik am Fritz-Haber-Institut der Max-Planck-Gesellschaft unter der Anleitung von Herrn Prof. Dr. Hans-Joachim Freund angefertigt.

Gutachter:

1. Prof. Dr. Hans-Joachim Freund, Fritz-Haber-Institut der MPG
2. Prof. Dr. Martin Weinelt, Freie Universität Berlin

Datum der mündlichen Prüfung: 20. Juli 2015

Gold nano-catalysis reminds me of the alchemists' search for the Philosopher's stone as they tried to use it to transform base metals into noble ones. The irony of the story is that nowadays we try to use their unachieved goal (gold) as a tool to transform chemical "waste" materials such as carbon dioxide into chemically useful species such as carboxylates or oxalates.

Abstract

Electron quantization is a fundamental phenomenon that accompanies the transition from bulk metals to nanoclusters. The associated opening of an energy gap at the Fermi level crucially affects various properties of the nanostructures such as their electrical and optical behavior as well as their performance in catalytic reactions. Low-temperature scanning tunneling microscopy and spectroscopy has been employed to analyze the formation of quantum well states in two-dimensional gold nanostructures on Magnesium oxide ultrathin films, concentrating on the size regime between 50 and 300 atoms where the metal to nonmetal transition takes place.

Starting with the investigation of gold clusters with arbitrary shape, the discrete electronic structure is rationalized by simple particle-in-a-box models. Additional density functional tight-binding approaches accounting for the true atomic structure of the aggregates corroborated the experimental findings. On the basis of statistical relevant single-island experiments, general conclusions on the dependence of the energy gap on the cluster size and shape, and the real confinement potential depth are drawn.

Subsequent comparison experiments of gold nanostructures grown on thin Magnesium oxide and thick Calcium oxide films reveal the role of a permanent charge transfer into ad-particles, that is associated to an enhanced chemical reactivity of the metal-oxide systems. The excess charges primarily localize at the rim of the clusters and originate either from electron shuttling from the underlaying metal support, or by charge donation from single-ion impurities embedded in bulk-like oxides. Both processes result in the formation of charged nanoparticles with identical properties, such as pronounced electron confinement effects, monolayer island-growth and characteristic depressions in the oxide regions surrounding the particle.

Finally the impact of molecular adsorption on the quantized electronic structure of individual oxide-supported metal particles is investigated. For this purpose, isophorone and carbon dioxide, as prototype molecules for physisorptive and chemisorptive binding, were dosed onto the gold nanostruc-

tures. The molecules exclusively agglomerate at the rim of the nanoparticles in accordance to the high localization extra charges. The gold quantum well states experience distinct energy shifts upon adsorption of molecules, whereby adjacent states move apart in the carbon dioxide case but squeeze together in isophorone-covered islands. With the help of supporting infrared reflection absorption spectroscopy and density functional theory calculations the binding mechanism of both molecular entities is clearly identified and renders the investigated system as a well-suited model catalytic system to study reactions at surfaces.

Zusammenfassung

Der Übergang von metallischen Festkörpern zu Nanoclustern geht mit einer Quantisierung der elektronischen Struktur einher. Das damit verbundene Auftreten einer Energielücke am Ferminiveau beeinflusst grundlegende Eigenschaften von Nanostrukturen, wie z.B. deren elektrisches und optisches Verhalten sowie ihre Performance in katalytischen Reaktionen. In dieser Arbeit wird die Bildung von Quantentrogzuständen in zweidimensionalen Goldnanostrukturen auf ultradünnen Magnesiumoxidfilmen mittels der Tieftemperatur-Rastertunnelmikroskopie und -spektroskopie erforscht. In den Experimenten wurde sich vor allem auf das Größenregime von 50 bis 300 Atomen konzentriert, genau dort wo der charakteristische Metall-zu-Nichtmetall Übergang auftritt.

Zunächst stehen unregelmäßig geformte Goldcluster im Mittelpunkt der Forschung. In einem ersten Schritt wird die experimentell beobachtete, diskrete elektronische Struktur durch einfache Teilchen-im-Kasten Modelle angenähert. Zusätzliche Berechnungen mit einer Dichtefunktional-Tight-Binding Methode, welche die genaue Atomanordnung in den Aggregaten berücksichtig, bestätigen die experimentellen Ergebnisse. Auf der Grundlage statistisch relevanter Experimente an einzelnen Goldinseln konnten allgemeine Schlussfolgerungen sowohl zum Verhalten der Energielücke in Abhängigkeit von der Clustergröße und -form als auch zur wahren Tiefe des Potenzialtopfes getroffen werden.

Anschließende Experimente vergleichen Goldnanostrukturen auf dünnen Magnesiumoxid- und dicken Calciumoxidfilmen und identifizieren die Rolle eines permanenten Ladungstransfers in die Cluster. Der Ladungsfluss ist für eine erhöhte chemische Reaktivität der Metall-Oxid Systeme verantwortlich. Die Überschussladungen lagern sich vorrangig am Rand der Cluster an und resultieren entweder aus dem darunter befindlichen Metallträger oder aus elektronenreichen Dotanden in volumenähnlichen Oxiden. Beide Prozesse führen zur Bildung von geladenen Nanopartikeln mit identischen Eigenschaften, wie z.B. ausgeprägten Quantisierungseffekten, Monolagen-Inselwachstum und dem Auftreten charakteristischer Mulden im Oxidbereich um die Cluster.

Im letzten Teil der Arbeit werden die Auswirkungen von molekularer Adsorption auf die quantisierte elektronische Struktur in individuellen, oxidgetragenen Metallpartikeln erforscht. Zu diesem Zweck wurden Isophoron und Kohlendioxid, als zwei Prototypmoleküle für Physisorption und Chemisorption, auf die Goldpartikel adsorbiert. Die Moleküle lagern sich, in Übereinstimmung mit der erhöhten Lokalisierung von Zusatzladungen, ausschließlich am Rand der Nanoteilchen an. Die Quantentrogzustände weisen eine charakteristische Energieverschiebung unter der Adsorption von Molekülen auf, wobei im Kohlendioxidfall benachbarte Zustände auseinander driften, während sich die Zustände im Isophoronfall verdichten. Mit Hilfe zusätzlicher Infrarot-Reflexions-Absorptions-Spektroskopie und Dichtefunktionaltrechnungen konnten die Bindungsmechanismen der Moleküle eindeutig bestimmt werden. Die erzielten Ergebnisse identifizieren das untersuchte System als ein ideales Modellsystem zur Untersuchung katalytischer Reaktionen an Oberflächen.

List of Abbreviations

1D	One-dimensional
2D	Two-dimensional
3D	Three-dimensional
AES	Auger electron spectroscopy
AFM	Atomic force microscopy
Ag	Silver
Al	Aluminum
Au	Gold
Ca	Calcium
CaO	Calcium oxide
CB	Conduction band
C_9H_14O	Isophorone
C_2O_4	Oxalate
CO	Carbon monoxide
CO_2	Carbon dioxide
CO_2^-	Carboxylate
DBTJ	Double barrier tunneling junction
DFT	Density functional theory
DFTB	Density functional tight binding
DOS	Density of states
EELS	Electron energy loss spectroscopy
EXAFS	Extended X-ray absorption fine structure
fcc	Face centered cubic
FER	Field emission resonance
FHI	Fritz-Haber-Institut der Max-Planck-Gesellschaft
FWHM	Full width at half maximum
HOMO	Highest occupied molecular orbital
HREELS	High resolution electron energy loss spectroscopy

IETS	Inelastic electron tunneling spectroscopy
IR	Infrared
IRAS	Infrared reflection absorption spectroscopy
LEED	Low energy electron diffraction
LDOS	Local density of states
LT	Low temperature
LUMO	Lowest unoccupied molecular orbital
MIGS	Metal induced gap state
Mg	Magnesium
MgO	Magnesium oxide
ML	Monolayer
Mo	Molybdenum
NaCl	Sodium chloride
NN	Nearest neighbor
O	Oxygen
PCF	Pair correlation function
PIB	Particle-in-a-box
PSTM	Photon emission scanning tunneling microscopy or microscope
PVD	Physical vapor deposition
QWS	Quantum well states
rms	Root mean square
RFPLO	Relativistic full-potential local-orbital
RT	Room temperature
SGL	Schrödinger Equation
STM	Scanning tunneling microscopy or microscope
STS	Scanning tunneling spectroscopy
TPD	Temperature programmed desorption
UHV	Ultra-high vacuum
UPS	Ultraviolet photoelectron spectroscopy
VB	Valence band
VCB	Valence conduction band
XRD	X-ray diffraction
XPS	X-ray photoelectron spectroscopy

List of Symbols

C	Capacitance
c_λ	mean coordination number
d	Tip-sample distance
d_c	Real diameter of 3D clusters
d_c^*	Apparent diameter of 3D clusters
Δ	HOMO-LUMO energy gap
dI/dV	Differential conductance
$\delta(x)$	Delta function
E	Energy
ΔE	Energy shift
$\vec{E}$	Electric field
ϵ	Dielectric function
E_{adh}	Adhesion energy
E_F	Fermi function
E_0	Onset energy
$f(E)$	Fermi function
h_c	Real height of 3D clusters
$\hbar$	Reduced Planck constant
γ	Surface free energy
Γ	Tunneling rate in a double barrier tunneling junction
I_T	Tunneling current
J	Quantum mechanical tunneling current
k, κ	Wave vectors
l	Angular momentum
L	Length
λ	Wavelength or decay parameter
m	Mass

m_{eff}	Effective electron mass
M_{ij}	Tunneling matrix element between states i and j
n	Quantum number
q	Charge distribution
r	Radius
r_0	Position of the tip
r_t	Radius of spherical tip
R	Resistance
rho_s	Sample electronic density
$\sigma(n)$	Ensemble distribution of electrons
T	Temperature or Transmission coefficient
T_{ij}	Transmission rate between states i and j
U	Bias
ΔU	Bias shift
V	Potential or bias
$\hat{V}$	Perturbation operator
V_0	Potential height
V_{mod}	Modulation bias
V_{pp}	Peak-to-peak voltage
V_s	Sample bias
ΔV	Total peak width
ΔV_i	Intrinsic peak width
ΔV_T	Thermal peak broadening
$\Delta V_{V_{mod}}$	Peak broadening due to modulation bias
ψ	Wave function

Contents

Chapter 1

Introduction

Small metal particles on oxide surfaces are pivotal elements in heterogeneous catalysis as they serve as active centers in catalytic reactions [1–4]. For instance small gold particles no larger than 3 to 4nm deposited onto titania show a high catalytic reactivity for interesting chemical reactions as e.g. the carbon monoxide (CO) oxidation to carbon dioxide (CO_2) already at room temperature (RT) [5, 6]. The investigation of such systems is very difficult because the metal clusters exhibit their highest reactivity in the so-called "non-scalable" size regime [7, 8], where the physical properties are very sensitive to the atom number and change drastically by adding one atom to the nanostructure. The non-scalable regime is also the range in which the interesting metal to non-metal transition takes place. By reducing the number of atoms in a metal to a few hundreds, the periodic band structure breaks down and the electronic structure develops into a set of quantized discrete states, the so-called quantum well states (QWS) [9–11]. Those states are no longer defined by distinct wave vectors, as the translational symmetry of the system is lost [10, 12–14].

The new geometry and specific electronic properties of the metal particles arising from their limited spatial dimensions lead to a distinct chemical and adsorption behavior. The large number of low-coordinated atoms in the nanostructures results in a different binding behavior for molecules as compared to compact surfaces. For instance the development of van-der-Waals forces, which result from the spontaneous polarization of atoms or molecules, is reduced in smaller cluster as the number of polarizeable units reduces. On the other hand, the creation of stable, covalent bonds with adsorbates is favored in smaller clusters due to the lower coordination number of their surface atoms. Another example for the distinct chemical properties is the possible communication between different cluster facets, owing to the reduced distances of neighboring facets in smaller clusters and hence the enhanced ability for

moving adsorbates between the facets [15].

Besides the intrinsic particle properties, substrate effects play a major role for the catalytic reactivity. Up to now, clusters have been mostly investigated in gas phase experiments concentrating mainly on size-selected clusters with less than 100 atoms. In this regime, a mass selection is possible with acceptable yields and ensemble effects can be neglected [16, 17]. However, the gas phase situation is unrealistic because substrates play a decisive role in all chemical applications. It is therefore important to investigate clusters in combination with substrates and particularly with oxide substrates. For instance the cluster geometry and charge state depend on the interaction of the cluster with the substrate [18–22]. Moreover, the small metal particles try to adopt the symmetry of the oxide support in order to interact in an optimum way with the substrate.

For the investigation of nanoparticles and molecular adsorption on them exist in general two experimental approaches: local and non-local ones. Non-local surface science techniques include infrared reflection absorption spectroscopy (IRAS) and electron energy loss spectroscopy (EELS), used to measure the vibrational modes of molecules on surfaces and to identify their binding sites [23]. With temperature programmed desorption (TPD) and calorimetric techniques adsorption/desorption energies of adsorbates can be measured [24–26]. The usage of electronic methods, as x-ray photoelectron spectroscopy (XPS/UPS) gives only statistical informations while x-ray diffraction (XRD) is limited to crystalline surfaces [27–29]. All these techniques have in common that they average over a macroscopic area of the sample surface, i.e. above millions of clusters, and they are not suitable to eliminate ensemble effects as the cluster size and shape distribution. Hence the individuality of clusters gets lost. Therefore, it is of utmost importance to use local surface science approaches for the investigation of metal clusters and their interaction with molecules. Prominent examples are scanning probe techniques such as scanning tunneling microscopy (STM) [30, 31] or atomic force microscopy (AFM) [32], and scanning electron microscopy [33]. Thereby, the investigated sample surface is scanned and imaged at the sub-nanometer length scale either with the help of the quantum mechanical tunneling current or a focused electron beam, respectively, and structural and electronic information of local surface areas are gained [34].

Those local approaches are not appropriate for real catalysts that comprise an oxide support with very inhomogeneous properties. However, these local approaches are well suited for catalytic model systems. Especially clusters on thin oxide films brought onto a metal substrate are suitable as (catalytic)

model systems [3, 35–42]. Usually, the thin oxides are insulators and decouple the cluster from the metal substrate. Nonetheless charges can be transfered from the underlying metal to the cluster in three ways. First, free electrons from the substrate can tunnel through the oxide into the cluster as it is the case for gold (Au) particles on magnesium oxide (MgO) ultrathin films grown on a silver Ag(001) support [18]. Second, oxygen vacancies in the oxide layers, being generated by reduction reactions, can supply electrons to be transferred into the cluster [43, 44]. A last possibility is charge donation from self-doped single-ion impurities embedded in bulk-like oxides as for instance from molybdenum donors in calcium oxide (CaO) on a molybdenum Mo(001) support [21, 22]. Here, charge transfer from the doped oxide is enough to activate oxygen molecules on the surface [45]. By combining the three tools — model systems *plus* metal particles *plus* a local methodology — the working principle of catalysts can be determined by putting special emphasis on the size and shape dependence of chemical reactivity; and chemical activation of molecules.

This thesis aims to go one step closer to a real catalytic reaction and focuses on the adsorption of molecules onto a model catalytic system and the associated change of the electronic structure. Thereby, the following questions have tried to be answered: Can molecules be chemically activated on supported metal particles in order to use them for chemical reactions? What is the binding mechanism behind this process and is there a charge transfer involved? What is the impact of adsorption on the electronic structure of the quantum systems? For this purpose, Au clusters have been deposited onto MgO ultrathin films grown on Ag(001). Already in the past, this material system has been subject to various catalytic research projects as it is the prototype model for heterogeneous catalysis. This was expressed by Prof. Joachim Sauer from the Humboldt University Berlin who stated "...MgO is for surface science what the hydrogen atom is for atomic and molecular physics..." [46]. The key role arises from its simplicity, which helps generating theoretical models, and its comparability to experiments. Two main objectives were addressed in the thesis. Firstly, to check whether the electronic structure in the Au nanoparticles changes upon molecular adsorption. Secondly, whether it is possible to chemically activate CO_2 at the Au nanoparticles and in this way, transforming this stable molecule into useful chemicals. This goal is of high economical, environmental and political relevance because in this way the in abundance existing greenhouse gas can be reduced.

The organization of the thesis is as follows: In a first step, gold clusters with arbitrarily shape have been prepared on the MgO/Ag(001) ultrathin film. After controlling the film quality, the influence of the cluster size and

shape on their electronic properties and hence, on the catalytic reactivity, has been analyzed (chapter 4). In chapter 5 two charging mechanisms of gold nanostructures on oxide surfaces are investigated, which are (i) electron tunneling through ultrathin MgO layers on a Ag(001) support and (ii) charge donation by single-ion impurities embedded in bulk-like CaO/Mo(001) oxides. In both cases excess charges get transfered to the clusters leading to their two-dimensional (2D) growth and an improved catalytic activity. The last and most important experiments shown in chapter 6 deal with molecular adsorption on the with Au nanoparticles-adsorbed MgO/Ag(001) ultrathin film by means of weakly bound isophorone and chemisorbed CO_2. Subsequently, a decisive and different change of the electronic structure of the Au clusters was observed. In combination with IRAS measurements and density functional theory (DFT) calculations the activation of CO_2 molecules at the nanostructures was shown and the binding mechanism of both molecules has been identified.

Chapter 2

Methods and Experimental Setup

This chapter gives a short introduction to the applications of a scanning tunneling microscope (STM) regarding the presented work. For a detailed overview over the broad range of capabilities of the STM the reader is referred to the wealth of literature which can be found e.g. in [17, 47–49]

2.1 Scanning Tunneling Microscopy

2.1.1 Introduction

Based on the phenomena of the quantum mechanical tunneling, G. Binning and H. Rohrer invented the STM in 1982 [50] for which they were awarded the Nobel prize in physics only four years later in 1986. This technique permits the investigation of geometrical and electronic properties of surfaces with a very high spatial resolution at the atomic scale. Further developments have led to STM-based spectroscopic methods which allow for local studies of sample properties. Fascinating examples are scanning tunneling spectroscopy (STS), [51], inelastic electron tunneling spectroscopy (IETS) [52] and photon emission scanning tunneling microscopy (PSTM) [53–56]. STS and differential conductance (dI/dV) mapping reveal the local density of states (LDOS) of surfaces and adsorbates on surfaces and are used, for instance, to determine surface states [57] and interface states [58], band gaps of semiconductors and insulating thin films [51, 58, 59] or to visualize the discrete electronic structure of atoms and clusters on surfaces [10, 60, 61]. These results represent a direct confirmation of basic principles in quantum mechanics [62–67]. IETS provides vibrational spectra of single adsorbed molecules on surfaces or on clusters on

surfaces [52, 68–70] which are not obtainable otherwise. Since molecules are characterized uniquely by their vibrational spectra, the measurement of IETS spectra represent a reliable possibility to characterize molecules on surfaces. PSTM is carried out with a special photon STM and is used to investigate optical properties of surfaces as plasmon resonances of single metal clusters [56] or exciton mediated [71] photon emission from semiconductors and oxide surfaces [72] and supported molecules [73, 74]. The emitted light gives information about the interplay between morphology, defect structures, adsorption and the optical properties of surfaces. By operating a STM in external magnetic fields with appropriate tips, spin-polarized tunneling and mapping of magnetization are possible [75–77]. A further key feature of the STM is the possibility of manipulating single atoms and molecules, a technique with high potential in the emerging research field of molecular electronics [67, 78, 79].

2.1.2 Principle and Theoretical Description

Electron tunneling is determined by the electronic density of states (DOS) of the tip and the sample but also depends on the sample bias V_s, the distance d between tip and sample and the tip shape. Fig. 2.1 shows a scheme of a STM setup. It consists of a metallic tip that is brought into a distance d to a conductive sample surface. The working principle is based on the quantum-mechanical tunneling, i.e. electrons can overcome a finite energy barrier even if their potential energy is less than the height of the barrier. In practice this barrier consists of the vacuum distance between the metallic tip and the conductive sample, i.e. the width as well as the height of the barrier. If a voltage V_s is applied between tip and sample a tunneling current I_T flows between tip and sample. I_T decreases exponentially with the distance d. For typical distances d of a few angstrom a typical tunneling current I_T from a few picoampere to some nanoampere is detected. Such small absolute distances and controlled vertical and lateral displacements of the tip can be achieved with piezo ceramics. A possible arrangement of piezo ceramics is shown in Fig. 2.1 (others exist). Here, the so called z-piezo is responsible for the height adjustment whereas the x- and y-piezos regulate the scanning of the surface area. A STM can be operated in two modes. In the first one, the *constant current mode*, the tunneling current I_T is kept constant via a feedback loop and the varying distance d between tip and sample surface is detected by the *z-piezo* during the scanning process. This is the preferred STM operation mode because it avoids crashes of the tip with the sample. In the second mode, the *constant height mode*, the distance d is kept constant during scanning and

changes in I_T are measured. Using this mode makes faster scanning possible which is important for the investigation of dynamic surface processes.

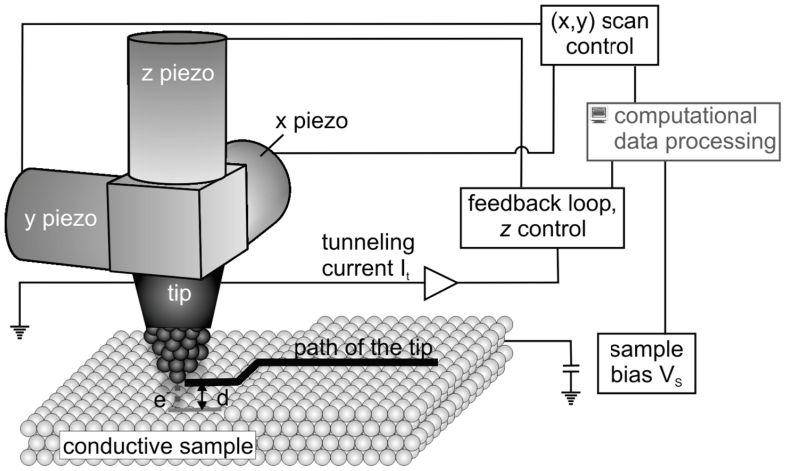

Fig. 2.1: Schematic design of a scanning tunneling microscope.

An exact theoretical description of the STM is extremely difficult due to the broken translational symmetry in the tunnel junction and the variety of unknown factors contributing to the non-equilibrium conditions. Therefore, the following gives only an initial idea of the tunneling process and the reader is referred to further literature for a deeper understanding of the STM [47, 48, 80, 81]. Furthermore, each description of electron tunneling has to distinguish between elastic and inelastic processes. In the first case, the energy of the electron is conserved and thus equal before and after the tunneling process. In the second case the electron gains or looses energy due to excitations in the gap such as plasmonic or phononic excitations. In the following, only the case of elastic electron tunneling is considered.

In order to introduce the basic idea of electron tunneling, we start from the idealized case of one electron with the energy E and the mass m penetrating through a rectangular, one-dimensional (1D) potential barrier with the height $V_0 > E$ and the width d as it is shown in Fig. 2.2. The time-independent Schrödinger equation that describes the system is

$$\left[\frac{\hbar^2}{2m} + V(x)\right]\psi(x) = E\psi(x) \ . \tag{2.1}$$

Here, $\psi(x)$ is the wave function of the electron, $\hbar$ is the Planck constant and

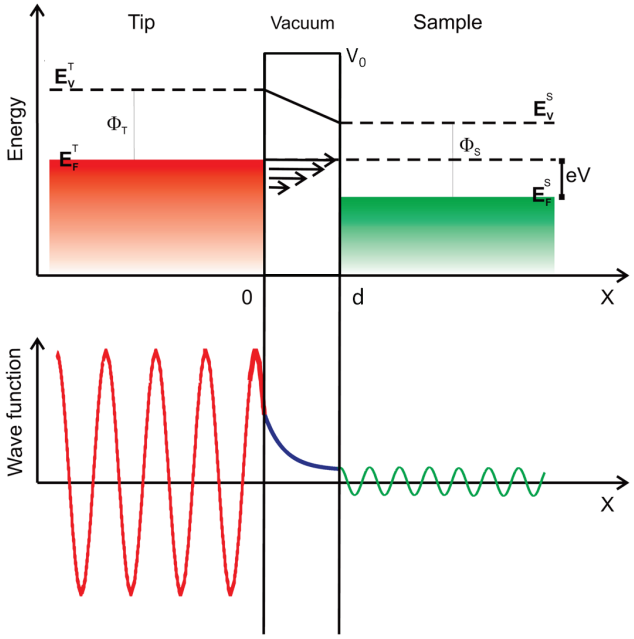

Fig. 2.2: Scheme of an 1D tunneling process. Figure taken from ref. [82].

$V(x)$ is the potential:

$$V(x) = \begin{cases} 0 & \text{for } x \notin [0, d] \\ V_0 & \text{for } x \in [0, d] \end{cases} \tag{2.2}$$

The wave functions that solve equation 2.1 have the form (not normalized)

$$\psi(x) \propto \begin{cases} e^{\pm ikx} & \text{for } x \notin [0, d] \\ e^{\pm \kappa x} & \text{for } x \in [0, d] \end{cases} \tag{2.3}$$

with the wave vectors

$$k(x) = \sqrt{\frac{2mE}{\hbar^2}} \tag{2.4}$$

and

$$\kappa(x) = \sqrt{\frac{2m(V_0 - E)}{\hbar^2}} \tag{2.5}$$

in the respective regions. The incoming wave function is partly reflected at the potential barrier and partly transmitted through the barrier. In order to

ensure that the wave function is continuously differentiable everywhere, the solutions of the Schrödinger equation and their derivatives have to be equal at the points $x = 0$ and $x = d$. The transmission coefficient T through the barrier is the quotient of the transmitted and the incident current density and can be written as [48]:

$$T = \frac{1}{1 + \frac{V_0^2 \sinh^2(\kappa d)}{4E(V_0 - E)}} \tag{2.6}$$

In the limit of large barriers $\kappa d >> 1$, expression 2.6 simplifies to the following.

$$T = \frac{16E(V_0 - E)}{V_0^2} e^{-2\kappa d} \tag{2.7}$$

The transmission coefficient T depends exponentially on the barrier width d which is a typical feature for electron tunneling independent of the actual barrier shape.

Many approaches for the tunneling process through a three-dimensional 3D potential barrier refer to a theoretical description by Bardeen [83]. There, he described the electron tunneling in a layered junction, consisting of metal and superconductor separated by a thin insulating film, as a many body problem with the time-dependent perturbation theory of first order. As Bardeen pointed out, his theory "...can also be used for calculating the tunneling current between the valence and conduction bands of a semiconductor, as observed in the Esaki diode..." [83]. The two electrodes are considered to be independent from each other with known eigenfunctions. The electron tunneling between the two electrodes is described as a transition from an initial state $|i\rangle$ to a unperturbated final state $|f\rangle$. The constant, energy-independent transition rate T_{if} between the two states is obtained by applying Fermi's Golden Rule

$$T_{if} = \frac{2\pi}{\hbar} |\langle f|\hat{V}|i\rangle|^2 \delta(E_i - E_f) \tag{2.8}$$

with $\hat{V}$ as the perturbation operator. By integration over the full energy interval, equation 2.8 can be written as

$$T_{if} = \frac{2\pi}{\hbar} |M_{if}|^2 \rho_f \tag{2.9}$$

with ρ_f as the energy density of the final states. $M_{if} = \langle f|\hat{V}|i\rangle$ is the tunneling matrix element between the initial state $|i\rangle$ and the final state $|f\rangle$ which are

described by the wave functions ψ_i and ψ_f, respectively. The absolute square value of the tunneling matrix elements $|M_{if}|^2$ gives the transition probability from $|i\rangle$ to $|f\rangle$. According to Bardeen, M_{if} is the quantum mechanical current operator:

$$M_{if} = \frac{\hbar^2}{2m} \int_S d\vec{S} \left(\psi_i^* \vec{\nabla} \psi_f - \psi_f \vec{\nabla} \psi_i^* \right) \tag{2.10}$$

with the integral over the surface S lying entirely within the vacuum barrier separating the two electrodes. The quantum-mechanical current J_i flowing between $|i\rangle$ and $|f\rangle$ is the product of the electron charge e and T_{if}: $J_i = e \cdot T_{if}$ [84]. In order to get the total tunneling current I_T, one has to sum over all states i,f with the same energy and consider the Fermi distribution. From equation 2.8 one obtains the following expression for the tunneling current I_T [83]

$$I_T = \frac{2\pi e}{\hbar} \sum_{i,f} f(E_i) \left[1 - f(E_f + eV_s) \right] |M_{if}|^2 \delta(E_i - E_f) \tag{2.11}$$

where $f(E)$ is the Fermi function, V_s the applied voltage and E_i is the energy of the state $|i\rangle$ in absence of tunneling. The delta-function δ maintains the conservation of energy for elastic tunneling processes.

Tersoff and Hamann extended Bardeen's theory to the specific case of the STM. The initial states are represented by the tip and the final states are located in the sample surface. In the limit of small applied voltages ($V_s \to 0$) and low temperatures ($T \to 0$), where the Fermi function has a step-like shape and only energy levels near the Fermi energy E_F are important, equation 2.12 simplifies to following expression. (Note the change of inidices $i \to t$ (tip) and $f \to s$ (sample).)

$$I_T = \frac{2\pi e}{\hbar} e V_s \sum_{t,s} |M_{ts}|^2 \delta(E_s - E_F) \delta(E_t - E_F) \tag{2.12}$$

V_s is the applied sample bias, E_s and E_t the energy of the unperturbed sample and tip states, respectively. In general, the structure and therefore the wave functions of the tip-apex are not known which makes the calculation of the tunneling matrix elements M_{if} impossible. Therefore, Tersoff and Hamann assumed the tip to have a locally spherical potential which means a s-wave symmetry [80, 81]. In this way they could calculate the transition matrix elements and show that the tunneling current is proportional to the LDOS

of the sample ρ_s at the tip position r_0 and near the Fermi level for small tunneling bias.

$$I_T \propto eV_s\rho_s(r_0, E_F) \tag{2.13}$$

The main restriction of their model is the limitation to tips with s-wave character which means an angular momentum $l = 0$. Regardless of the broad application of the model it fails for instance to correctly describe the high corrugation observed for some metal surfaces [47]. Therefore further models have been developed considering p_z and d_{z^2} states of the tip which enabled a better description of STM images [47, 84].

2.1.3 Tunneling Through Thin Oxide Films

Many oxides are insulators. They are characterized by sometimes large energy gaps of 3 to 5 eV between the filled valence band (VB) and the unoccupied conduction band (CB), with the Fermi level E_F lying in between the two bands. If insulators are exposed to electrons they tend to charge due to their dielectricity and electron tunneling cannot be observed. In general, oxide materials are only suitable for STM investigations if the dielectric sample charging can be avoided and the electronic conductivity is sufficiently high in order to overcome the band gap. This condition is fulfilled for bulk oxides at elevated temperatures [85, 86] or for bulk conductive materials as titania [87] where the electronic conductivity arises from defects. In order to enable tunneling in oxides with wide band gaps they can be grown as thin films on conductive substrates [59, 88, 89]. In this situation, charging of the oxide can be avoided if the electrons overcome the oxide barrier with a sufficiently high probability. This implies that the film thickness is limited to a few monolayers (ML). The influence of the film thickness on electronic and imaging properties has been studied systematically for several systems, e.g. for sodium chloride (NaCl) films on aluminum Al(111) and Al(100) [90] and for MgO films on Ag(001) [58] and on Mo(001) [91]. According to the results, band gaps as large as in the corresponding bulk oxide are already reached for film thicknesses of 2-3 ML. These thin films are still conductive and can often be imaged with atomic resolution [92]. Nonetheless, a detailed theoretical description of tunneling processes on thin oxide films is still missing.

Fig. 2.3 shows the scheme of a tunneling junction of a thin oxide layer on top of a metal substrate. It consists of two electrodes, a metallic tip and a metal substrate, which are separated by two barriers, the vacuum and the thin oxide film. The oxide layer can be considered as perfect dielectric which means

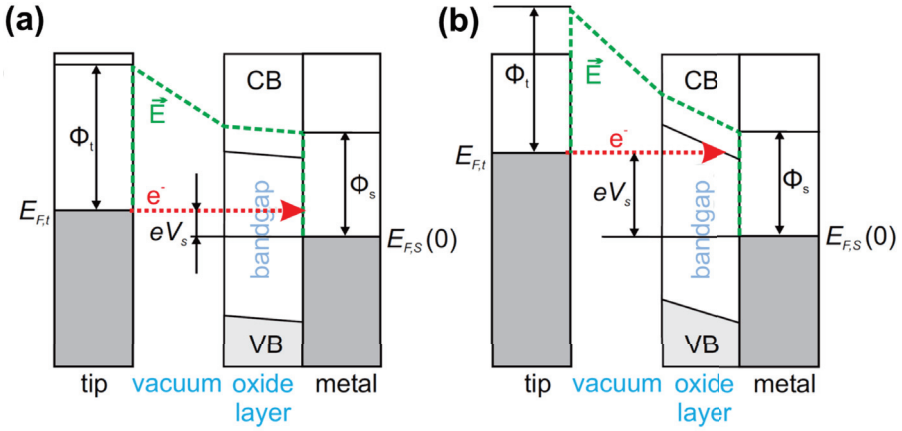

Fig. 2.3: Energy scheme of a tunneling junction for thin oxide films on a metal substrate. The tunneling barrier consist of the vacuum barrier and the oxide layer. Figure modified from ref. [93].

that the absolute value of the electric field $\vec{E}$ can be estimated as the ratio between voltage drop in the oxide and film thickness, normalized by the oxide dielectric function ϵ. The field therefore depends linearly on the sample bias V_s across the layer [94]: $|\vec{E}| \propto V_s/d$. The reduction of the electric field results in a bending of the valence band (VB) and conduction band (CB) of the oxide towards the Fermi level of the tip (Fig. 2.3) [95–97]. Phenomenologically, two different scenarios of electron tunneling can be distinguished. Firstly, if the scanning bias is chosen within the oxide band gap close to the Fermi level of the metal substrate $E_{F,s}$ as shown in Fig. 2.3 (a), oxide states do not contribute to the tunneling current and the STM is only sensitive to states of the metal substrate and the metal-oxide interface. This assumption seems to be supported by the observed reduction of the apparent thickness of oxide films for small biases [98]. Secondly, if V_s is chosen outside the oxide band gap, as shown in Fig. 2.3 (b), oxide states are directly accessible by STM and the apparent height of the film is in the range of the real film thickness [98]. Usually, no atomic resolution can be obtained under these tunneling condition because of the large distance between tip and sample.

2.1.4 Tunneling Through Oxide-Supported Metal Clusters

3D metal clusters on thin oxide films can be considered as adsorbates with a large corrugation. Due to the fact that STM images represent a convolution of geometric and electronic tip and sample properties, the tip shape strongly

influences the apparent lateral size of adsorbates on the surface and an extraction of geometrical parameters has to be done carefully. The tip convolution effect is schematically shown in Fig. 2.4 for 3D metal clusters with a (a) hemispherical and a (b) prism shape. The real cluster diameter d_c is not imaged

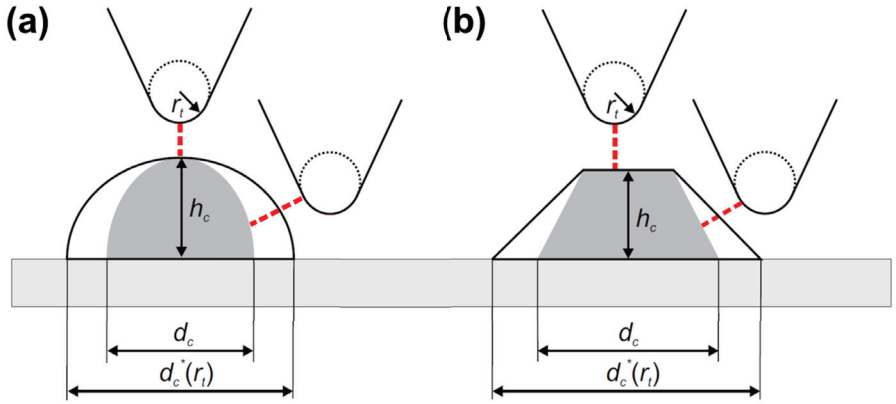

Fig. 2.4: Scheme of the tip convolution effect when tunneling on oxide-supported (a) hemispherical and (b) prism-shaped metal cluster. The cluster height can be measured reliably but the apparent cluster size deviates from the real one. Figure taken from ref. [93].

correctly because electrons tunnel from different parts of the tip depending on where the tip is placed with respect to the cluster center. Thus, the apparent cluster diameters d_c^* measured by STM depend on the tip radius r_t (assuming a spherical tip geometry at the edge). The exact knowledge of d_c is often essential for e.g. a proper description and understanding of the electronic properties of clusters. However, the tip radius r_t is usually unknown which makes the corrections of the measured cluster diameters d_c^* often difficult and imprecise. One possibility is to compare the amount of deposited metal with the amount determined from STM images. In this case clusters are assumed to have the same shape and the volume is calculated by using the measured values h_c and d_c^*. The correction factor $g = \frac{d_c}{d_c^*}$ can be determined by comparing the apparent and real metal coverage. Contrary to the determination of the cluster diameters the cluster height h_c can be determined without problems. As it is seen in Fig. 2.4 if the tip is placed above the clusters, the tunneling process takes place only between the lowest part of the tip and the highest part of the cluster and is happening directly. However, h_c is bias dependent for substrates with a band gap [98] as it is the case for most thin oxide films. Therefore, the sample bias has to be chosen outside the band gap in order to measure h_c correctly.

2.2 Scanning Tunneling Spectroscopy

Keeping the tip of a STM at a fixed position over the surface and sweeping the bias voltage, one can record the I-V characteristics. This technique is called synonymously scanning tunneling spectroscopy or dI/dV spectroscopy. The first derivative of the current to the voltage dI/dV gives information about the LDOS of the substrate, assuming that the tip has a featureless DOS. Differentiating equation 2.13 with respect to the sample bias leads to following expression. (Note the change of indices: $I_T \rightarrow I$, $V_s \rightarrow V$.)

$$\frac{dI}{dV} \propto e\rho_s(r_0, E_F) \tag{2.14}$$

The differential conductance dI/dV is direct proportional to the LDOS of the sample ρ_s at the position of the tip r_0. Therefore, it is an ideal technique to measure the local electron distribution at surfaces and in surface near regions. A weak point of STS is that it is not possible to accomplish angle-resolved studies since this techniques has no resolution in the complete k-space as the component perpendicular to the surface cannot be measured. Furthermore, it is limited to those states only, that extend sufficiently into the vacuum. Hence, it is often difficult to study occupied states which are more contracted than unoccupied ones.

Experimentally, various modes have been proposed to measure the differential conductance. All of them have in common, that they use a lock-in-amplifier, which adds a small modulation voltage V_{mod} to the sample bias to detect the conductance. This technique was established first by Feenstra et al. [51]. The difference in various STS operation modes concerns the adjustment of the tip-sample separation, which can be kept constant [51] or varied in a specific way (linear ramp, constant gap resistance, constant current). Advantages and disadvantages inherent to each method can be found for instance in ref. [59]. All dI/dV spectra presented in this work re recorded with disabled feed-back loop at constant tip-sample distance. This permits to take spectra across the Fermi level $E_F = V_s = 0$. The lock-in amplifier was typically operated with a small modulation bias between 10 and 30 mV root mean square (rms) value, and typical modulation frequency around 1 kHz.

An important point to consider when using STS is the spectral resolution. The experimental peak width ΔV consists of mainly three components. These are the intrinsic peaks width ΔV_i, the peak broadening due to finite temperature ΔV_T and due to a bias modulation $\Delta V_{V_{mod}}$ [99–101]. The total peak

width ΔV is calculated as follows [93, 102]

$$\Delta V = \sqrt{(\Delta V_i)^2 + (\Delta V_T)^2 + (\Delta V_{V_{mod}})^2} \tag{2.15}$$

whereby each width corresponds to the full width at half maximum (FWHM) of the individual contributions. ΔV_i is mainly determined by the natural line width and by tip-induced broadening [103, 104]. The influence of the latter factor can be estimated by comparing spectra recorded with different tips. The thermal broadening ΔV_T can be derived from equation 2.11 with the Fermi function $f(E) = [\exp(E - E_F/k_BT) + 1]^{-1}$ reflecting the energy distribution at a finite temperature T. The derivative dI/dV can be approximated by a Gaussian distribution with a FWHM of $2\sigma = 3k_BT/e$ [105] which leads to the following expression.

$$\Delta V_T = 3k_BT/e \tag{2.16}$$

Considering the working temperature of the microscope (5 K) in equation 2.16, it results in a negligibly small thermal broadening of $\Delta V_T = 1.3\ mV$. From an analysis of the amplifier signal as demonstrated in [106], one gets a FWHM of the broadening function of around 0.87 V_{pp}, whereby V_{pp} is the peak-to-peak voltage of the modulation. This corresponds to a rms-value of $2 \cdot 0.87\sqrt{2}V_{mod} \approx 2.5V_{mod}$ and hence:

$$\Delta V_{V_{mod}} = 2.5 \cdot V_{mod} \tag{2.17}$$

Typical modulation voltages used in the following work are between 10...30 mV, which lead to a peak broadening of 25...75 mV. The total peak broadening is therefore

$$V = \sqrt{(\Delta V_i)^2 + (3k_BT/e)^2 + (2.5V_{mod})^2} \tag{2.18}$$

and arises mainly from the intrinsic peak width and the modulation voltage leading to the experimental peak width in our system of typically 500 meV.

2.3 Conductance Imaging

Conductance imaging or alternatively conductance mapping consists of scanning a certain surface area and recording the dI/dV value at each point at one specific bias. This results in a map of the LDOS of the surface. Experimentally, a small modulation voltage of about 30 mV is added to the chosen sample

bias and the dI/dV value is detected via a lock-in-amplifier. The sample bias is kept constant and the feed-back loop closed during the scanning process which enables the recording of constant current topographic and dI/dV images simultaneously. A main application of this method is the investigation of standing wave patterns resulting from electron confinement on terraces, artificial quantum structures, clusters or islands [14, 62, 63, 66, 67, 107, 108]. Furthermore, dI/dV mapping is a valuable technique to study the electronic structure in the environment of local defects (point or line defects) or adsorbates on the surface [109, 110].

2.4 Coulomb Blockade and Coulomb Staircase

When electron tunneling is performed on oxide supported metal clusters, the effect of Coulomb charging or Coulomb blockade plays an important role. Fig. 2.5a shows a cartoon of a typical tunneling junction consisting of two barriers between tip and substrate, the vacuum and the insulating oxide film. Each of the barriers in this double barrier tunneling junction (DBTJ) can be represented by a combination of a capacitance C_i and a resistance R_i (Fig. 2.5b). Furthermore, three electrodes are depicted in the electric circuit: (i) the tip, (ii) the metal cluster and (iii) the metal support. The Coulomb blockade or Coulomb staircase [112, 113] refers now to modifications of the tunneling curves $I_T(V)$ which occur in DBTJs with sufficiently low capacitances, so that the charging energy of a single electron when entering the central electrode is large enough to play a major role in the tunneling process. If the electrostatic

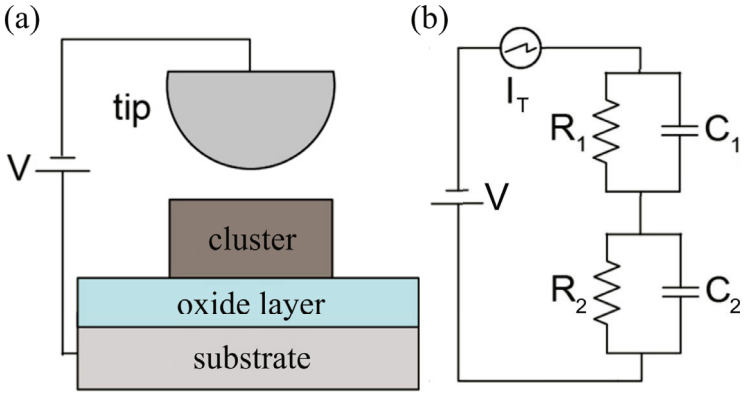

Fig. 2.5: (a) Cartoon of a Coulomb blockade setup consisting of a metal cluster on top of an insulating oxide film on a metallic substrate. (b) Scheme of the electric circuit for the double barrier tunneling junction with each barrier represented by a set of capacitors and resistors. Figure adapted from [111].

Coulomb energy of an electron exceeds the thermal energy, i.e.

$$\frac{e^2}{2(C_1 + C_2)} \gg k_B T \tag{2.19}$$

the number of electrons on the center electrode (metal cluster) remains unchanged for a constant bias. (Cf. Fig. 2.5: C_1 and C_2 refer to the tip-cluste and cluster-support capacitance, respectively.) When applying an external voltage V, the capacitances C_i charge up to certain threshold voltages before the tunneling process takes place. Two phenomena may result from the Coulomb charging depending on the ratios of the time constants $T_i/T_j = (R_i C_i)/(R_j C_j)$. First, if the time constants T_i for electron tunneling through the barriers are of the same order, a characteristic dip around the Fermi level is observed in the dI/dV spectrum [114] (see black, red, green curves in Fig. 2.6b). Second, if the time constants $R_i C_i$ are very different, the center electrode (metal cluster) is charged quickly to its equilibrium level by tunneling through one junction, but releases charges through the other junction comparably slow. The successive charging of the center electrode by individual electrons opens new tunneling channels and, hence, leads to an increased conductance in the DBTJ in a quantized fashion with respect to the bias and hence, to a stepwise increase of the tunneling current (see marine, blue and magenta curves in Fig. 2.6a). First experimental results regarding Coulomb blockades, gaps and staircases were observed in planar tunneling junctions in the late 1960s [115, 116]; theoretical descriptions for these nanoscopic junctions followed in the late 1980s [114, 117–119] and has been confirmed by STM measurements in the same decade [120].

In the following is given a short overview about the orthodox theory of the Coulomb blockade, a precise description can be found in [119, 121]. It is aimed to develop an expression for the tunneling current as a function of the sample bias and the tunneling rate $\Gamma_i^{\pm}(n)$ of electrons:

$$\Gamma_i^{\pm}(n) = \frac{1}{R_i e^2} \left(\frac{-\Delta E_i^{\pm}}{1 - \exp\left(E_i^{\pm}/k_B T\right)} \right) \tag{2.20}$$

with ΔE as the energy difference when an electron tunnels across the barrier. The sign, + or -, refers to electron tunneling into or from the cluster, respectively. The index i refers to the two barriers in the DBTJ (cf. Fig. 2.5). The center electrode (metal cluster) carries the excess charge Q which consists of an integer and fractional part Q_0, $Q = n \cdot e + Q_0$. The energy change in the

two barriers calculates as

$$\Delta E_1^{\pm} = \frac{e}{C_\Sigma}\left\{\left[\frac{e}{2} \pm (ne - Q_0)\right] \pm C_2 V\right\} \tag{2.21}$$

$$\Delta E_2^{\pm} = \frac{e}{C_\Sigma}\left\{\left[\frac{e}{2} \pm (ne - Q_0)\right] \mp C_1 V\right\} \tag{2.22}$$

with $C_\Sigma = \sum C_i$ being the total capacitance over the two barriers. The tunneling current is than:

$$I_T(V) = e\cdot \sum_{n=-\infty}^{\infty} \sigma(n)\cdot \left(\Gamma_2^+(n) - \Gamma_2^-(n)\right) \tag{2.23}$$

$$= e\cdot \sum_{n=-\infty}^{\infty} \sigma(n)\cdot \left(\Gamma_1^-(n) - \Gamma_1^+(n)\right) \tag{2.24}$$

$\sigma(n)$ represents the ensemble distribution of the number of electrons on the electrode. Equation 2.24 can be solved numerically considering that (i) the net probability for a transition between adjacent states is zero, i.e.

$$\sigma(n)\cdot \left(\Gamma_1^+(n) + \Gamma_2^+(n)\right) = \sigma(n+1)\cdot \left(\Gamma_1^-(n+1) + \Gamma_2^-(n+1)\right) \tag{2.25}$$

and that (ii) the ensemble distribution $\sigma(n)$ is normalized

$$\sum_{n=-\infty}^{\infty} \sigma(n) = 1. \tag{2.26}$$

The simulation of the tunneling current and corresponding dI/dV spectra using equation 2.24 is shown in Fig. 2.6. The time constants T_i are in the same range for the lower curves. For the upper curves the ratio R_{vac}/R_{oxide} is decreasing and with it the ratio of the time constants T_{vac}/T_{oxide} at constant capacity values, resulting in a Coulomb gap (bottom curve) which changes gradually into a Coulomb staircase (top curve). In the case of metal clusters on ultra-thin MgO/Ag(001) film, an electron transfer of about $0.2e$ per Au atom from the substrate Fermi sea into the metal clusters via tunneling through the oxide layer is guaranteed. This effect is independent of the Coulomb response and controls only the fractional part of the cluster charge value Q_0 which is therefore not zero. The resistivity of the substrate R_2 is mainly given by the thickness of the insulating oxide layer. Since the layer is a few ML, it leads to a highly decreased resistivity R_{oxide} in the tunneling barrier and, hence to an increasing ratio of time constants $T_{vac}/T_{oxide} \to \infty$. Furthermore, R_2 is

adjustable via a variation of the film thickness. From equation 2.24 is seen that in this case the tunneling current I_T is loosing its step-like increase and the Coulomb gap in the dI/dV spectrum is very small (cf. black curve in Fig. 2.6). Hence, the effect of Coulomb charging is negligible in our investigated sample system.

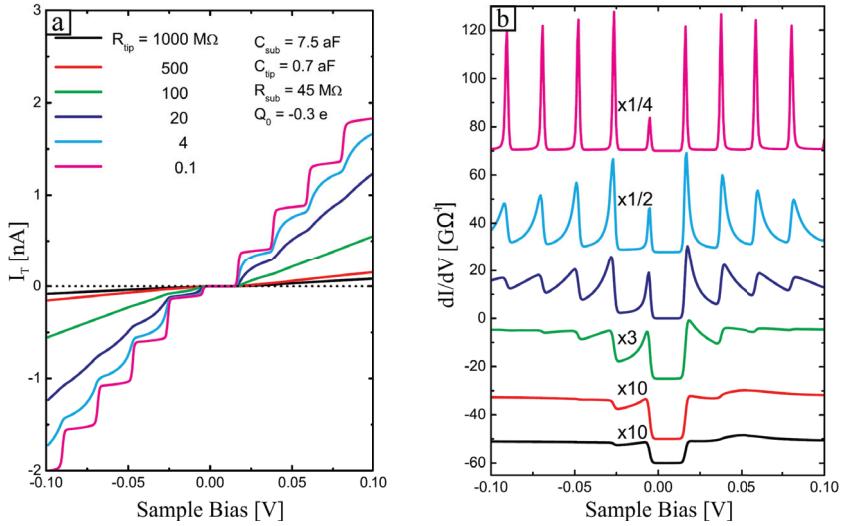

Fig. 2.6: Simulation of the (a) tunneling current and (b) corresponding dI/dV spectra of a Coulomb island using equation 2.24. Only the vacuum resistivity R_{vac} is modified whereas the other parameters in the DBTJ are fixed. From bottom to top is shown the evolution from a Coulomb blockade (gap) to a Coulomb staircase, which can be achieved by approaching the tip (i.e. increasing set point current at fixed bias values) during spectra measurements. Figure adapted from [122].

2.5 Experimental Setup

This chapter contains a brief overview of the custom-built LT-ST) at the Fritz-Haber-Institut (FHI) at which the experiments were performed. For a more detailed description, the reader is referred to the references [93, 123, 124].

2.5.1 Low-Temperature Ultrahigh Vacuum System

The experiments have been performed with a custom-built LT-STM [123–126] which is operated in ultra-high vacuum (UHV). It consists of three parts: (i) a main chamber, (ii) a preparation chamber and (iii) a STM chamber equipped with a pendulum that accommodates the microscope. The preparation chamber is used for sample preparation and sample storage. It is equipped with a

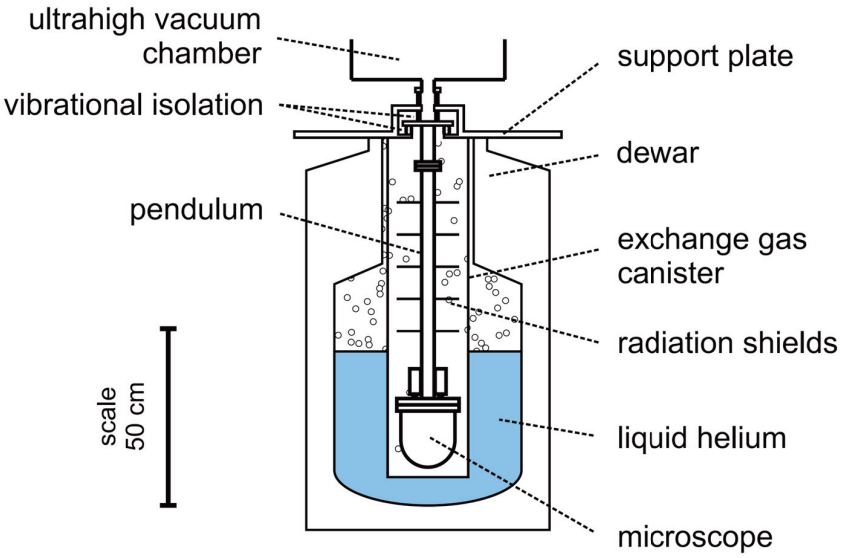

Fig. 2.7: Scheme of the low-temperature UHV chamber housing the custom-built STM. Picture taken from ref. [128].

turbopump, an ion getter pump, an argon (Ar) sputter gun, a sample heater based on electron bombardment, an *Omicron* evaporator EFM3T, a gas supply and a low energy electron diffraction (LEED). The LEED can be used to check the cleanness and crystallographic structure of the sample surface. The main chamber has a separate pumping system consisting of an ion getter pump. The base pressure during STM operation lies in the range of $1 \cdot 10^{-10}$ mbar at RT. A bellow connects the main chamber with the STM chamber which consits of a pendulum accommodating the microscope head. The sample transport between the three chambers is performed with a mechanical transfer system. A scheme of the STM chamber is shown in Fig. 2.7. The microscope is situated inside a liquid helium dewar which contains an exchange gas canister filled with gaseous helium. The helium gas provides first, a good thermal coupling between the microscope and the liquid helium reservoir; and second, it isolates the microscope against vibrations from the outside. This kind of design was firstly realized by Eigler et al. [127]. A main advantage of this setup is its high stability against vibrational perturbations (see below) due to the low eigenfrequency of about 1 Hz of the pendulum. The STM can be cooled down to approximately 5 K. Depending on the desired measuring temperature in the STM, the dewar can be filled either with liquid nitrogen (boiling temperature at standard pressure: 77 K) or liquid helium (boiling temperature at standard pressure: 4 K). In this range the temperature can be adjusted by varying either the helium pressure in the exchange gas chamber

[126] or by warming up the microscope to a well-defined value between 5 and 80 K via the resistive heating of a filament inside the microscope. The latter one provides usually a faster temperature equilibrium than the method mentioned before. The sample temperature is measured via a silicium diode attached to the sample holder. In order to double-check the temperature another diode is mounted outside of the vacuum on top of the microscope flange. In thermal equilibrium, both sensors display nearly the same temperature indicating the good thermal connection in the microscope.

Vibrational isolation is a crucial issue in high-resolution tunneling microscopy. The damping system of the setup consist of several parts inside and outside the UHV system. Each device covers a specific frequency region. The penetration of acoustic waves (10-1000 Hz) is efficiently reduced by (i) a massive acoustic chamber encapsulating the whole instrumentation. To suppress low frequency noise (0.1-10 Hz) mainly transmitted through vibrations of the building, the whole UHV system is mounted onto (ii) a laser table which stands on four pneumatic damping units. Further damping devices are (iii) an additional support plate that is connected to the laser table via four active piezoelectric damping feet. The only further connection to the UHV chamber is (iv) another bellow that is nearly perfectly vibrationally isolated. All stiff connections of the mechanical tip and sample approaches (see below) must be decoupled carefully in order to obtain a good vibrational isolation of the pendulum. A quantitative characterization of the damping performance can be found in [123].

The electronics used for operating the STM are the *Nanonis SPM Control System Base Package* commercially available from the company Specs. It consists of a Realtime Controller (RC4), a Signal Conditioning unit (SC4) and the Nanonis software for the PC. To detect the differential conductance as needed for STS and conductance imaging, an external lock-in amplifier of the type EG&G 7260 was connected to the Nanonis electronics. It can be operated in a range between 0.001 Hz and 250 kHz with a the voltage sensitivity of 2 nV to 1 V.

2.5.2 Microscope Head

The FHI custom-built STM consists of a horizontally aligned tip and a sample opposite of it as it is shown schematically in Fig. 2.8. The approach consists of a coarse and a fine approach between tip and sample. The coarse approach is used to reduce the rather large distance of a few millimeters between tip and sample until both are in tunneling contact. It is realized mechanically

and has the advantage of being reliable in a broad temperature range; on the other hand it is slower than piezo-based approaches. The tip is mounted onto a plate which can be moved linearly in z-direction, i.e. toward the sample. In contrast, the plate carrying the sample performs an eccentric motion which leads to a displacement in z-direction and at the same time, an elliptical motion parallel to the sample surface, hence in x-y plane. Both, the sample plate and the tip plate are moved with ultra-fine threaded axes which are driven by motors from outside the UHV chamber. A detailed description of the coarse approach can be found in [123, 125]. The fine approach is responsible for the tip motion during image acquisition and is performed with a piezo tripod scanner. It consists of three PZT (lead zirconia titanate) tubes which are glued together that they are oriented along the x-, y-, and z-direction. The z-piezo is equipped with a Macor plate containing a cannula for plugging in the STM tip. The tubes have an outer diameter of 6.13 mm, a wall thickness of 0.4 mm and 24.5 mm length (with 10 mm clamped). The application of a voltage leads to an extension of the piezo tubes along their respective axes. A field strength of 2 kV/mm leads hereby to an expansion of 0.15 % of their respective length at RT. At lower temperatures the extension becomes smaller and the maximum area which can be scanned in x, and y direction at 5 K has a size of about (240 nm^2. Depending on the particular experimental situation (e.g. studies of magnetic properties, scanning on metal or oxide surfaces etc.)

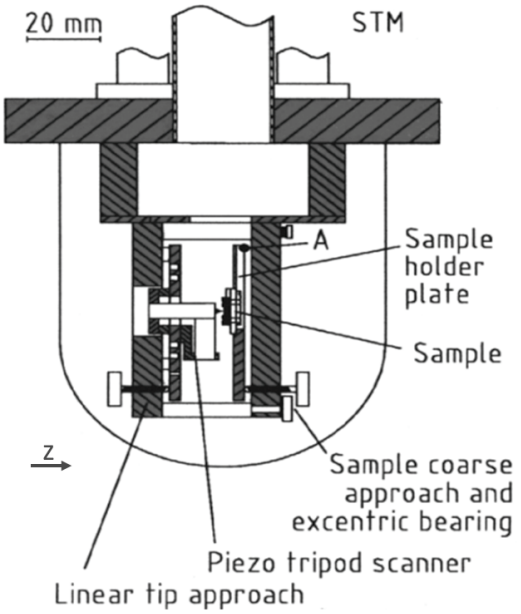

Fig. 2.8: Scheme of the microscope head of the custom-built low-temperature STM.

various materials are suitable for STM tips. Among the most common tip materials is tungsten. Tungsten tips show good mechanical properties [47] and are easy to prepare by etching in an aqueous sodium hydroxide. On the other hand, they get easily covered by an insulating oxide layer and are therefore not suitable for the investigation of oxide surfaces. The tip material of choice in this study was gold. Since it is a noble metal it is very inert toward oxidation. The tip is prepared by etching a commercially purchasable gold wire in an 3:1 solution of hydrochloric acid and ethanol. A good description for the preparation of STM tips and the resulting shapes can be found in [129, 130]. Once the tip is mounted into the STM, it can be prepared *in situ* by (i) poking which means a controlled crash with a gold sample or into gold clusters or by (ii) field emission where a high electric field between 10-30 V/nm is applied between tip and sample (positive sample bias). This leads to evaporation of admaterials from the tip and therefore to a cleaning of the tip. In order to limit the current and protect the electronics, a high resistance of about 10 MΩ is integrated into the electric circuit. Moreover, the I-V converter is disconnected.

2.6 Sample Preparation

The samples in our studies have been silver single crystals with a diameter of about 1 cm and a thickness of about 2 mm. They were cut and polished according to its respective crystallographic plane in the crystal laboratory of the FHI. The single crystals were mounted onto a 15 x 20 x 2 mm^3 sapphire plate as it is shown in Fig. 2.9. The sapphire plate is equipped with two molybdenum bars and two tantal sheets which fix the crystals to the plate. This kind of mounting serves the sample transfer and guarantees a good thermal and electric connection in the microscope. The crystal can be heated via electron bombardment from the backside through a hole of about 8 mm diameter in the sapphire plate. The sample temperature is measured with a thermocouple consisting of a nickel/chromium-nickel wire pair twisted into a small hole in the upper part of the crystal and then separated and contacted trough small holes in the sapphire plate. The Ag(001) single crystals were cleaned by repeated cycles of Argon sputtering and annealing via electron bombardment. In order to avoid thermal tensions in the crystals during the annealing procedure that might lead to structural defects, damage or cracks, the temperature gradient has been kept small with a cooling rate not exceeding 20 K per minute. The mono- and bilayer MgO films were deposited by reactive physical vapor deposition (PVD) of magnesium (Mg) atoms onto the

Ag(001) surface in an oxygen (O) environment of $5 \cdot 10^{-7}$ mbar at 550 K [58]. The film quality was pre-checked with LEED and STM, revealing the sharp (1x1) square pattern of the (001) rocksalt plane in diffraction and extended, atomically flat oxide terraces in microscopy. The ultrathin nature of the film was verified with dI/dV spectra, exhibiting a distinct shoulder at 1.7 V inside the MgO band gap arsising from a Ag-MgO interface state (see chapter 3.1.2).

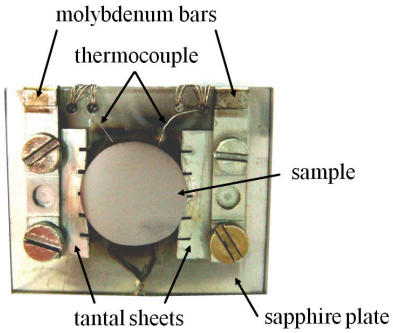

Fig. 2.9: Foto of the sample holder with mounted Ag single crystal. The molybdenum bars and tantal sheets serve for accurate fixing of the crystal.

Deposition of Gold Atoms and Clusters

The preparation of Au clusters on the MgO film has been done in two different ways. Firstly, in the preparation chamber at RT by evaporating gold from a tungsten crucible onto the oxide surface. Secondly, single Au atoms could be deposited inside in the STM by heating of a gold-covered filament. When heating the sample up to about 80 K, Au clusters were formed due to the temperature induced thermal mobility on the sample surface. Different cluster sizes and shapes were achieved via a variation of the sample temperature during the deposition procedure and the amount of deposited metal. The metal clusters were characterized by topographic and spectroscopic methods in the STM.

Deposition of Molecules

Molecules were adsorbed onto the MgO surface and Au clusters in the main chamber. Isophorone (0.5 L) was dosed at RT from a flask containing the liquid compound, while CO_2 (5 L) was supplied by backfilling the chamber with $1 \cdot 10^{-7}$ mbar for 50 s at 250 K sample temperature. Subsequently, the samples were quickly transfered to the liquid helium reservoir in the STM to avoid contamination from the rest gas. A typical transfer took 7 to 8 minutes, while cooling down to liquid helium required about 30 to 45 minutes.

Chapter 3

Sample Systems

3.1 MgO Thin Films

3.1.1 General Aspects and Properties

MgO is a prototype material for wide band-gap insulators [131, 132]. It has a simple atomic configuration, consisting of two atoms in the unit cell of cubic rock salt structure (cf. Fig. 3.1). The bulk band gap is 7.9±0.7 eV at 0 K [133]. This properties make MgO to a ideal system to be studied both experimentally and theoretically, and further, it represents a good starting point to approach more complex materials. Additionally, MgO is gaining more and more attention in fields like heterogeneous catalysis as bare oxide [134–136] and as support for metal particles [137–141], in photocatalysis [142] and as magnetic tunnel junction in spintronics [143, 144]. Analyzing the surface of thin films grown on metal substrates has the advantage of avoiding electrical charging due to the metallic support, an effect hat would be encountered during experiments on MgO single crystals [37]. The film thickness has been recognized as an important parameter to tune properties of the thin films and adsorbates [4, 146, 147]. In an ideal preparation technique, the surface structure of the thin films is identical to those of single crystals due to epitaxial growth. However, the preparation of such thin layers is a complicated task and many parameters have to be controlled [148]. The main issue is the selection of a suitable metal substrate on which the thin film is grown. This should have (i) a similar lattice constant as the MgO (i.e. a small lattice mismatch) in order to minimize epitaxial strain, (ii) a low affinity to oxygen, and (iii) a rather high melting temperature to allow annealing to improve the film quality. The simple rock salt structure allows the growth of epitaxial films on a variety of substrates as long as the lattice mismatch with the MgO

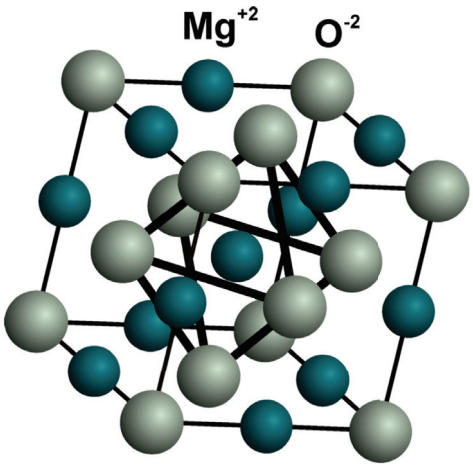

Fig. 3.1: Crystallographic structure of bulk MgO. The O ions form a fcc structure with Mg ions in half a lattice constant distant. The center of the fcc unit cell inherits an octahedral fcc network of oxygen ions neighbored by Mg ions forming a rock salt structure. Figure taken from ref. [145].

does not exceed 5-7 %. So far MgO films have been deposited on Ag(001) [58, 110, 149, 150], Fe(001) [143, 144] and Mo(001) [91, 151–153] substrates. For the three substrates the lattice mismatch with MgO is 2.9 % [154], 3.5 % [143] and 5.3 % [145], respectively. Therefore, the Ag(001) support seems to be most suitable. However, this is only the case in the ultrathin film limit, i.e. 1 to 8 ML [18], since the low melting temperature of silver prevents from annealing thicker films and thus from a thermally-driven improvement of the film structure. Concerning the annealing point, Mo(001) substrate suits better because of its higher melting temperature of about 2900 K [155]. Theoretical and experimental studies showed that MgO thin films exhibit the same chemical features as MgO single crystals [156] but differ in certain properties as for instance the CO binding energy on the surface due to the high concentration of defects in the films [157], or the shape of deposited Au nanoparticles [18, 158, 159] due to electron transfer from the substrate.

3.1.2 MgO Thin Films on Ag(001)

The epitaxial growth of MgO thin films on metal single crystals depends strongly on the lattice mismatch between oxide and chosen support. A small lattice mismatch reduces substrate induced strain effects and therefore, improves the film quality. As mentioned above, MgO is preferably grown on the Ag(001) surface due to the comparably small lattice mismatch of 2.9 % between the Ag and MgO (nearest neighbor (NN) distance for Ag(001):

d_{Ag-Ag}=2.89 Å, and MgO: d_{Mg-Mg}=2.98 Å). The MgO film grows in the Frank-van-der-Merve mode on top of the fcc (face center cubic) Ag(001) substrate [1, 160]. The O anions are located on the Ag top sites and Mg cations prefer fourfold hollow sites with respect to the Ag layer as derived from DFT calculations [160]. This is in agreement with calculations of Smoluchowski from the year 1941 [161] where he had shown that the electron gas of a clean metal tends to move into the holes between the surface atoms which are, therefore, the preferred binding sites for cations. The mean interfacial distances between the MgO overlayer and the surface as calculated by DFT are for Mg and O 2.55 Å and 2.46 Å, respectively [162]. Experimentally determined interface distances of 2.53 ± 0.05 Å and 2.39 ± 0.06 Å have been found by extended x-ray absorption fine structure (EXAFS) [163] and LEED [164] measurements, respectively.

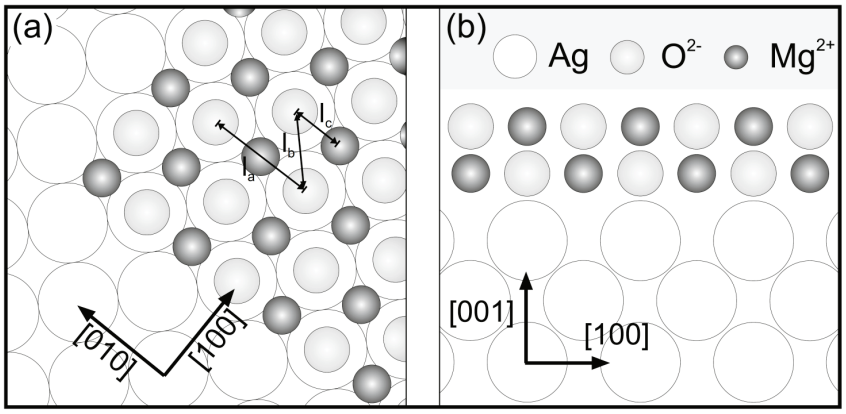

Fig. 3.2: Model of the rock salt MgO lattice grown on fcc Ag(001) in (a) top and (b) side view. O atoms sit on top of Ag; Mg atoms on the hollow sides between the Ag. In (a) is pointed out the Ag unit cell length l_a=4.08Å, the NN distance of Ag l_b=2.89Å and the Mg-O bonding length l_c=2.04Å. Figure taken from ref. [165].

Another issue in MgO thin films is rumpling[1] [166]. For a monolayer MgO film the surface corrugation due to rumpling is about 0.1 Å and results from a release of compression energy which has been formed due the MgO-Ag lattice mismatch. Already for the second ML of MgO, the interface rumpling decreases by a factor of three to a value of only 0.03 Å between anion and cation positions [162]. The average distance between the first and the second layer of the supported MgO bilayer film is elongated in comparison with that of bulk MgO by 3 % [162]. An elongation of 3.6 % is reported experimentally

[1]Rumpling describes the different relaxation (change in inter-plane spacings) of anions and cations in z-direction.

for 3 ML MgO films and a complete recovering of the bulk value occurs in 6 ML films [149, 167]. The topmost Ag layers are also affected by the MgO overlayer. Their positions change by -0.027 Å and -0.055 Å [162] for a mono- and bilayer MgO film, respectively, as compared to the clean and relaxed Ag surface.

Especially interesting is the bonding and the related change in the electronic structure of the noble metal - inert oxide interface. The bonding mechanism as well as the electronic structure of the MgO/AgO(001) interface have been studied by various surface science techniques as high resolution electron energy loss spectroscopy (HREELS), LEED and TPD [151]; Auger electron spectroscopy (AES), UPS and XPS [168]; and STM/STS [58, 59, 169]. Associated to the experiments, theoretical calculations contributed immensely to the understanding of decisive parameters determining the interface [58, 160, 162, 164, 168, 170]. From the UPS spectrum of a 10 ML MgO film (Fig. 3.3a) is seen that the valence band maximum is fixed at about 4 eV below the Fermi level[2] [171]. An EELS spectrum of the same film (Fig. 3.3b) shows the energy losses corresponding to the interband transitions in the inner part of the MgO and at the surface of 7.8eV (B) and 6.2eV (S), respectively [151, 172, 173]. From both spectra one can deduce the energy level scheme shown in Fig. 3.3c. Fig. 3.3d shows a STS spectrum of a monolayer MgO/Ag(001) film [58]. In the negative bias regime (tunneling from occupied electronic states in the sample) the LDOS increases at around -4 V, whereas at positive sample bias (tunneling into unoccupied electronic states in the sample), two structures are detected at 1.7 V and 2.5 V. Between -4 V and 1.7 V, the dI/dV signal is constant which indicates an unchanged finite tunneling current. The peak at 2.5 eV is independent of the film thickness and, hence associated to the MgO empty conduction band [172, 174, 175]. The intensity of the LDOS peak at around 1.7 V observed in STS in monolayer MgO films diminishes for bilayer films and is not detectable anymore for film thicknesses of 3 ML and more (not shown here). This feature is attributed to a MgO-Ag interface states [168]. Combining STS with conventional electron spectroscopy leads to the conclusion that at 3 ML MgO coverage the electronic structure at the MgO surface shows no contribution from interface states, but corresponds to the electronic structure of an MgO(001) single crystal surface. The experimental findings on the MgO-Ag interface state have been subsequently confirmed by DFT calculations [58]. Furthermore, the Schneider group [58, 59]

[2]In photoemission as well as STS the Fermi level is fixed by the metallic substrate. Tip-induced band bending is comparably small as long as the LDOS of the metal substrate is "leaking"through the MgO film.

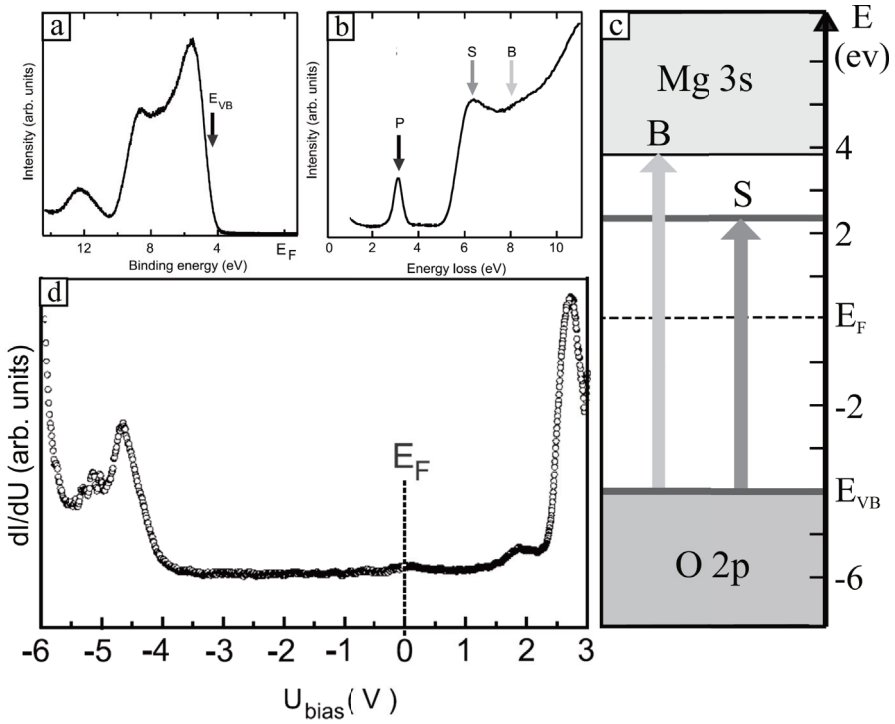

Fig. 3.3: Electronic structure of a 10 ML stoichiometric MgO/Ag(001) film as determined by (a) UPS and (b) EELS. In (a) the valence band onset is indicated. The (b) EELS spectrum indicates the Ag–MgO interface plasmon excitation (P) [118, 134], the inter-band transition at the MgO(001) surface (S) and bulk (B). (c) The resulting MgO(001) energy level scheme is derived and can be compared with the (d) STS spectrum of a 1 ML MgO/Ag(001) film. Figure adapted from [59].

has investigated the field emission resonances (FER) of monolayer MgO films and Ag substrates. They report a shift of 0.4 eV toward lower energies for the MgO FER compared to the Ag ones, consistent with a reduced oxide work function as observed in UPS for the monolayer MgO film. For more details the reader is referred to [58, 59].

The lowest ionization states of MgO have mainly O 2*p* character. Hence, the interaction with the Ag support is expected to result mainly from O 2*p* states coupled to Ag 4*d* and Ag 5*sp* orbitals. However, XPS measurements have shown that the O 2*p* states hybridize strongly with the Ag 5sp but show only a weak interaction with the Ag 4*d* states [168]. With respect to unsupported MgO, the hybridization of the O 2*p* with the Ag 5sp states is responsible for a shift of the oxygen DOS toward the Fermi level [160, 162]. These states are often called metal induced gap states (MIGS) and are a general feature of metal-oxide interfaces [176–178]. MIGS are mainly localized

at the metal-oxide interface which is corroborated by calculations showing that a second oxide layer does not contribute significantly to the MIGS [58]. As the MIGS lie in the band gap, they have a characteristic damping length [179] which reaches its maximum in the middle of the gap. Assuming an exponential decay of the charge density in z-direction [160]

$$\rho(z) = \alpha \cdot \exp -2z/\lambda \tag{3.1}$$

with λ being the decay length of the initial charge density α. The decay length has been determined as $\lambda = 1.19d$, which for a mean interplanar distance of d=2.5 Å between Mg and O atoms leads to a decay length of λ=2.98 Å. Hence, the MIGS are mainly present in the first ML of MgO; weakly interact with the second ML; and vanish for further increasing film thickness. This result is in excellent agreement with the measurements of the Schneider group [58] showing the existence of the MgO/Ag(001) interface state in the first two ML only.[3]

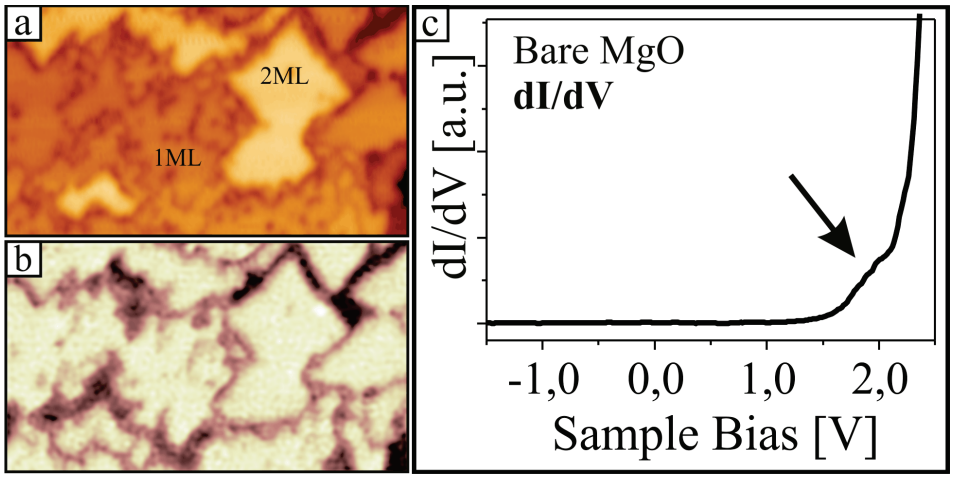

Fig. 3.4: (a) Topographic image and (b) corresponding dI/dV map of a MgO/Ag(001) film with 1 to 2 ML thickness at 1.7V (70 x 40 nm^2, 30 pA). (c) STS spectrum for a 1 ML MgO film with the MgO-Ag(001) interface state (IS) located at 1.7 V, indicated by the black arrow. With the help of the IS, it is possible to distinguish between regions of mono- and bilayer films (bright contrast) from regions with thicker films and bare metal substrate (dark contrast) in the dI/dV map in (b).

[3]Note that the MgO/Ag(001) interface state at 1.7 eV might have its origin in a MIGS. Another possible interpretation may be a split-off state, which is separated from the unoccupied Mg-induced conduction band [59, 180].

3.1.3 Comparison with MgO Films on Mo(001) and Fe(001)

MgO on Mo(001) supports is prepared in a similar way as MgO on a Ag(001) support: via a reactive deposition of evaporated Mg in an oxygen environment of about $1 \cdot 10^{-7}$ mbar at RT. The main difference is that due to the much higher melting point of Mo compared to Ag, the as-grown oxide film can be post-annealed up to about 1100 K [145]. This leads to an improved film crystallinity and a lower defect density. The advantage of the high-temperature annealing step is partly compensated by the enhanced lattice mismatch of 5.3 % between the MgO and Mo(001), as compared to Ag(001). The lager lattice mismatch induces a complex relaxation behavior as a function of the MgO thickness, which induces various morphological stages [91, 145]. In the submonolayer regime close to 1 ML, the MgO film consists of larger holes that are confined by polar [110] and non-polar [100] oriented edges (cf. Fig. 3.5a).

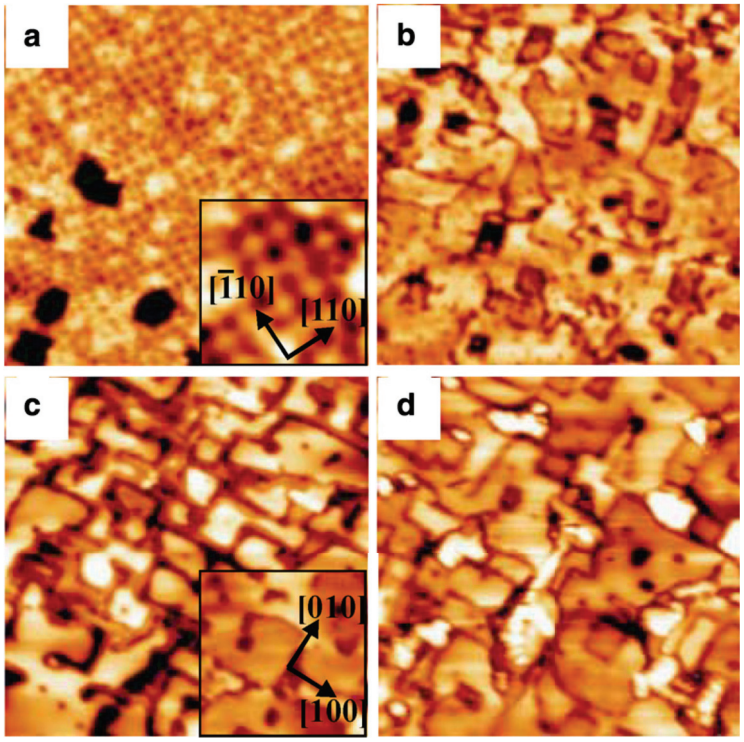

Fig. 3.5: Topographic images of MgO/Mo(001) films: (a) 150 x 150 nm^2, 0.85 ML MgO, the inset shows a 25 x 25 nm^2 zoom of the observed square pattern of the same sample. (b) 100 x 100 nm^2, 1.75 ML MgO; (c) 100 x 100 nm^2, 7 ML MgO, the inset shows screw dislocations which typically occur for film thicknesses of 5-10 ML MgO; (d) 100 x 100 nm^2, 18 ML MgO. Picture taken from ref. [91].

These holes were observed also for MgO/Ag(001) thin films. They reflect the first stage of overcoming the metal-oxide misfit strain [181, 182]. Furthermore, a regular square pattern appears with a mean size of 55 Å which was identified as a coincident lattice arising from the mismatch between MgO and Mo(001) (18 MgO unit cells on 17 Mo cells along MgO[110]). In addition to the lateral displacement, a tilting of the grown overlayer by 1-5° is observed to compensate the misfit strain.[4] The surface Moiré pattern, resulting from a superposition of the squared MgO and Mo(001) lattices with slightly different atomic distances, vanishes between 8-10 ML film thickness. The dominant structural features are now dislocations lines, step edges and rectangular holes of about 30Å diameter (cf. fig. 3.5b). At 7 ML film thickness, the oxide film closes indicating a good layer-by-layer growth accompanied by a gradual flattening of the surface roughness (cf. fig. 3.5c) and the appearance of screw dislocations (cf. Fig. 3.5c, inset). Above 18 ML thickness, STM experiments become difficult due to the vanishing conductivity between tip and sample, as a result of the insulating character of oxides (cf. fig. 3.5d).

MgO films grown on Fe(001) are especially interesting because they can be used as magnetic tunnel junctions, where the insulating oxide separates the magnetic substrate from a magnetic ad-film or ad-particle. A structural model has been derived from X-ray measurements [143]. Here, MgO/Fe(001) has been epitaxially grown by electron beam deposition of Mg from a polycrystalline rod in UHV. A layer-by-layer growth was observed up to 5 ML oxide thickness. The layer-by-layer growth is however not perfect because the third (second) layer starts to grow before the second (first) one is completed. X-ray investigations gave direct evidence that a FeO interface layer between the Fe electrode and the MgO barrier is formed before the MgO growth starts. The vertical distance of the first MgO layers is slightly enhanced compared to bulk MgO due to the compensation of the 3.5 % lattice mismatch between the grown oxide and substrate, which in turn laterally compresses the film. By RT-STM experiments, the electronic properties and defect landscape have been investigated [144]. Mather et al. [144] have prepared MgO films on 4 nm thick Fe(001) which was perfectly grown on gallium arsenide substrates. Better films have been synthesized via a two-step sputtering procedure where, firstly, Mg atoms are sputtered onto the Fe surface in an argon Ar environment, followed by a reactive oxygen sputtering to oxidize the Mg layer. The post-annealing process turned out to be important for significantly increasing the band gap (compared to the non-annealed film) that varied with film

[4] A detailed analysis of the complex relaxation structure on MgO/Mo(001) can be found in ref. [145].

thickness from 0.5 V for 2 ML up to 1.5 eV for 8 ML film thickness. For films of comparable thickness, a band gap of 7.5 eV was observed for MgO/Ag(001) reported by the Schneider group [58]. From XPS measurements a shift toward lower binding energies indicate the presence of negatively charged Mg vacancies besides the oxygen defects. The vacancies were ascribed to the strain arising from the lattice mismatch between the MgO and the Fe. The defect density reduces with increasing film thickness as a progressive stress relaxation takes place away from the interface.

In summary, due to the possible post-annealing step in the preparation procedure of the MgO/Mo(001) films, they have a better film crystallinity up to many ML thickness and already the first ML is closed. Therefore this film is better suited for the investigation with averaging methods where global film properties are in the focus of study as for instance XPS and UPS for structural and electronic properties, and IRAS, EELS and TPD for adsorption experiments on the MgO surface. In contrast, such investigations are hardly possible for MgO/Ag(001) films. Due to the missing post-annealing step in the preparation, a closure of the film with a high crystallinity over several micrometers is not possible. In comparison, MgO/Ag(001) films have a smaller lattice mismatch which makes them flat already in the ultra-thin and submonolayer regime, with only small vertical displacement in z-direction. This advantage is absent for the MgO growth on Mo(001) due to the enhanced strain in the first few ML, resulting in a patch-like structure and a strong tilt of the film in z-direction. Therefore, the Ag(001) is the support of choice for investigations of ultra-thin MgO films via local scanning probe methods such as STM-STS or AFM [169, 183, 184]. Furthermore, ultrathin films can be scanned at very low bias voltages, enabling STM-STS investigation of the electronic structure around the Fermi energy. This allows to explore surface states, QWS, or determining the size of the energy gap between the highest occupied molecular orbital (HOMO) and lowest unoccupied molecular orbital (LUMO) in metal deposits (see next chapter). Since flat MgO films on Mo(001) are only observed for thicknesses above 6 ML, the scanning bias in STM experiments needs to be higher than 2.5 V as a result of the insulating oxide properties. MgO/Fe(001) films are preferentially used for the investigation of magnetic tunneling barriers when depositing magnetic ad-particles. Here, the MgO plays the role of a non-magnetic spacer between the magnetic Fe substrate and magnetic adsorbates. This property makes Fe unique with respect to Ag and Mo. A good film crystallinity and sufficient similarity to the bulk MgO band gaps are already achieved for thicknesses of 8 ML.

3.2 Metal Particles on Surfaces

3.2.1 General Aspects

Metal particles on surfaces consisting of only a few hundred atoms are confined quantum systems. When reducing the atom number from 10^{23} per cm^3 in a bulk metal to several hundred atoms, the transition from a bulk system into a molecule-like system takes place accompanied by a break down of the periodic band structure into a set of quantized states (cf. Fig. 3.6). This metal to non-metal transition is characterized by a change of the size of the HOMO-LUMO gap as the intrinsic parameter describing the performance in chemical/catalytic reactions. In general, the HOMO-LUMO gap is decreasing with increasing atom number [10] and irregular shape of the cluster [61], and the molecule-like behavior of the nanostructures vanishes. These features make metal particles deposited on surfaces one of the most interesting and manifold systems in science.

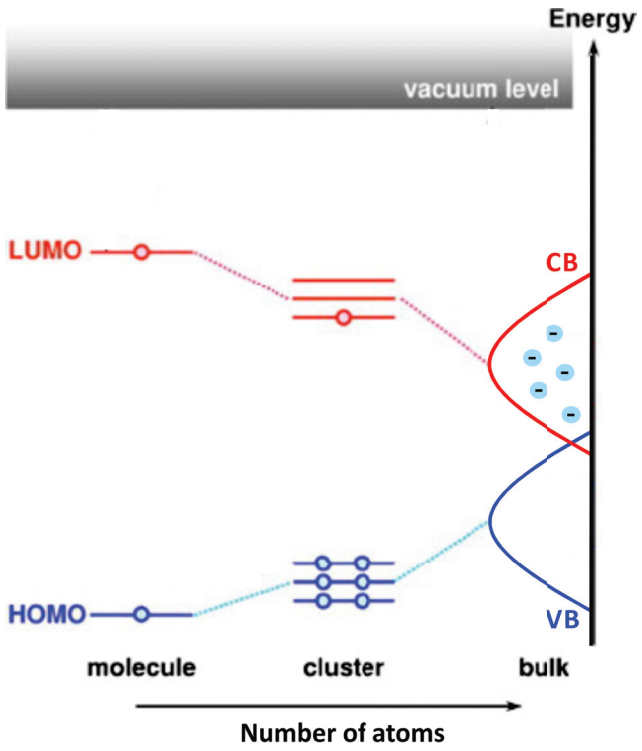

Fig. 3.6: Band gap scheme of a metal depending on the atom number. The electronic structure develops from localized states for molecules and metal clusters into a periodic band structure for the bulk material characterized by its conduction (CB) and valence band (VB).

An assembly of many low-coordinated atoms is called cluster. From a physical point of view these nanostructures do not represent a cutout of the respective bulk crystal but show completely new chemical, electronic and optical properties which depend strongly on the number and arrangement of the individual atoms. Small clusters consist of many surface atoms and, therefore, have a high surface-to-volume ratio. For example in a Au cluster of the magic size of 13 atoms, 92 % of all atoms are located on the surface while for a cluster consisting of 1415 atoms, only 35 % of all atoms are surface atoms (assuming an icosahedron cluster geometry). The general shape of oxide-supported metal clusters can be derived from an evaluation of the free energy balance [1]. It is mainly a competition between the surface free energies of the oxide support γ_{ox}, the dominant particle facet γ_{me} and the interface energy γ_{me-ox} between the two (cf. Fig. 3.7b). If the free surface energy of the oxide support is larger than the sum of the free surface energy of the metal and the metal-oxide-interface $\gamma_{ox} > \gamma_{me} + \gamma_{me-ox}$ then the metal wets the oxide surface and forms large 2D islands (Frank-van-der-Merwe growth) via a layer-by-layer growth. In contrast, if the oxide free surface energy is smaller than the sum of the free surface energy of the metal and the metal-oxide-interface $\gamma_{ox} < \gamma_{me} + \gamma_{me-ox}$, a wetting is thermodynamical prohibited and the metal deposit grows 3D (Vollmer-Weber growth) as it is observed for most metal deposits on oxide surfaces (cf. Fig. 3.7). In general, the surface free energies of metals (and especially of transition metals) are larger than for oxides [36]. This means that a layer-by-layer growth is an exception for metal particles on oxide surfaces and that the growth of 3D particles is very likely which is confirmed by several former studies [35, 36, 38, 186–188]. In the case of the Vollmer-Weber growth, a so-called Wulff polyhedron is formed [189] (Fig.

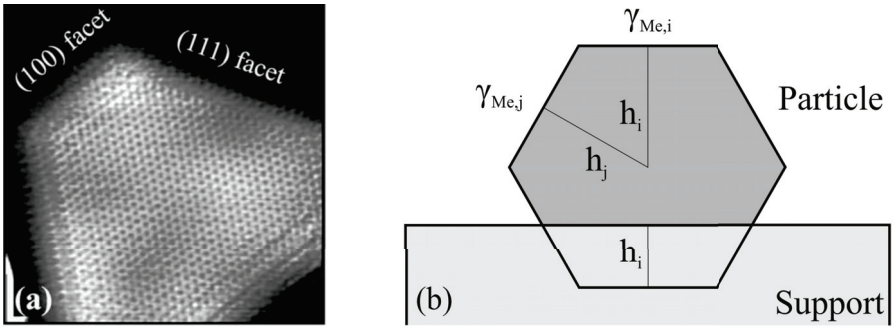

Fig. 3.7: (a) Atomically resolved STM image of a 3D Pd cluster (10 x 10 nm^2) with two different facets (picture taken from ref. [185]). (b) shows a scheme for the construction of a Wulff polyhedron.

3.7b). It becomes more and more flat with increasing metal-oxide interaction, i.e. with increasing adhesion energy. Thereby, the particle truncation Δh at the interface is given with respect to the height h_i of the particular facet above the particle center by the relation [1, 38]

$$\frac{\Delta h}{h_i} = \frac{E_{adh}}{\gamma_{me,i}} \tag{3.2}$$

with E_{adh} being the adhesion energy and $\gamma_{me,i}$ the free energy of the metal facet i. Assuming the system to be stabilized in thermodynamic equilibrium, the complete cluster geometry can be found by a Wulff construction [38]. In a third growth mode, the first layer of the metal wets the oxide surface completely due to a strong interface adhesion whereas additional material grows 3D (Stranski-Krastanov growth). This 2D to 3D growth transition is governed by a large lattice mismatch between the wetting metal layer and the bulk-like surface material, avoiding further layer-by-layer growth. With the exception of some thin oxide films such as the growth of Au clusters on MgO/Ag(001), the Stranski-Krastanov regime is mainly observed for the opposite case, i.e. the growth of oxides on metal surfaces [190, 191].

3.2.2 Quantization of Electronic Structure

In the limit of single atoms and small aggregates up a few hundred atoms, quantum mechanics plays the dominant role and the electronic properties are governed by discrete states [16, 192]. If small metal particles are deposited onto oxide surfaces, as it has been experimentally realized for Au on Alumina [11], MgO/Ag(001) [10, 61, 193] or on Si(557) [194], QWS are formed. The geometrical arrangement of the cluster atoms plays a major role in this scenario because it determines the symmetry of the confining potential on the surface. In general, the cluster growth happens in a 3D fashion, referring to the Wulff polyhedron shown in Fig. 3.7. In these systems, the electronic states quantize in all three dimensions, making the understanding rather complicated. However, if depositing only a small amount of metal atoms on oxide surfaces or if a sufficiently high transfer of extra charges is guaranteed from the underlying support into the cluster, the cluster growth may occur in a 2D fashion. This behavior has been observed for Au clusters on MgO/Ag(001). The MgO film in the ultrathin limit permits an electron transfer via tunneling from the Ag support through the oxide film into the Au deposits. This electron exchange is a cooperative effect between the low MgO/Ag workfunction and the high electronegativity of gold [195]. For single Au atoms this leads to an extra

charge resulting in Au^- anions [43], and resulting in clusters with various shapes but only of monolayer height [18, 19]. The Au anions in the cluster experience thereby an enhanced bonding to the oxide film, which is mediated by Coulomb and polaronic interactions with the MgO surface and renders a 2D growth energetically preferred [158]. Due to the Coulomb repulsion, the extra charges localize at the cluster perimeter leading to the development of additional edge states [193]. The same effect has been observed for Au clusters deposited on self-doped CaO films on a Mo(001) substrate [21, 22]. In this case, extra charges are provided by electron rich Mo dopants in the oxide film that can travel to the surface and make the clusters grow in a 2D pancake shape of monolayer height. In the case of clusters with monolayer height only lateral quantization of electronic states is observed, simplifying the problem significantly. The symmetries of metal deposits on surfaces range from linear chains on metals [196–198] and oxide supports [11, 19], over spherical clusters [10], up to triangular [61, 199, 200] and hexagonal structures on metals [66, 201] and oxide surfaces [202] or to characterize clusters with total arbitrary shape [61].

In order to obtain the dispersion relation of electronic states for metal clusters on oxide surfaces, one has to solve the stationary Schrödinger equation (SGL, from German "Schrödinger Gleichung") (cf. equation 2.1). Depending on the particular cluster shape, an adequate analytical expression for the cluster potential that confines the electron system is difficult to obtain. In general, the SGL can only be solved numerically. However, there are a few examples where the SGL has an analytic solution which makes the interpretation and understanding of the observed phenomena quite convenient. The simplest model to characterize such electronic systems is a rectangular "particle-in-a-box" (PIB) model. Referring to the examples shown in Fig. 3.8, one can estimate the potential for (a) a linear chain by a 1D box potential; (c) a triangular cluster by an isosceles, right-angled triangular box potential (as a special case of a rectangular 2D box potential); and (d) a hexagonal cluster by a hexagonal box potential. For sake of simplicity, in a first approximation the box potential can be assumed to be infinitely deep. For the case shown in Fig. 3.8b, it has been shown that the shape of the nanostructure's electronic orbitals could be well described by a particle in a harmonic potential [10]. For the dispersion relation, one can say in general: as long as the problem can be separated into independent 1D cases, the $E(k)$ (or $E(n)$) relation shows a

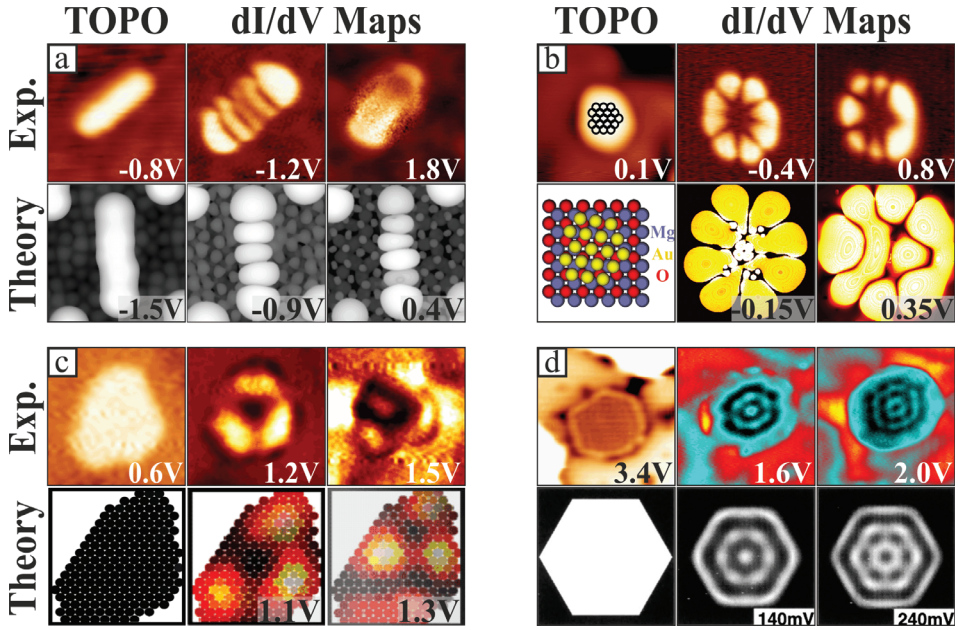

Fig. 3.8: Measured topographic and dI/dV maps (top row) with corresponding theoretical calculations (bottom row) of (a) a linear Au_7 chain on Alumina [11], (b) a spherical Au_{18} cluster [10], (c) a triangular Au_{170} and (d) a hexagonal Au_{300} cluster on MgO/Ag(001) thin films. In (a) and (b), the dI/dV maps correspond to the HOMOs and LUMOs; in (c) to the 3rd and 4th states of a particle in an isosceles, right-angled, triangular box potential; in (d) to the 10th and 16th state for a particle in a (ideal) hexagonal box potential. Calculations in (d) are taken from ref. [66].

quadratic dependence and can be expressed by [203]

$$E_n = E_0 + \frac{(\pi\hbar)^2}{2m_{eff}} \sum_i \left(\frac{n_i}{L_i}\right)^2 \tag{3.3}$$

with $i = x, y$, the quantum number n, L_i being the length in the respective direction, m_{eff} the effective mass of the electron system, E_0 the onset energy. In the other cases, i.e. when a separation into 1D problems is not possible, the dispersion relation shows a linear dependence with respect to k (or n). This is the case for spherical clusters described by a particle confined in a harmonic potential, in circular [64, 204, 205] or hexagonal box potentials[5] [66, 201]. A next step towards real cluster potentials is to reduce the height of the potential box from infinite to a finite value V_0. In this case, the wave functions spill out

[5]The dispersion relation for a particle in an ideal hexagonal box is technically speaking non-analytic but one can obtain a quasi-analytic dispersion relation in first approximation as it is shown in ref. [202].

into the barrier region where they decay exponentially. This is accompanied by a reduction of the eigenenergies of the individual wave functions.

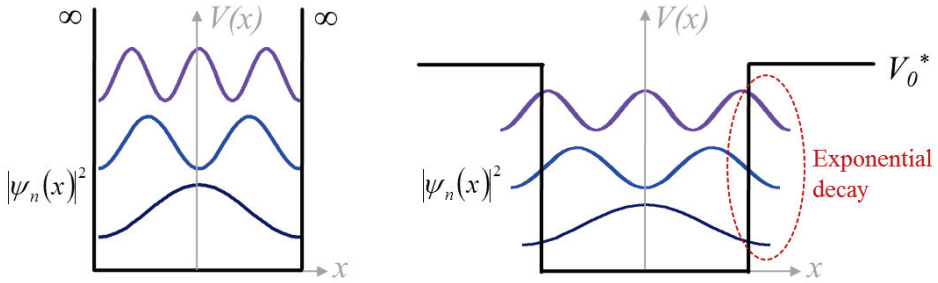

Fig. 3.9: Cartoon for the quantization of electronic states of a particle in a 1D rectangular potential well of infinite (left) and finite (right) depth.

The precise characterization of the QWS in Au clusters on MgO/Ag(001) thin films turns out to be a key feature in the investigation of the electronic interaction between this model catalytic system and adsorbed molecules. One hypothesis is that in the adsorption process charge transfer occurs between the two chemical species. In a first Gedankenexperiment, one can imagine to use the Au nanoparticle shown in Fig. 3.8b to quantify the exact charge transfer by counting the individual electrons in the cluster. As it has been shown by X. Lin et al. [10], the electronic system of the Au_{18} cluster contains 22 electrons (18 coming from the Au $6s^1$ orbitals of the individual cluster atoms and four extra electrons from the support). The corresponding level scheme for a particle in a harmonic potential is shown in Fig. 3.10a, depicting the *1G*-like HOMO (left picture) and *1G**-like LUMO (right picture). If a molecule that either has the tendency to donate or accept electrons adsorbs on the cluster, its electronic structure can be changed intentionally due to the difference in electronegativity between the gold and the ad-species. Adsorbing an electron donor (e.g. hydrogen, sodium, lithium) to the cluster, a charge transfer from the adsorbate toward the cluster occurs accompanied by a change of the cluster valence states (cf. Fig. 3.10 b). The former LUMO would become the new HOMO (unchanged 1*G*-like shape; indicated by the red arrow) while the former LUMO+1 would become the new LUMO (new 2*D*-like orbital shape). In the opposite case, i.e. upon adsorption of an electron acceptor (as oxygen, chlorine, fluorine, CO_2) to the cluster (cf. Fig. 3.10 c), the former HOMO would become the new LUMO (unchanged 1G-like orbital; indicated by blue) and the former HOMO-1 the new HOMO (2*P*-like shape). First related experiments have been performed with CO at Au clusters on NiAl(110) [108]

and MgO/Ag(001) [206]. In addition, Repp et al. [60] have shown that the adsorption of an individual gold atom on a pentacene molecule leads to a change of the HOMO and LUMO.

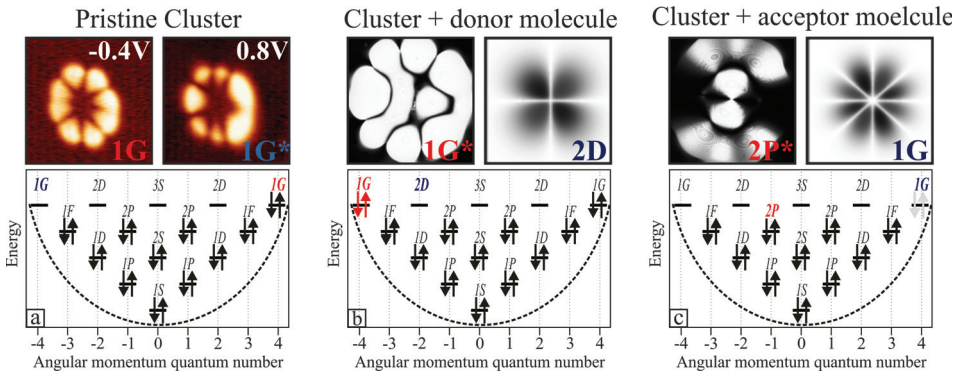

Fig. 3.10: (a) Level scheme of the spherical Au_{18} cluster on ultra thin MgO/Ag(001) shown in fig. 3.8b [10]. Upon adsorption of an (b) electron donor or (c) acceptor, the HOMOs (indicated by red) and LUMOs (indicated by blue) change accordingly. (Remark: Transfer of two electrons is assumed between molecule and cluster.)

Chapter 4

Electron Quantization in Arbitrarily Shaped Gold Clusters

The following chapter presents the effect of the cluster size and shape on the electronic structure of ultrasmall Au particles. Therefore, three model clusters with an approximately rectangular, triangular and quasilinear symmetry are chosen. The electronic structure, rationalized by a PIB model, is compared with electronic density calculations performed via a density-functional-tight-binding (DFTB) code.[1] The final part of this chapter elucidates two general features for quantization effects in Au nanostructures. These are (i) the general dependence of the HOMO-LUMO gap on the cluster size and shape and (ii) the estimation of the real cluster potential using a PIB model with finite potential well depth instead of an infinite one. The HOMO-LUMO gap is an intrinsic parameter for the performance in chemical reactions.

4.1 Characterization of the Sample Surface

Fig. 4.1a shows a topographic overview of the sample surface. According to chapter 3.1.2, the ultrathin nature of the MgO was verified with dI/dV mapping at 1.7 V (Fig. 4.1b) revealing characteristic bright contrast regions on the surface arising from the Ag-MgO interface state located inside the

[1]DFTB calculations are calculations based on density functional theory but including electronic densities from a superposition of atomic orbitals, as they are obtained by the linear combination of atomic orbitals or tight-binding approach. For more information, the reader is refereed to ref. [207, 208].

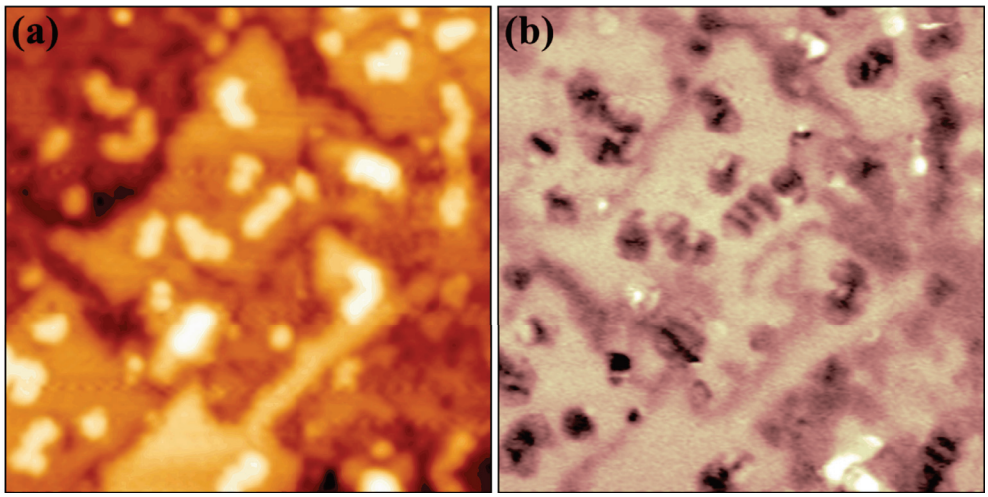

Fig. 4.1: (a) Topographic image and (b) corresponding dI/dV map of a 2 ML MgO/Ag(001) film covered with Au islands (50 x 50 nm^2, 1.7 V, 100 pA).

oxide band gap. Darker regions are ascribed to uncovered silver and thick oxide patches. Gold with 0.05 ML nominal thickness was deposited onto the oxide film at LT and ad-atom diffusion and formation of metal aggregates was provided by annealing the sample to 80 K directly inside the cryogenic STM. The resulting metal islands of monolayer height appearing as protrusions on the surface (Fig. 4.1a) typically comprised 50-200 atoms, and were found to nucleate both on pristine MgO terraces and step edges. In addition, the quantization patterns of the metal nanostructures become nicely discernible in the conductance maps shown in Fig. 4.1b.

4.2 Rectangular Gold Clusters

The first example is an Au cluster with an approximately rectangular shape and a size of 7.5 x 3 nm^2. By filling the surface area with a hexagonal close-packed arrangement of Au atoms with a NN distance of 2.89 Å, which is similar to the lattice parameter in the Au(111) surface, a structure model of the island could be obtained (cf. Fig. 4.2a, inset). Thereby, a 5 Å wide rim has been kept open at the island perimeter to account for the tip convolution effects of the STM. The total number of atoms is estimated to be 130. Uncertainties in this procedure limit the accuracy of our model structure to about 20% (roughly one atom row along the island perimeter). The valence electronic structure in the cluster is governed by the formation of QWS. Their exact energy position and spatial localization were measured by STS and dI/dV mapping, respec-

tively. In Fig. 4.2a are shown dI/dV spectra of the Au island. Both spectra can be divided into two parts: (i) a negative one for the filled states that exhibits only weak spectral modulations and (ii) a positive one characterized by strong unoccupied-state resonances. This pronounced difference is based on the impact of extra electrons shuttled from the Ag support into the cluster [195]. The amount of extra charge is 0.2|e| per atom [10] (or 26 electrons for the total nanoisland). In order to minimize the internal Coulomb repulsion between electrons, the electrons preferentially localize along the cluster perimeter [19, 193]. Consequently, the filled-state density is pushed from the island interior to its outer regions and only small dI/dV signals are detected in the center of the nanostructure. Contrarily, high intensity is found at the island perimeter as observed in dI/dV maps taken around the Fermi level in

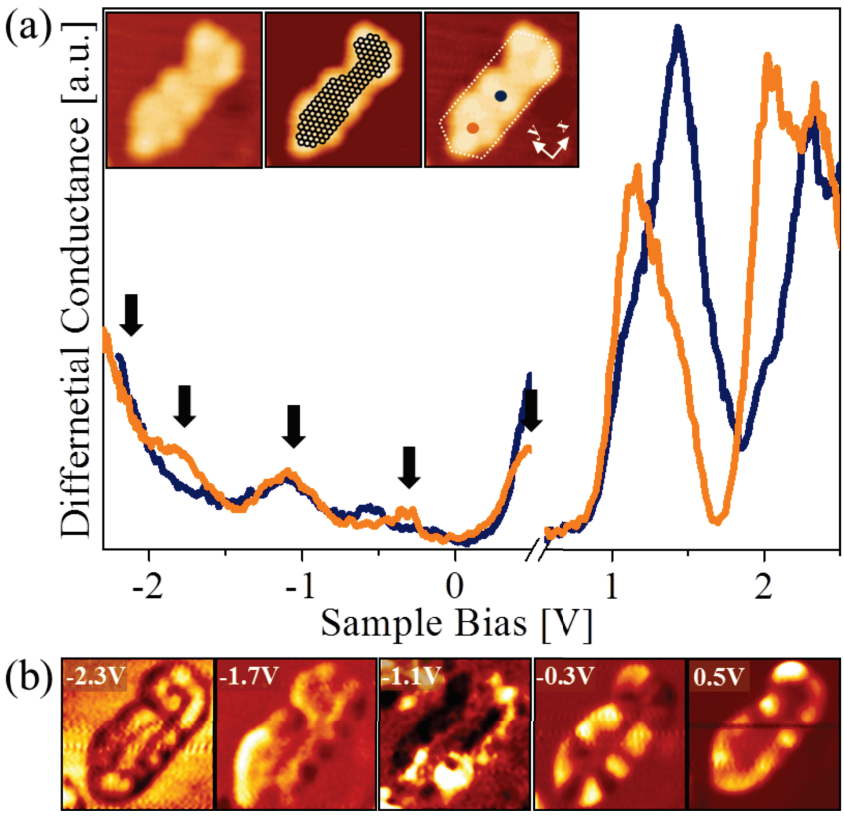

Fig. 4.2: (a) STS spectra taken in the center (blue) and lower part (orange) of a rectangular Au cluster shown in the inset (setpoints: -2.0 and +2.5 V for negative and positive polarity, respectively). The insets (from left to right) show a topographic image, a structure model and the quasi-rectangular outline of the island (7.5 x 7.5 nm^2, -0.1 V, 250 pA). The orange and blue dots indicate the tip position during STS. (b) dI/dV maps of the occupied states in the cluster with bias values corresponding to the arrows in the spectra.

Fig. 4.2b. The edges of the negatively charged Au island appear bright over a relatively broad bias window which indicates an enhancement of the filled-state density at the perimeter. The spectral intensity becomes maximal at the low-coordinated kink and corner atoms where the extra charges preferentially localize due to their larger distance to adjacent charge centers along the edge. Only a weak comparable effect is observable for the unoccupied states. There is only a weak indication for a Coulomb repulsion is observed and, hence, for a charge-redistribution toward the edges. As the effect of the edge states on negatively charged Au clusters is discussed in detail by X. Lin et al. [193]. This work focuses on the empty-state spectra.

Fig. 4.3a shows a dI/dV spectrum of the unoccupied cluster states. The most pronounced peaks are detected at bias values between 1.0 and 2.5 V. According to previous DFT calculations they correspond to the energy window of the Au $6p_z$ orbitals [11]. The energy region below is governed by Au $6s$-like QWS states that feature already high quantum numbers with numerous nodes in the orbital plane and are, therefore, difficult to observe in the STM [210]. On the other hand, the region above 2.5 V is governed by a strong overlap between Au QWS and MgO CB states and later with vacuum states in the tip-sample gap. This makes the identification and interpretation of the genuine Au states difficult. For the rectangular cluster depicted in Fig. 4.2, at least six dI/dV maxima can be identified lying at 1.05, 1.25, 1.45, 1.7, 2.0 and 2.3 V above the Fermi energy, all of them belonging to the Au $6p_z$ manifold (Fig. 4.3a). The energy position of the peaks is approximately constant across the island, reflecting their delocalized character. The exact peak positions were extracted by a deconvolution of the dI/dV spectrum into six Gaussians (gray curves). The very good match between the data and sum of Gaussians (orange curve) is also reflected by the good reliability factor $\chi^2 = 2.4 \cdot 10^{-4}$. The nominal peak width is 0.25 eV and might be explained by the presence of vibronic sidebands dressing the actual electronic resonance [103, 104, 211]. In contrast, the intensity of the dI/dV peaks sensitively depends on the tip position above the island as it is expected from the nodal structure of the underlying electronic states. The respective symmetry of the QWS has been revealed from dI/dV maps where the dI/dV signal was detected at selected bias voltages across the entire island (Fig. 4.3b). The lowest Au $6p_z$-type QWS at 1.05 V is characterized by an almost uniform intensity in the lower island part and a negligible signal in the upper half. For the second state at 1.25 V, the intensity pattern reverses and the upper part of the island turns bright. The QWS at higher energy are always governed by nodal planes, i.e. by dark stripes along the x- and y-direction in the

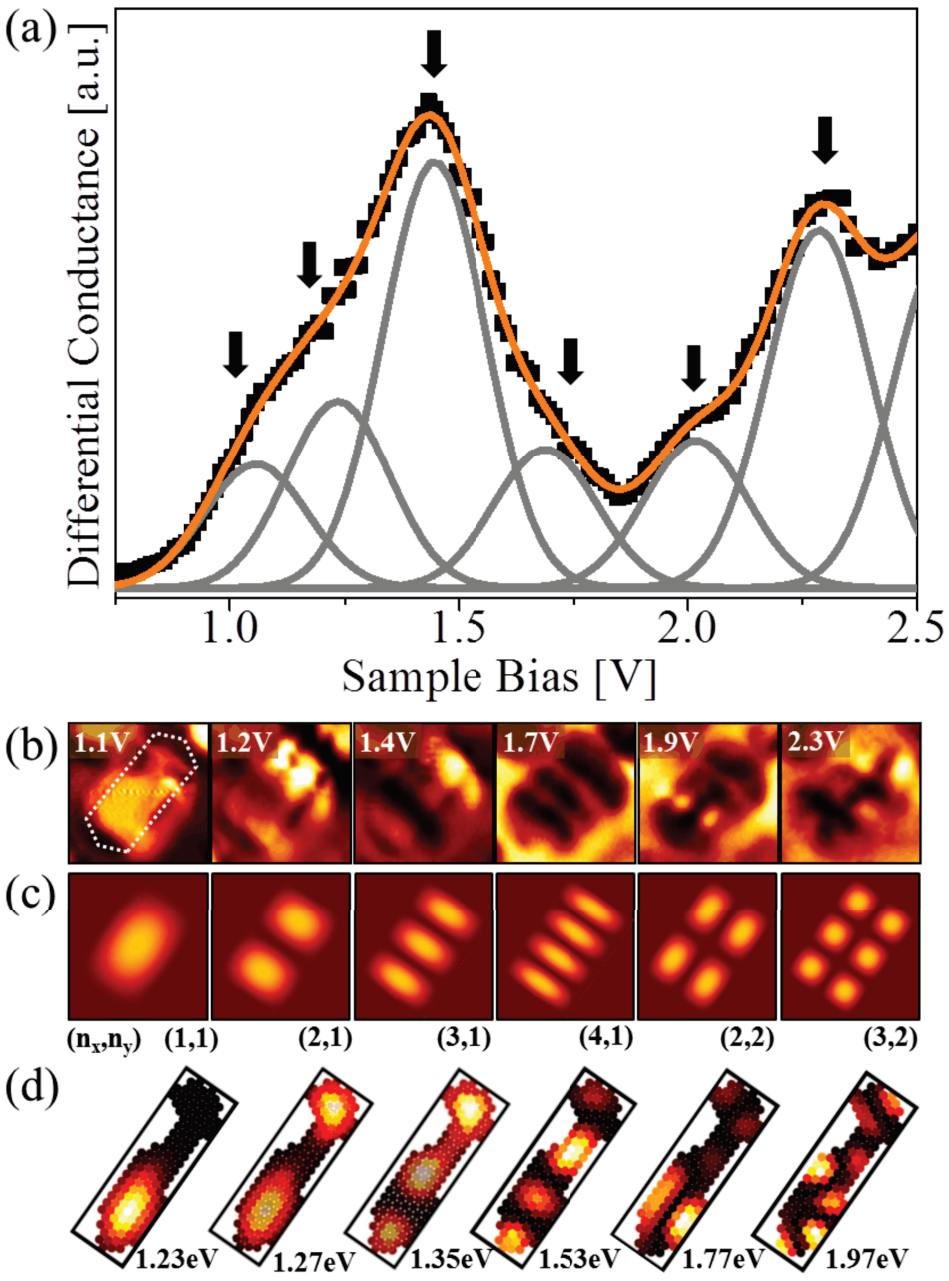

Fig. 4.3: (a) Empty-state spectra taken in the center of the cluster shown in Fig. 4.2. (b) corresponding dI/dV maps (7.5 x7.5 nm^2) measured at bias positions indicated in (a), and (c) corresponding states within the PIB model. (d) DFTB calculations showing the local-state density in the cluster [209]. Remark: The second and third maps result from a superposition of two closely spaced eigenstates of the system.

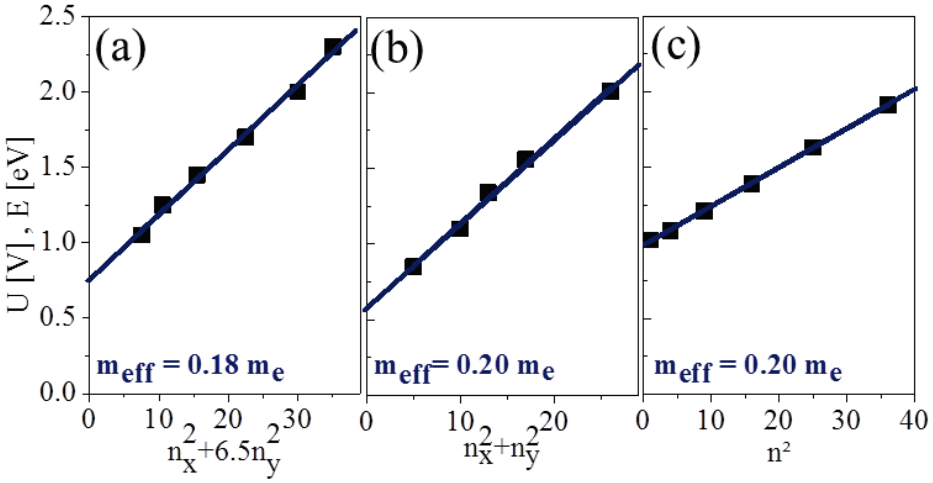

Fig. 4.4: Dispersion relations for the (a) rectangular (cf. Fig. 4.2), (b) triangular (cf. Fig. 4.5), and (c) quasi-linear cluster (cf. Fig. 4.6). The measured bias values are plotted against the squared quantum numbers of the corresponding PIB models.

dI/dV maps reflecting the quantization of electronic states in two dimensions. For instance, the third and fourth QWS display one and two vertical nodes perpendicular to the x-axis, whereas the fifth and sixth states show additional nodal planes perpendicular to the y-axis (cf. Fig. 4.3b). A simple PIB model is already sufficient to reproduce the sequence of the measured QWS. In first approximation, the cluster is treated as a ideal rectangular box with infinitely high walls. Hence, the wave functions and quantization effects are separable along the two orthogonal axes, x and y, and equation 3.3 changes to

$$E_{n_x,n_y} = E_0 + \frac{\hbar^2\pi^2}{2m_{eff}L_x^2}\left(n_x^2 + c^2 n_y^2\right) \tag{4.1}$$

with the measured aspect ratio $c = L_x/L_y = 2.5$. The eigenstates of the rectangular box can be fitted to the STS data (Fig. 4.4a). This yields an onset energy for the Au $6p_z$ quasiband of $E_0 = 0.75eV$ and an effective electron mass of $m_{eff} = 0.18m_e$. The latter value is comparable to the effective mass of the Au(111) surface state (0.22 m_e) [212] but is 2.5 times smaller than in monatomic Au chains on NiAl(110) (0.5 m_e) [67]. This discrepancy may be explained by the reduced dimensionality and the large interatomic spacing in 1D gold chains. In addition, the QWS symmetry predicted by the PIB model qualitatively matches the experimental results (Fig. 4.3b, c). In both, simulation and experiment, the first four eigenstates are characterized by 0–3

vertical nodes (n_x = 1,2,3,4), whereas the fifth and sixth experimental states exhibit an additional horizontal node together with one (2,2) and two (3,2) vertical nodes, respectively. This interpretation implies that two intermediate states, (1,2) and (5,1), are not resolved by the STM. Their overlap with neighboring QWS of different symmetry may cause this effect. Not surprisingly, a more precise analysis highlights substantial differences between the measured dI/dV maps and ideal PIB states which are a consequence of inhomogeneities in the cluster shape and hence cluster potential. A better match between theory and experiment can be achieved by calculating the lower-energy QWS by a DFTB approach [207] considering the exact atom configuration depicted in Fig. 4.2a. The computed LDOS maps shown in Fig. 4.2d reproduce the main features seen in experimental dI/dV maps. The first two eigenstates are confined to the lower and upper halves of the Au cluster, while the third state exhibits a pronounced nodal plane. The fifth and sixth state are characterized by an additional long-axis node. The remaining discrepancies are related to irregularities in the cluster shape that are not captured in the structure models derived from the STM images. It is especially difficult to define a precise edge configuration, although the nature of the edge may have a substantial influence on the overall electronic structure of the cluster. Furthermore, up to now a defect-free MgO film is assumed, neglecting possible perturbations due to defects such as oxygen vacancies [41]. A more reliable structure determination based on atomically resolved STM images as they could be obtained in later experiments (cf. Fig. 5.2) might lead to an even better match between experiment and theory.

4.3 Triangular Gold Clusters

The second sample cluster chosen in this work is an Au island of triangular shape with an edge length of 55 Å and an estimated atom number of 170 (cf. Fig. 4.5a, inset). In first approximation, the nanostructure can be described by an isosceles, right-angled triangle. This is the only triangular potential symmetry that analytically solves the Schrödinger equation and therefore enables an exact modeling of the experimentally observed QWS. In fact, the right-angled isosceles symmetry can be treated as a square potential cut along its diagonal. Therefore, the wave functions and quantization effects are fully separable along the orthogonal axes, x and y, with the additional boundary condition of inequality of quantum numbers $n_x \neq n_y$. The similarity to the rectangular box becomes evident also from the expression of eigenenergies

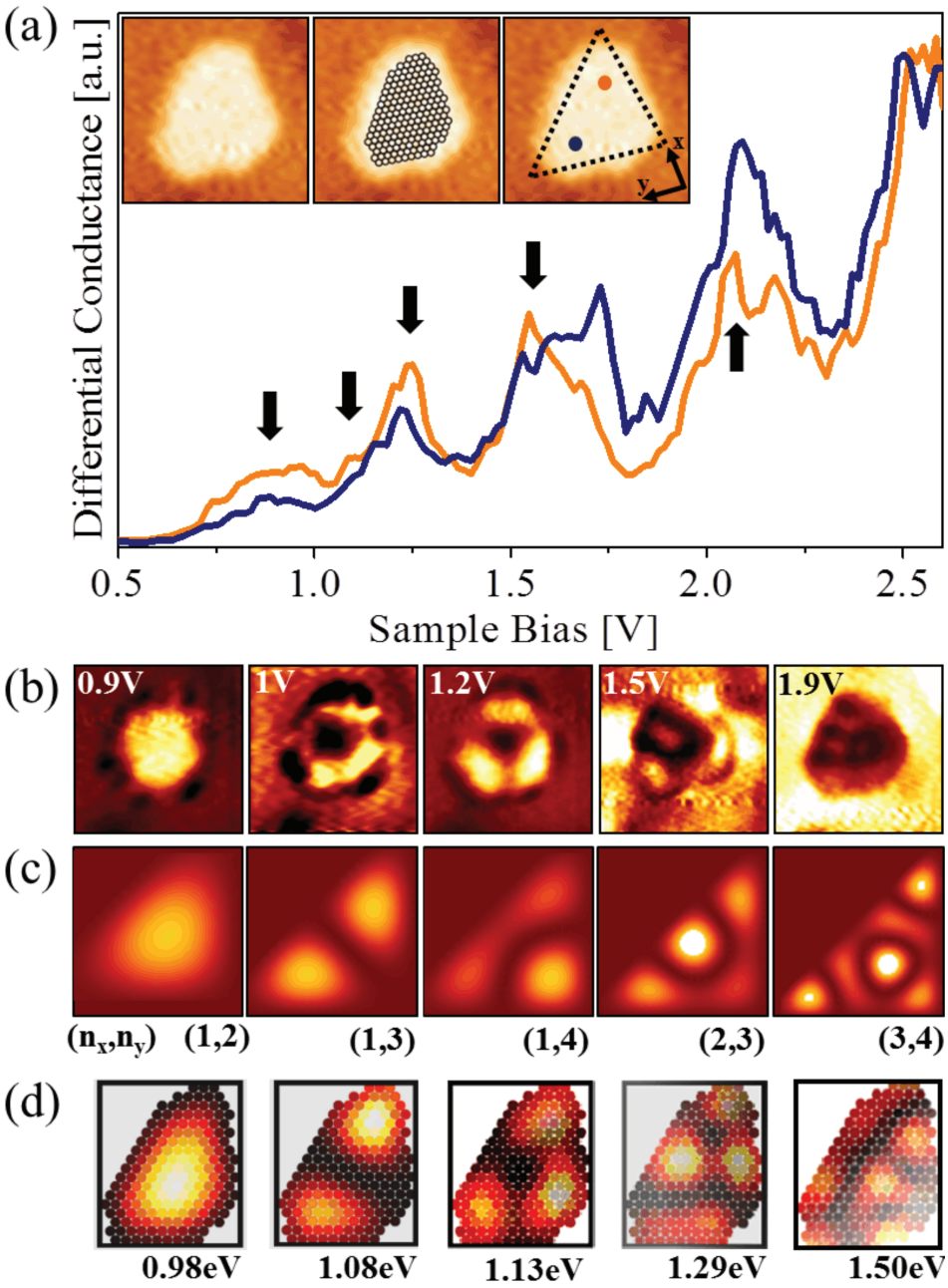

Fig. 4.5: (a) Empty-state spectra taken in the upper (orange) and lower (blue) parts of the triangular Au cluster shown in the inset and (b) corresponding dI/dV maps (8 x 8 nm^2) taken at the bias values indicated by arrows in the spectra. The symmetry of the QWS can be explained either with (c) the eigenstates in an isosceles, right-angled triangular box potential or with (d) DFTB calculations performed on a structure model of the Au island [209]. Here, the symmetry of the third, fourth, and fifth dI/dV maps result from a superposition of two adjacent eigenstates.

obtained from expression 3.3 [213]:

$$E_{n_x,n_y} = E_0 + \frac{\hbar^2\pi^2}{2m_{eff}L_x^2}\left(n_x^2 + n_y^2\right) \tag{4.2}$$

In the dI/dV spectra and maps shown in Figs. 4.5a and b five maxima could be detected in the energy range of the Au $6p_z$ state manifold lying at 0.9, 1.05, 1.25, 1.55 and 2.05 V. As above, the exact peak positions are obtained by a spectral deconvolution into Gaussians (not shown here). Plotting the peak energies vs. teh squared sum of quantum numbers in Fig. 4.4b yields the dispersion of states in the triangular nanoisland. The band onset energy of $E_0 = 0.6\ eV$ and an effective electron mass of $m_{eff} = 0.2\ m_e$ are similar to the values obtained for the rectangular box. Moreover, the low-energy eigenstates exhibit well-defined symmetries in the respective dI/dV maps and can be reproduced within the PIB model (Figs. 4.4b, c). A good qualitative match is given between the experimental dI/dV maps and the calculated pattern, representing the main maxima. While the ground state shows a homogeneous intensity distribution, two and three maxima are resolved for the second and third QWS. The fourth and fifth states show more complex intensity patterns which are characterized by a sequence of dark and bright spots. A further comparison shows the respective LDOS patterns computed with the DFTB approach in Fig. 4.4d. Especially, the first three QWS show a good match with the dI/dV maps, indicating the suitability of our theoretical approach to capture the physics of electron quantization. The third and fourth state can be convincingly reproduced by a superposition of two adjacent eigenstates, accounting for the fifth QWS in a reasonable manner. The good correspondence underlines the quasi-free electron character of the Au QWS, which renders them insensitive to small irregularities in the potential as a result of a much larger wavelength (about 30 Å) of the quantum mechanical wave function compared to a single Au atom (3 Å).

4.4 Quasilinear Gold Clusters

The last example discussed in detail is an elongated-curved Au island that may be considered as a model for a quasilinear quantum well. Its main axis (8.3 nm) is roughly three times longer than its short one (2.6 nm). The number of atoms is approximately 130 (cf. Fig. 4.6a, inset). As before, several dI/dV peaks are detected at positive bias lying at 1.0, 1.1, 1.2, 1.4, and 1.9 V (cf. Fig. 4.6a). The QWS can be compared with the eigenstates of a 1D PIB

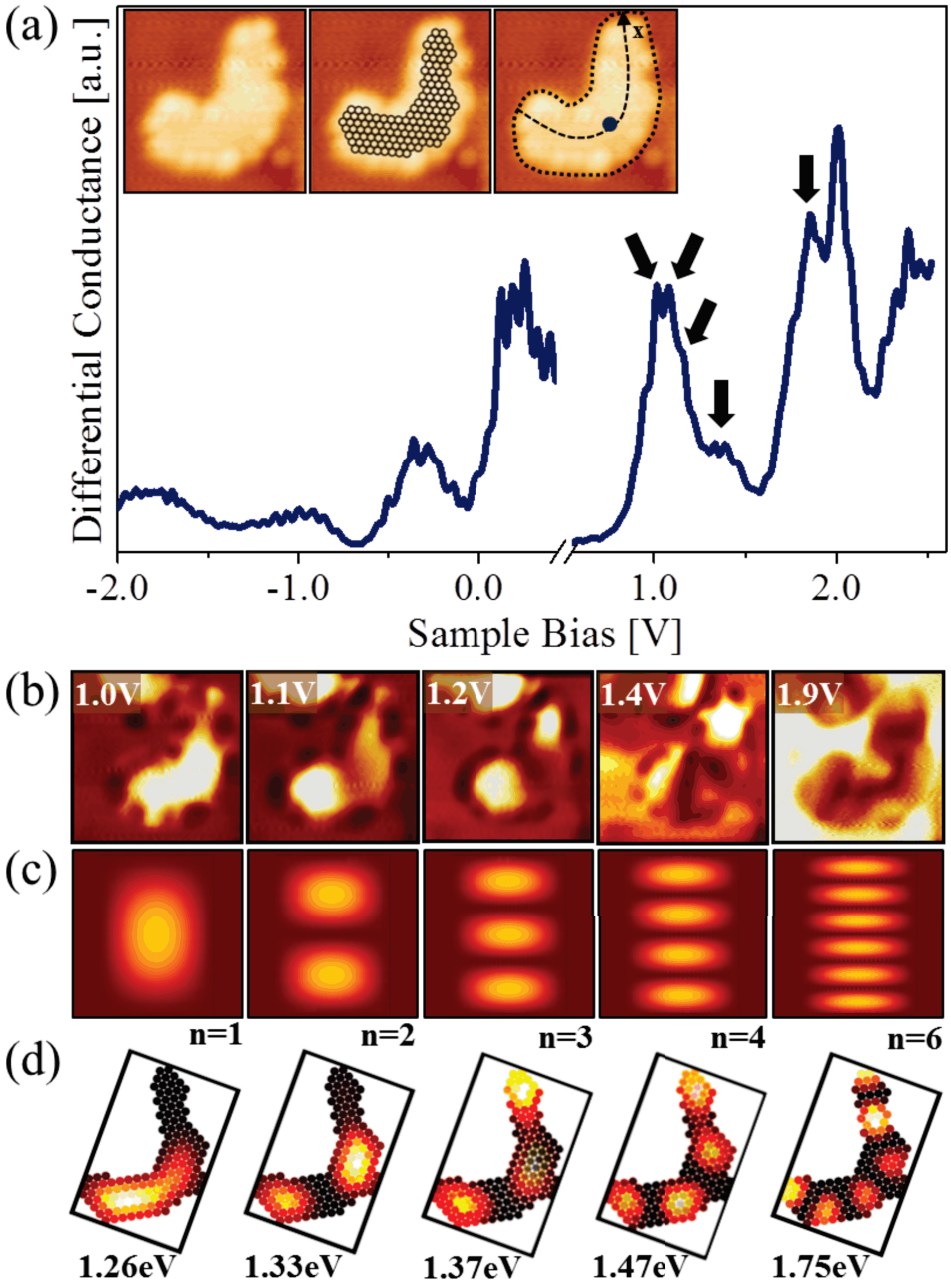

Fig. 4.6: (a) STS spectra taken in the center of the curved-linear cluster shown in the inset (9 x 9 nm^2). The first five maxima, obtained from a Gaussian deconvolution, are marked by arrows. (b) dI/dV maps (9 x 9 nm^2) taken at the determined bias positions indicated by arrows in the spectrum, (c) the eigenstates in an ideal 1D PIB model and (d) the respective LDOS maps calculated by a DFTB method. The third and fourth maps are superpositions of two adjacent states.

potential with infinitely high walls that depends anly on a single quantum number n [203]:

$$E_n = E_0 + \frac{\hbar^2 \pi^2}{2 m_{eff} L^2} n^2 \tag{4.3}$$

A linear fit of the exact peak position obtained from a Gaussian-deconvolution of the dI/dV spectrum (not shown here) to the squared quantum number n^2 yields a parabolic dispersion with an onset energy of $E_0 = 1.0\ eV$ and an effective electron mass of $m_{eff} = 0.2\ m_e$ for the QWS $6p_z$ manifold in the nanostructure (Fig. 4.4c). The density-probability distribution in an ideal, linear 1D box potential is described by charge-density waves with an increasing number of maxima and minima along the main axis with increasing quantum number n [203]. Thereby, the quantum number n equals the number of maxima as calculated for the ideal case in Fig. 4.6c. Despite obvious deviations from a truly 1D potential, this scheme can be still recognized at least for the lowest five QWS in the experimental dI/dV maps. Whereas the first two states show dI/dV intensity mainly in the lower part of the cluster, the signal localizes also in the upper part at around 1.2 V for the third QWS. With increasing bias, additional maxima and minima are detected along the main axis and the pattern becomes more complex. No horizontal nodal planes are observed up to the highest resolved state, reflecting the pseudo-1D nature of the confinement potential. As for the two other sample clusters, a better reproduction of the experimental dI/dV maps can be achieved by calculating the LDOS using a DFTB approach in Fig. 4.6d. The corresponding LDOS maps clearly reveal the increasing number of nodal planes along the cluster's main axis with increasing energy and quantum number n.

4.5 General Properties of Quantum Well States

A fundamental property of confined electron systems, represented here by small metal clusters, is the HOMO-LUMO gap. It is an intrinsic parameter describing the performance of nanocatalysts in chemical reactions and gives a measure for the metallicity [7, 192] of the clusters. Goodman and co-workers [5] showed for the first time for the LT CO oxidation to CO_2 on Au clusters on Titania, that the catalytic activity depends on the cluster size showing a maximum at 3.5 nm in the investigated size range of 1 to 6 nm. This sensitivity of the reaction results from quantum size effects in the supported Au clusters, as it is exactly the range where the metal to non-metal transition takes place.

The enhanced catalytic performance can be attributed to so-called resonance states that get optimally occupied at around 3.5 nm cluster size [214]. If the HOMO-LUMO gap gets too large (smaller clusters) or too small, i.e. too "metallic"(larger clusters), these resonance states are not sufficiently occupied and the catalytic activity drops below its optimal value.

4.5.1 Dependence of the HOMO-LUMO Gap on Cluster Size and Shape

To analyze now the interplay of the geometry and the electronic structure of planar Au clusters on MgO(001) thin films, a large data set of dI/dV spectra for various cluster shapes has been analyzed. The region of zero conductance around the Fermi level gives thereby the size of the HOMO-LUMO gap. As expected, the gap size decreases with increasing island size, a trend that becomes evident when plotting the dI/dV gap as a function of the estimated atom number n per island (cf. Fig. 4.7a). The observed trend has been reported before for clusters with circular shape [10]. There, the HOMO-LUMO gap exceeds 1.0 eV for clusters containing less than 20 atoms, and gradually decreased with increasing cluster size until it becomes zero for atom counts above 100 [10].[2] The weak point of this data set is that they have chosen clusters with only one fixed geometry, neglecting possible effects of the cluster shape on the HOMO-LUMO gap. Whereas the overall size evolution is easily visible in Fig. 4.7a, the data points exhibit a substantial scattering, especially in the region around 130 atoms. A functional relationship cannot be found easily. Obviously, the atom number is not the only parameter that influences the HOMO-LUMO gap and other properties such as the shape or non-monotonous shell-closing effects [192] have to be taken into account.

In a simplified picture, the shape effect may be explained by the difference in wave function overlap in compact (spherical) clusters as compared to open, elongated structures. In compact clusters, the number of interacting atoms in a fixed radius is larger which promotes faster gap closing. On the other hand, in elongated islands the number of NN is small, and the gap remains open for much larger sizes. This trend might be counterbalanced by symmetry effects, as highly symmetric clusters feature a quite large degeneracy of electronic states within a certain energy interval. If one imagines a more irregular shape

[2]The Δ values can differ with respect to reference [10] due to a different definition of the band gap. Whereas X. Lin et al. [10] estimated Δ directly from the zero-bias gap in the dI/dV spectra, Δ is defined here as the distance between HOMO and LUMO level, as extracted from spectral deconvolution into Gaussian curves.

then the degeneracy of states is partially lifted which leads to a larger number of states with different energies in the same energy interval and, consequently, to a reduced energy distance between the individual states. Hence, symmetry effects inhibit gap closure. Furthermore, symmetry effects are closely related to the presence of magic cluster sizes that are characterized by closed-shell configurations and pronounced HOMO-LUMO gaps. For gas-phase clusters, an oscillatory behavior of the gap has been revealed with cluster size, a trend that could not be reproduced for supported nanoparticles so far [192, 215].

To account for the interplay between size/shape and the HOMO-LUMO gap, a suitable descriptor that catches the relevant geometric properties of the 2D clusters has to be found. In former experiments, the size dependence has been investigated [10] and the trend of a decreasing gap with increasing cluster size is reproduced in the present data set (Fig. 4.7). Furthermore, four sample clusters of the same size (130 atoms) have been selected in Fig. 4.9, ordered from (a)-(d) from high to low symmetry. The broadest data scattering for the energy gap Δ as a function of the number n of atoms in the cluster Δ-n is observed exactly for these clusters, showing the strong influence of the cluster shape on the electronic structure. As shown in Fig.

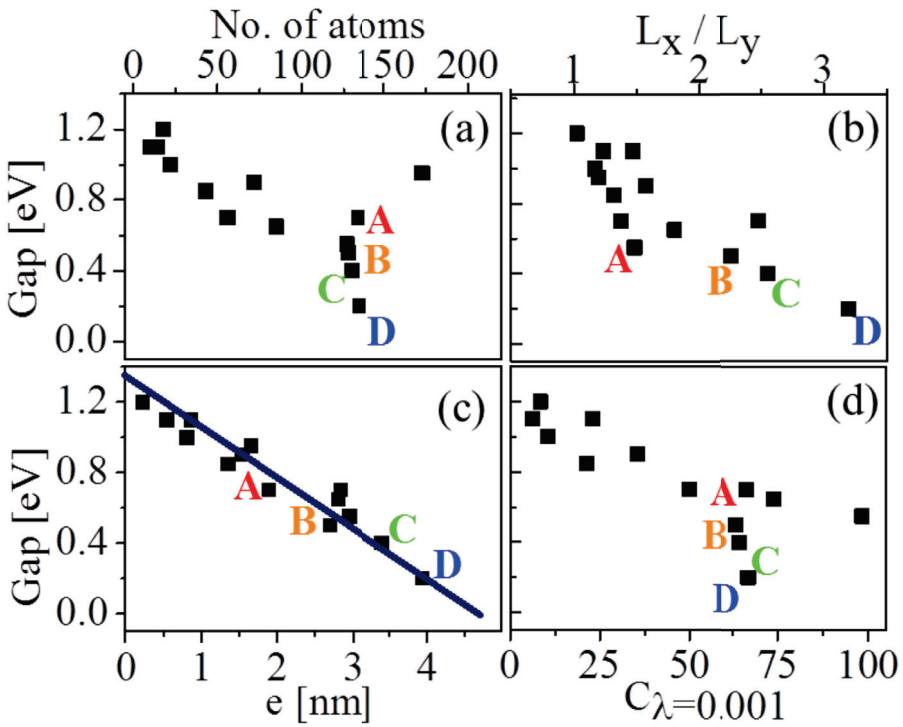

Fig. 4.7: Size and shape dependence of the HOMO-LUMO gap in Au clusters.

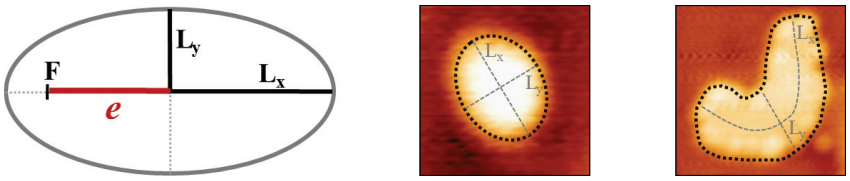

Fig. 4.8: Approximation of arbitrarily cluster shapes by an ellipse (center) or parabola (right), characterized by their semimajor and semiminor axes L_x and L_y, respectively. The linear eccentricity e gives the distance between focal and center point.

4.8, clusters with arbitrarily shape can be approximated in general as an ellipse or parabola, which are similar objects from a mathematical point of view. The only difference is that a parabola has a negative focal length whereas an ellipse has a positive one. A first parameter describing the cluster shape is the ratio of long and short axis L_x/L_y as a direct measure of the island shape. Plotting the HOMO-LUMO gap as a function of this parameter in Fig. 4.7b does not satisfactory reduce the scattering of data points with respect to the Δ-n diagram. This is due to the fact that the axis ratio neglects the island size. For example, a cluster of twice the size has an identical ratio $2L_x/2L_y = L_x/L_y$ although the number of interacting atoms increases. Other shape parameters, such as the ratio between perimeter length and island area, do not improve this correlation (not shown here). In a next step, the linear eccentricity e, i.e. the distance between the focal and center point of an ellipse, calculated as

$$e = \frac{1}{2}\sqrt{L_x^2 - L_y^2} \tag{4.4}$$

has been chosen as a descriptor for the HOMO-LUMO gap. It suits well since it contains both size and shape elements and carries the dimension of a length. Moreover, it is a common parameter to analyze the asymmetry of gas-phase clusters [215]. Plotting the Δ-e dependence shown in Fig. 4.7c leads to an almost perfect linear relationship with negligible scattering of the data points. The good correlation with the gap value suggests that the linear eccentricity can be used to predict HOMO-LUMO gaps in metal clusters without measuring their particular gap size via STS. However, a disadvantage of this descriptor is its purely empirical character that lacks any insight into the quantum mechanical nature of the problem.

A microscopic parameter that may capture the origin of the gap is the atom coordination number, i.e. the number of first, second, third, etc. NN atom pairs in the island. Intuitively, one would expect that an increase in coordination enhances hybridization among the atoms and results in a more

rapid crossover into a metallic ground state. To analyze this effect, the pair-correlation functions (PCF) for four sample clusters have been calculated and are shown in Fig. 4.9. The different shape of the sample clusters becomes visible in the tail of the PCF, i.e. by the pairs with relatively large distances. Contrarily to this, the number of NN and next-NN pairs depends only weakly on the cluster shape. Using the PCFs a definition of a mean coordination number c_λ for each island was possible:

$$c_\lambda = \sum N(d) \cdot e^{-\lambda d} \tag{4.5}$$

with N being the number of neighbors with distance d. The decay constant λ has been determined by searching an adequate linear relationship between Δ and λ. Even for the best parameter λ=1$\cdot 10^{-4}$ Å, the correlation between the size of the HOMO-LUMO gap and the coordination number remains poor (cf. Fig. 4.7d). It seems that hybridization between the atoms is not the only nanoscopic reason for a gap closure in the clusters which may be explained by the fact that symmetry and shell-closing effects are neglected. Obviously, the empirical parameter of the linear eccentricity catches these features with respect to the gap size better than the coordination number. However, further work is needed to identify an adequate quantum mechanical parameter that mediates cluster geometry and gap size in Au nanostructures.

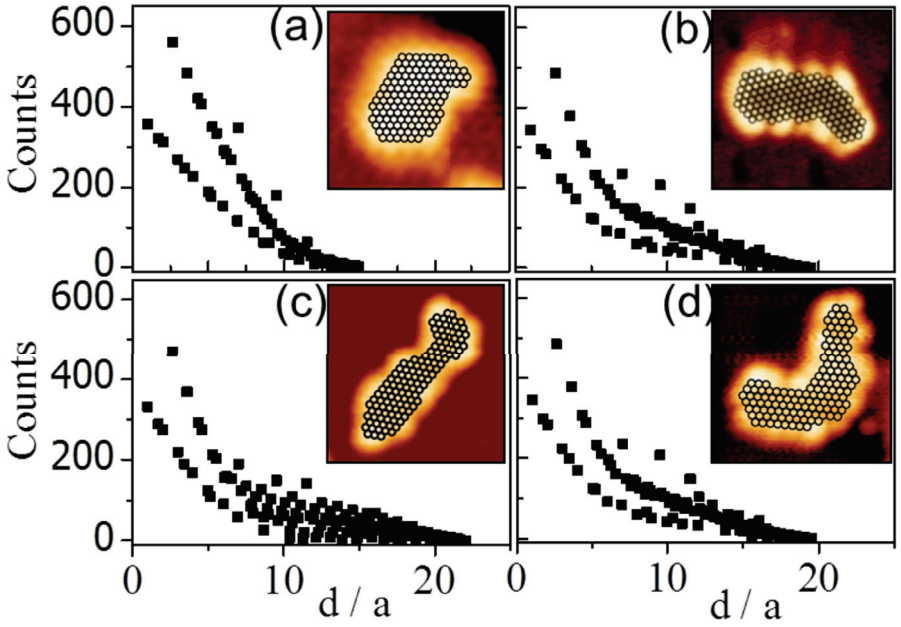

Fig. 4.9: Pair correlation functions of four sample clusters with arbitrary shape

4.5.2 Estimation of the Confinement Potential

Up to now only potential wells with infinite depth were assumed. This facilitates an analytical description but oversimplifies the experimental situation. Whereas in bulk gold the real potential depth of the Fermi electron gas is determined by the workfunction [155], this value becomes smaller for Au clusters of finite size. The following gives a realistic estimation of the potential depth by analyzing the spillout of Au QWS beyond the geometrical boundaries of the nanoparticle.

As discussed in chapter 3.2.2 and shown in Fig. 3.9, the density probability of electrons $|\psi|^2$ decays exponentially when moving beyond the island edge of the cluster (here y, referring to Fig. 4.10):

$$dI/dV(y) = |\psi_{exp}(y)|^2 \propto e^{-2\alpha^* \cdot y} \tag{4.6}$$

In the experiments, this behavior is governed by two decay contributions, α_{qws} and α_{stm}, related to the QWS and the STM, respectively. They sum up to the total decay observed in the STM: $\alpha^* = \alpha_{qws} + \alpha_{stm}$. Whereas the STM contribution α_{stm} accounts for the in-plane decay of the wavefunction overlap between the tip and sample, the QWS decay length α_{qws} is a direct consequence of the finite potential depth. The latter provides a direct measure of the true potential height V_0^* (according to equation 2.5):

$$\alpha_{qws} = \sqrt{\frac{2m(V_0^* - E_{qws})}{\hbar^2}} \tag{4.7}$$

with E_{qws} being the eigenenergy of the state as determined from the dI/dV spectra. Analyzing now the wave function decay of the sample cluster shown in Fig. 4.10 in y-direction, one can identify two dI/dV maps having the same quantum number $n_y = 1$ (Fig. 4.10b,c). The spill-out of the square wave function beyond the boundaries of the cluster is clearly seen. By an exponential fit of the decay in the two dI/dV maps, the equation system

$$\alpha^*_{(1,1)} = \alpha_{(1,1)} + \alpha_{stm}$$

$$\alpha^*_{(2,1)} = \alpha_{(2,1)} + \alpha_{stm}$$

can be solved with help of equation 4.7 by eliminating α_{stm} via subtraction of both equations. This leads to the following expression for V_0^* which can be

solved numerically.

$$\frac{\hbar}{2m_e}\left(\alpha^*_{(1,1)} - \alpha^*_{(2,1)}\right) = \sqrt{V_0^* - E_1} - \sqrt{V_0^* - E_2} \tag{4.8}$$

Hence, the potential depth of the finite well can be calculated as $V_0^* = 3.75\ eV$. Adding the onset energy $E_0 = 0.75\ eV$ of the cluster as obtained from the dispersion shown in Fig. 4.4a, the upper edge of the confinement potential is estimated to be 4.5eV above the Fermi level. This value is 0.6 eV smaller than the workfunction of bulk gold (5.1 eV) which may have two reasons: (i) Au islands in the investigated size regime are too small to develop their own vacuum energy and still feel the reduced workfunction of the surrounding MgO/Ag(001) film (3.5 eV)[183]. (ii) The Au electrons may escape the potential well by moving into the MgO conduction band and hence, the cluster potential is defined by the oxide electronic structure rather than the vacuum energy.

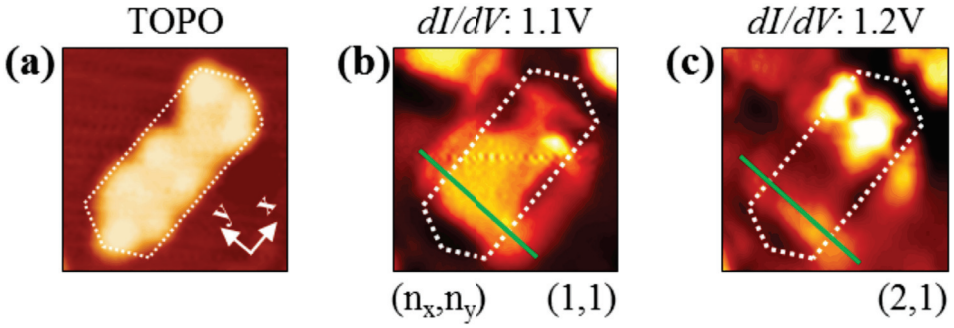

Fig. 4.10: (a) Topographic image of the rectangular cluster in Fig. 4.2 with its geometrical boundaries indicated by the white hexagon. dI/dV maps of the (b) first and (c) second state consisting of equal quantum number $n_y = 1$. The line along which the decay parameter has been fitted is indicated by green.

4.6 Conclusions

In this chapter, the electronic structure of planar, monolayer-high Au clusters on MgO/Ag(001) ultrathin films containing between 50 and 200 atoms has been analyzed. A series of pronounced peaks in STS detected above the Fermi level has been assigned to QWS arising from the of Au $6p_z$ manifold of the individual atoms. Their energy position and node structure was convincingly reproduced with simple PIB models of rectangular, triangular and linear symmetry. This agreement despite obvious irregularities in the cluster shape

reflects the free-electron character of the Au conduction electrons, which renders their properties insensitive to details of the potential. An even better reproduction of the experimental data was achieved by modeling the Au electronic structure with a parameterized DFTB approach that takes into account the true atom configuration as estimated by STM topographic measurements. On the basis of the experimental results, an empirical relationship between the size and shape of Au nanoislands and the HOMO-LUMO gap was established, using the linear eccentricity as a descriptor. With this scheme, it is now possible to predict the "metallicity" of oxide-supported Au nanoparticles only by measuring the cluster's topography and hence an important factor in evaluating their performance in chemical reactions.

Chapter 5

Substrate versus Dopant-Induced Charging of Gold Clusters

A permanent charge transfer into metal nanoparticles on oxide supports has been associated with a number of unusual morphological, electronic and catalytic properties of these systems. Two fundamental charging routes have been identified so far: (i) electron tunneling through ultrathin oxide layers on metal supports and (ii) charge donation by single-ion impurities embedded in a bulk-like oxide. In this chapter, it has been investigated in detail whether both routes result in the formation of charged nanoparticles with identical properties. For this purpose, Au nanoislands were prepared either on 1-2 ML thin MgO/Ag(001) or 25 ML thick CaO/Mo(001) films doped with Mo impurities. The experiments on the CaO film have been performed by Dr. Yi Cui in another STM at the FHI's Chemical Physics department. The morphological and electronic properties of the Au islands observed in the STM, show in both cases pronounced electron confinement effects that arise from the quantization of one and the same Au electronic band. Moreover, clear experimental signatures for a substrate-driven charge transfer were observed on the two oxide films, such as a monolayer growth of the Au ad-islands and a characteristic contrast reversal in the oxide region surrounding the charged islands. The results provide evidence that charged nanostructures feature identical properties independent of the origin and nature of the transfer-electrons, indicating that ultrathin oxide films may be used as model systems for doped bulk oxides as used in heterogeneous catalysis.

5.1 Structural properties

In the following, Au islands with similar size and shape on (i) ultrathin MgO films and (ii) thick CaO films are compared. Atomically resolved images of different Au islands typically reveal a hexagonal atom arrangement with a periodicity 2.9 Å, indicating that the exposed Au layer is of (111) type and does not adopt the square symmetry of the oxide lattice (Fig. 5.1, 5.2). The threefold lattice symmetry of Au(111) also dictates the hexagonal equilibrium shape of the ad-islands. A comparison of hexagonal Au clusters of 5-7 nm diameter (corresponding to 200-400 atoms) on both oxides exhibits similarities in the overall shape but displays pronounced differences in the structural and electronic properties of the Au clusters. The CaO-based islands show pronounced stripe patterns with 7.5 Å spacing that appear in three orientations rotated by 120°. The pattern is ascribed to a hexagon-on-square Moiré structure, in which six Au rows along the CaO[100] direction overgrow three unit cells of oxide support (Fig. 5.1c) [217, 218]. The crests of the pattern are formed by Au atoms in calcium (Ca) top positions. The valleys of the structure are governed by Au atoms in O top and various hollow sites. As two crests exist in each Moiré cell, the distance between adjacent stripes (7.5 Å) is only half of the unit cell length (15 Å). By contrast to this, no superstructures are observed for Au islands on MgO. The theoretical Moiré periodicity in this case would be of the order of 20 Å, corresponding to eight Au rows overgrowing five MgO unit cells. The invisibility of the Moiré pattern on MgO can be explained by the flatness of the potential landscape for adsorption on the MgO monolayer, for which almost identical binding properties have been calculated for Au atoms on Mg / O top and hollow sites, respectively [195].

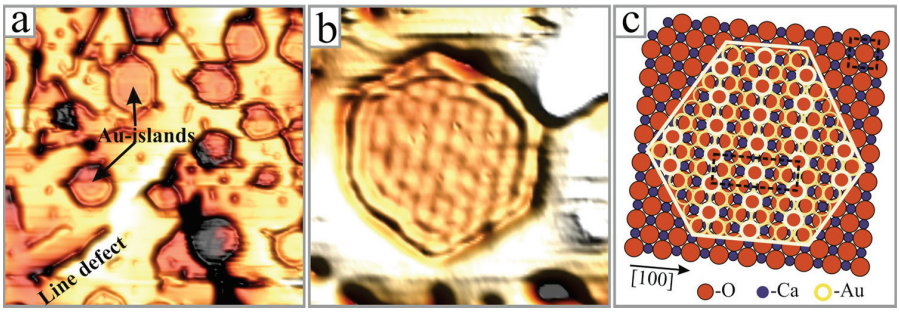

Fig. 5.1: Pseudo-3D STM topographic images of (a) several (40 x 40 nm^2) and (b) a single Au monolayer-island (12 x 12nm^2) on a 20 ML, Mo-doped CaO film (4.0 V, 15 pA). The stripes in (b) are assigned to a Moiré pattern formed between the hexagonal Au(111) and the square CaO(001) lattice, as modeled in (c). [216]

Moreover, a Moiré periodicity that comes close to the lateral dimensions of the Au cluster makes its observation difficult.

Apart from the internal structure revealing a hexagonal atom arrangement (cf. Fig. 5.2e), also the general appearance of the Au islands with respect to the surrounding oxide displays pronounced, bias-dependent differences. On both supports, the Au nanosheets undergo a contrast reversal from protruding islands at negative and small positive bias (cf. Fig. 5.2b) to faint depressions at elevated positive voltage (cf. Fig. 5.2c) [22]. The Au islands appear bright as long as the imaging bias lies inside the oxide band gap and below the vacuum states above the oxide surface. At around 3.5V, the contrast reverses as the conductivity through the Au islands drops below the one of the pure film. The conductance drop can be explained with the high workfunction of the Au islands with respect to the oxide films that shifts the highly conductive vacuum states [219] out of the accessible bias window for electron transport between tip and sample [22]. The change in contrast is enhanced especially at the cluster perimeter. While the island rim appears brighter than the interior in the low-bias regime, reflecting the presence of low-lying edge states at the under-coordinated Au atoms [193], it turns dark when crossing the conduction band onset of the oxide film at higher bias. The troughs surrounding the Au nanostructures are hereby much deeper and broader on the CaO than on the

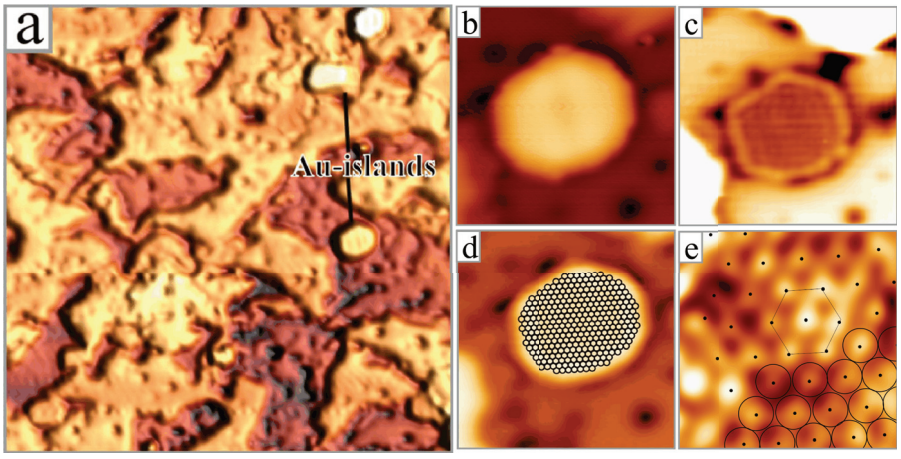

Fig. 5.2: (a) Pseudo-3D STM topographic overview image (80 x 80 nm^2, 1.7V) and topographic images of a single Au monolayer-island (12 x 12 nm^2) at (b) 1.0 V and (d) 3.4 V on a 2 ML MgO film (1.7 V, 15pA). (d) Approximation of the atom count in the island by filling its area with a hexagonal closed packed pattern of 2.89Å spacing, as in bulk Au(111). The atom number has been determined to be 319. (e) shows an atomically resolved image on top of an Au cluster on the MgO/Ag(001) ultrathin film revealing a hexagonal atom arrangement.

MgO supports. This effect can be understood by the local band bending in the oxide film in presence of the charged Au deposits.

5.2 Electronic properties

Both, the MgO and CaO-supported Au islands are characterized by a quantized electronic structure that dominates dI/dV spectra and spectroscopic maps of the nanostructures [10, 61]. For a MgO-supported Au island with approximately 300 atoms, a series of dI/dV maps probing the unoccupied LDOS at positive sample bias is shown in Fig. 5.3. Starting from 1.0 V, the initially featureless conductance behavior exhibits concentric rings that are increasing in number with bias voltage. Particularly nice examples can be found at 1.0, 1.6 and 2.0 V, when one, two and three dark rings become visible around the center (Fig. 5.3b). The rings exhibit also a radial fine-structure, characterized by nodal planes that cut thorough the island center and again increase in number with increasing bias. Similar conductance patterns have been revealed for hexagonal metal islands on thin oxide films [10], but also on bulk metal crystals before [66]. The features have been interpreted as stand-

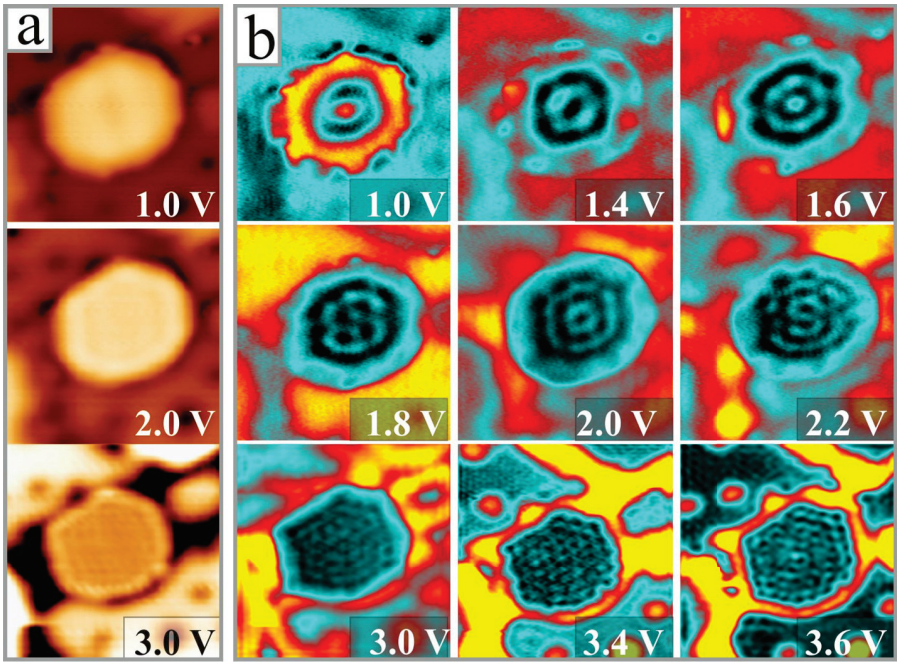

Fig. 5.3: (a) Topographic and (b) conductance maps of an Au island taken at different bias voltages on MgO/Ag(001) ultrathin films (1 2x 12 nm^2). Note the bias-dependent evolution of a standing wave pattern inside the island.

ing wave patterns that arise from a confinement of the Au 6*sp* electronic band in the metal nanostructures. The quantization phenomenon can be described analytically for a hexagonal potential well with infinitely high walls, yielding a linear energy dependence of the eigenenergies on the quantum number n [201]:[1]

$$E_n = E_0 + \frac{n}{\Omega^* m_{eff}} \tag{5.1}$$

Here, E_0 and m_{eff} are onset energy and effective mass of electrons in the Au 6*sp* band, respectively, while $\Omega^* = \Omega/10.8$ denotes the area of the 2D nanoisland.[2] To compare experimental and theoretical dispersion relations of the quantized electron band, the energy position of the Au energy levels is determined by measuring the distance of maxima/minima of cuts through the bias-dependent dI/dV maps. Thereby, a characteristic wavelength $\lambda_{dI/dV}$ and the associated wavenumber $k = \frac{\pi}{\lambda_{dI/dV}}$ as a function of bias have been extracted. [3] In this way, the k-value of the particular state is extracted. By analyzing the data one finds a linear dispersion for the electronic band underlying the observed standing wave pattern. The band onset was fitted to 0.1 eV, while its slope, accounting for the mobility and localization of electrons in the band, has been determined to be 0.69Vnm (cf. Fig. 5.4a). Both values agree well with earlier results acquired for single-layer Au islands on thin MgO supports discussed in chapter 4 and ref. [61]. Moreover, the respective band can be located directly in the band structure of bulk gold, as calculated with a RFPLO[4] approach by Häkkinen [220]. The (111) surface, representing our Au islands in real space, converts into a hexagonal plane centered on the L point in the irreducible Brillouin zone shown in Fig. 5.4d. The quantized band in this study proceeds from the zone center towards the edge, which means along the

[1] Ref. [201] describes electron confinement in a hexagonal Ag island on an Ag(111) surface. The quantization of the electronic structure arises thereby from a surface state located inside the band gap. This state is hence electronically decoupled from the substrate. The dispersion for the ideal hexagon is expressed by $E_n = E_0 + \frac{\lambda_n}{\Omega m_{eff}}$. In first approximation, the eigenenergies λ_n can be linearly fitted by $n = 10.8n + 5.9$ yielding to the equation used in the text.

[2] In ref. [201] are used atomic units, here are used SI units.

[3] Remark: The dI/dV signal measured in the STM is proportional to $|\psi|^2$. Consequently, phases of the wave functions are not observable in the STM and the intensity minima in dI/dV maps indicate the nodal planes of the wave function. As a result, the measured wave length is half of the real wave length, $\lambda_{dI/dV} = 1/2 \cdot \lambda_{real}$, resulting in the expression used in the text.

[4] RFPLO refers to a relativistic full-potential local-orbital approach used in the DFT calculations.

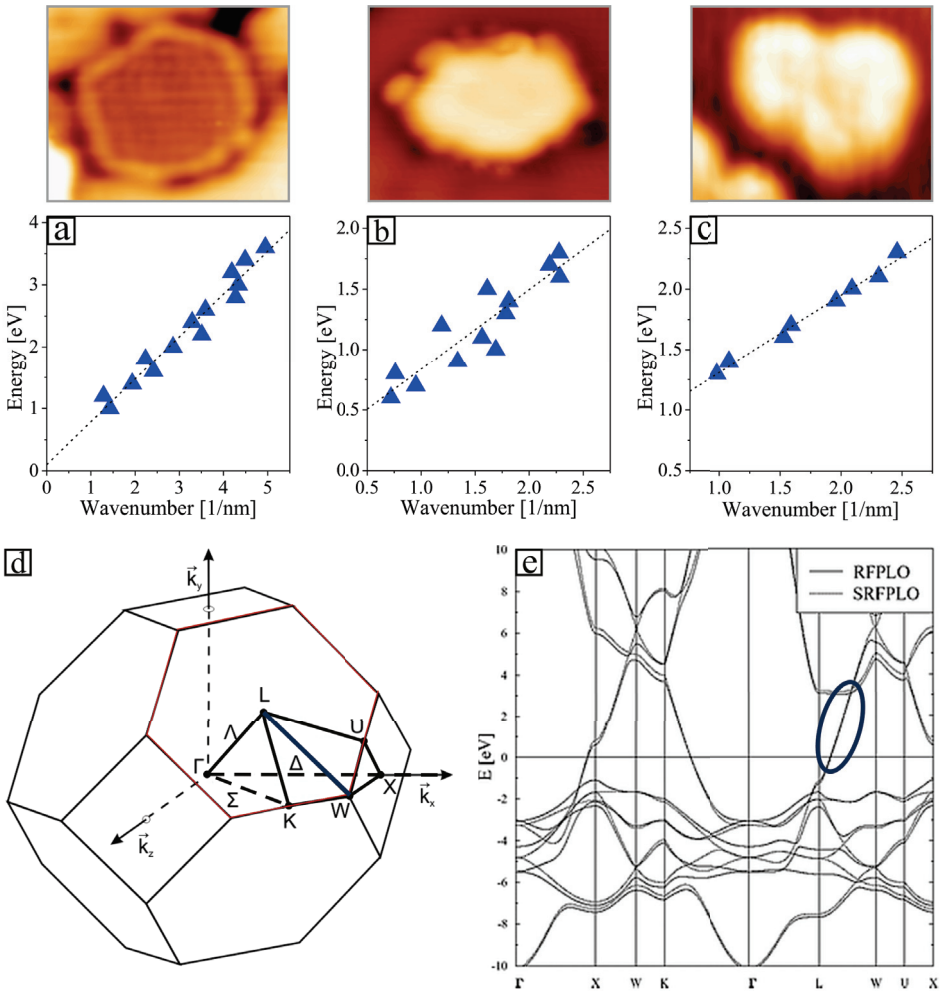

Fig. 5.4: (a-c) Experimental dispersion relations of QWS in three differently sized Au clusters on MgO/Ag(001) ultrathin films. The approximate atom count in the islands decreases from 300 in (a) to 200 and 44 in (b,c). The data for cluster (a) has been derived from dI/dV maps shown in Fig. 5.3. (d) shows the irreducible Brillouin zone in reciprocal space and (e) the calculated band structure for bulk gold, taken from ref. [220]. The electronic band that experiences lateral quantization in the clusters is marked by a blue ellipse. The band properties in both, bulk gold and monolayer islands, agree to a large extent.

LW direction in reciprocal space. The calculated band structure in Fig. 5.4e contains indeed a band in the expected energy range with properties largely following the signatures of the experimental state manifold. As expected, the band is of Au 6sp character, i.e. parabolic at the band onsets and almost linear in the intermediate regions. Its dispersion in the linear region can be approximated by a slope of 0.6 Vnm which is comparable to the measured value of the cluster. The main deviation between experiment and theory concerns the band onset, which is at -1.3 V in the RFPLO calculation [220], but close to the Fermi level in our STM study. This discrepancy can be assigned to a quantum size effect since the band onset scales directly with the diameter of Au islands on the MgO support. The trend is exemplified with the three dispersion relations measured for differently sized Au islands. While the smallest one (44 atoms, Fig. 5.4c) has a band onset at 0.6 eV, this value shifts to 0.2 and 0.1 eV in islands containing 200 and 300 atoms, respectively (Figs. 5.4a, b). Apparently, the depth of the quantum well is still governed by the finite atom number in the deposits, i.e. it approaches and finally crosses the Fermi level with increasing island size. Interestingly, the effective electron mass and hence the overlap of the adjacent Au electronic states, does not depend on the island size and remains constant in all three cases. Moreover, the absence of atomic planes below and above the monolayer islands (2D material) seems not to have drastic consequences on its in-plane electronic structure, as the derived band properties are well reproduced by the calculations for bulk gold (3D material).

In analogy to MgO-supported nanostructures, the electronic properties of Au islands grown on CaO supports are discussed in the following. Just to recall, the main difference between both oxide systems is the film thickness which is about 20 times larger in the case of CaO. The deposits are both expected to be electron-rich as a flow of electrons is guaranteed towards the nanogold either from the Ag(001) support below the ultrathin MgO film or from Mo donors embedded in the CaO matrix. Furthermore, CaO-supported clusters display characteristic standing wave patterns as well (cf. Fig. 5.6). However, the quality and clearness of dI/dV maps is significantly lower due to the limited transmissibility of the thick oxide for electrons. In fact, dI/dV mapping can only be performed at bias voltages close or above the onset of the oxide conduction band. For bias voltages lying inside the oxide band gap a high-quality data acquisition is hardly possible due to the unstable tunneling conditions. Despite the higher level of disorder, the wave patterns on CaO-supported Au islands can be analyzed in a similar manner as for the MgO via a extraction of $\lambda_{dI/dV}$ and correlated bias-dependent k-values. The

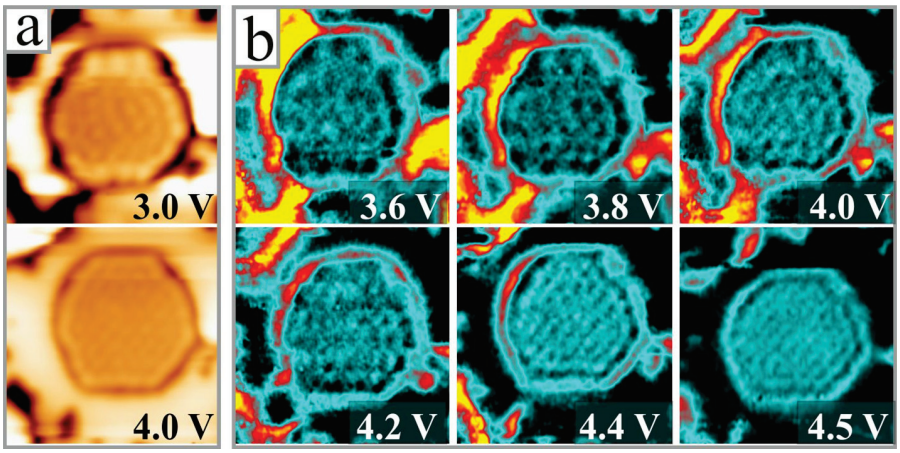

Fig. 5.5: (a) Topographic and (b) dI/dV maps of an Au cluster taken at different bias voltages on self-doped CaO/Mo(001) films (12 x 12 nm^2). Note the bias-dependent evolution from a standing-wave into a Moiré pattern on top of the island. [216]

so determined dispersion relation for the quantized band in CaO-Au islands shown in Fig. 5.6a deviates clearly from the one of the MgO-Au system discussed before. Firstly, the obtained fit values for band onset (1.5 eV) and effective electron mass (0.8 Vnm) are much higher than for the MgO-supported islands (0.1 eV, 0.66 Vnm), although clusters of similar dimension were chosen. Secondly, the dispersion relation is linear only up to a critical bias value of 4.2 V and becomes constant at higher voltages. The kink in the $E - k$ diagram occurs at k=3.8 nm^{-1}, which corresponds to the inverse periodicity of the Moiré pattern. It seems that the electron waves lock into the topographic line pattern observed on the CaO-Au islands. In other words, the topographic constraints on the Au surface result in a new boundary of the Brillouin zone that sets an upper bound for the k-vector of the Au 6sp electronic band [221, 222]. Given the rather large differences in the Au electronic properties with respect to the MgO support the question arises whether both systems can still be described within the same physical frame.

The following paragraph addresses the apparent deviation in the electronic structure which can be traced back to the better electronic screening of the CaO- versus the MgO-supported Au islands and leading to reversible shifts of the Au electronic states in the tip-electric field. In general, STM experiments on insulating oxide films involve electron transport through a double barrier junction, consisting of the vacuum gap between tip and ad-island and the oxide gap underneath the gold [94]. The two barriers give rise to a voltage division in the junction V_{vac}/V_{ox} that can be calculated by the film thickness

and dielectric response of the dividing gaps [95, 97]:

$$\frac{V_{vac}}{V_{ox}} = \frac{d_{ox}}{\epsilon_{ox}} \cdot \frac{\epsilon_{vac}}{d_{vac}} \tag{5.2}$$

Consequently, only a fraction of the applied bias drops in the vacuum barrier of the STM, while the substantial part decays in the oxide film by bending its electronic bands towards the Fermi level of the tip (cf. Fig. 5.6b). The Au electronic system floats now between the two junctions and internal energies of the system, as the band onsets, cannot be defined on an absolute scale anymore. In order to compare directly the MgO and CaO-supported clusters, the measured energies have to be corrected for the band-bending effects by inserting the mean thickness of 2 ML MgO (4 Å) and 25 ML CaO films (50 Å) as well as the oxide dielectric constant of $\epsilon_{ox} = 10$ into the above equation. The width of the vacuum gap was set to approximately 8 Å by assuming negligible changes in the tip-sample distance in the scanning range of the bias from 1.0 to 3.0 V. While corrections are minor for the ultrathin MgO layer ($V_{ox}/V_{vac} = 0.05$), they become significant for the 25 ML thick CaO spacer ($V_{ox}/V_{vac} = 0.62$) for which more than one third of the total voltage drops in the oxide barrier (cf. Fig. 5.6b). After a renormalization of the dispersion, the band properties for the Au clusters on thick CaO films converge against the ones obtained for the ultrathin MgO layers (cf. Fig.

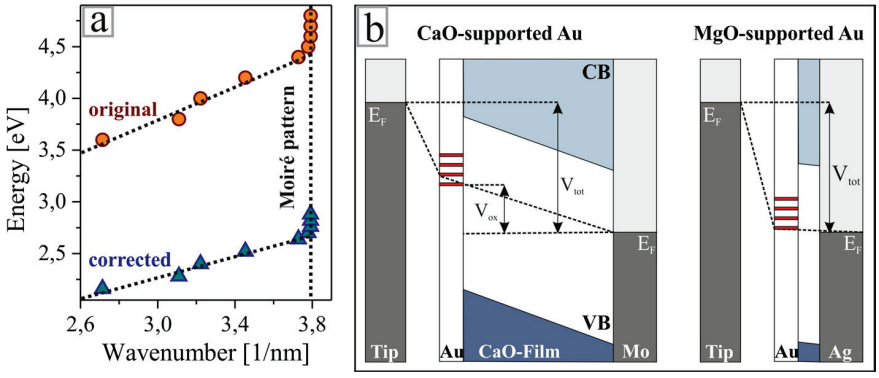

Fig. 5.6: (a) Experimental dispersion relation of QWS in the CaO-supported Au cluster shown in Fig. 5.5 (200 atoms). After the correction for tip-induced band bending, the eigenenergies shift downward and approach the values obtained for MgO-supported Au islands. Above a critical wavenumber of k=3.8 nm^{-1}, the wave pattern locks into the periodicity of the Moiré pattern and becomes constant. (b) Potential diagram of the STM junctions containing either a thick CaO or a thin MgO film. Band bending effects are relevant only for the highly polarizable CaO spacer layer.

5.6a). While the band onset shifts downwards to 0.7 V, the slope reduces to 0.55Vnm. Note that error bars in the CaO-based experiment are generally larger due to the lower quality of the measured standing wave patterns and the additional renormalization error based on the assumed constant tip-sample distance. In this regard, the experimental results obtained for Au clusters on both oxide films match in a reasonable manner, suggesting that one and the same gold band experiences electron confinement in both cases. The remaining deviations might be due to differences in the experimental situation. For instance, the magnitude of electron transfer may be larger for MgO since the Ag(001) single crystal underneath is a quasi-infinite electron reservoir, whereas the number of accessible Mo donors in the doped CaO is finite. On the other hand, the expanded CaO lattice with respect to MgO may increase the spacing between the Au atoms, which reduces the overlap of the Au orbitals and increases the effective electron mass of the corresponding band, and therefore lower the slope of the dispersion relation. Nonetheless, the general electronic properties of the ad-islands are very similar on both oxide supports.

The following paragraph discusses further experimental evidences for the charge promotion via the two different oxide layers into the Au ad-islands. In the case of ultrathin MgO/Ag(001) film, the electrons originate from a metal support, while for the 25 ML CaO/Mo(001) film the charging is based on electron exchange with single Mo ions inside the oxide matrix. If both charging routes converge to the same final state, the common use of ultrathin oxide films as model systems for heterogeneous catalysis and chemical sensing gets validated once again [223]. The obtained knowledge on the electronic structure of Au islands supported on thin and thick oxide films enables us to address this point with high accuracy. (i) The growth shape of the Au clusters gives a first indication for the presence of excess electrons. Au clusters on both oxides grow in a monolayer fashion and no 3D deposits are observed on either surface. The 2D growth regime of gold has safely been connected with a charge transfer into the ad-material and is explained with a stronger Coulomb and polaronic interaction of Au anions with respect to their neutral counterparts [18, 19, 158, 224]. Furthermore, it has been shwon that the 2D growth regime breaks down when the MgO thickness exceeds the tunneling length of electrons [18] or when the donor concentration in the CaO matrix becomes insufficiently low [21, 22, 225]. In both cases, electron transfer into the ad-islands becomes ineffective and forces the gold to return to its usual 3D growth. The clear prevalence of 2D growth on both oxide films thus provides evidence for a robust and sufficient charge transfer into the gold islands (cf. Figs. 5.1, 5.2). (ii) A second hint for an electron flow into the gold is deduced from the

upshift of field-emission resonances (FERs) on top of the metal nanostructures as compared to the bare oxide (Fig. 5.7). FERs are vacuum states that develop in the classical part of the tip-sample cavity and govern the electron transport in STM junctions at high biases [219]. The lowest FER marks the approximate position of the vacuum energy of the system, while higher levels are additionally influenced by the tip-electric field. On both oxide supports, the FERs continuously shift to higher energies when moving the tip from the bare oxide towards the Au islands (from 4.0 to 6.0 V for the first FER, Fig. 5.7). The upshift indicates a higher surface potential above the nanogold, reflecting the effect of electron accumulation inside the islands but also the higher workfunction of gold (5.2 eV) as compared to the oxide films (4.0 eV) [22]. (iii) A third and last evidence for charge accumulation in the ad-islands is the pronounced negative contrast around the island perimeter and surrounding oxide, especially at high bias (cf. Fig. 5.8). As it has been explained in chapter 3.2, the extra electrons mainly localize along the cluster perimeter. In this way, they maximize their mutual distance and minimize their electron-electron repulsion inside the nanostructures [193]. Moreover, additional states are localized in the low-coordinated edge atoms that can be easily populated

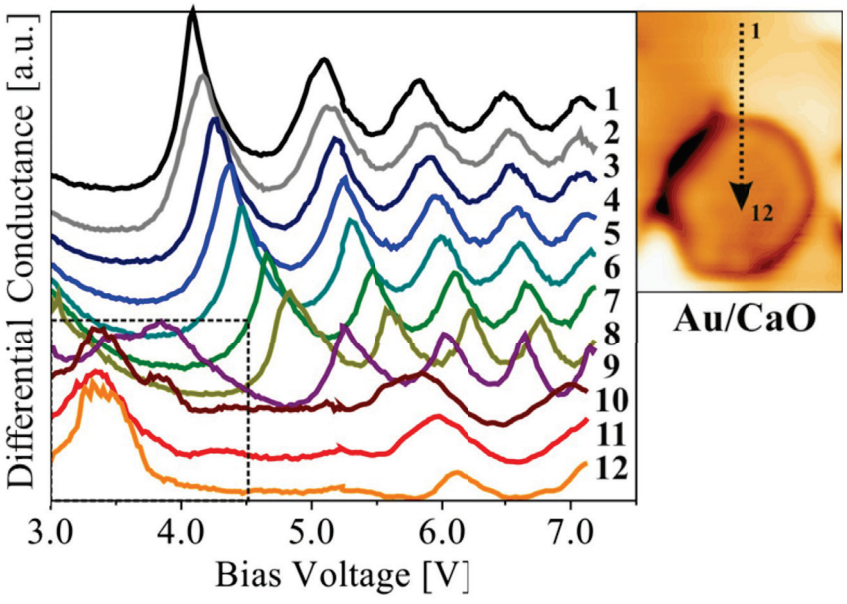

Fig. 5.7: Series of dI/dV spectra taken along a path from bare CaO onto an Au cluster as shown in the inset (11 x 25 nm^2). The high-bias dI/dV oscillations are FERs that shift up in energy when approaching the gold due to a repulsive effect induced by the excess electrons in the nanostructure. The spectral region marked by the dashed box covers the Au QWS before correction for band bending effects. [216]

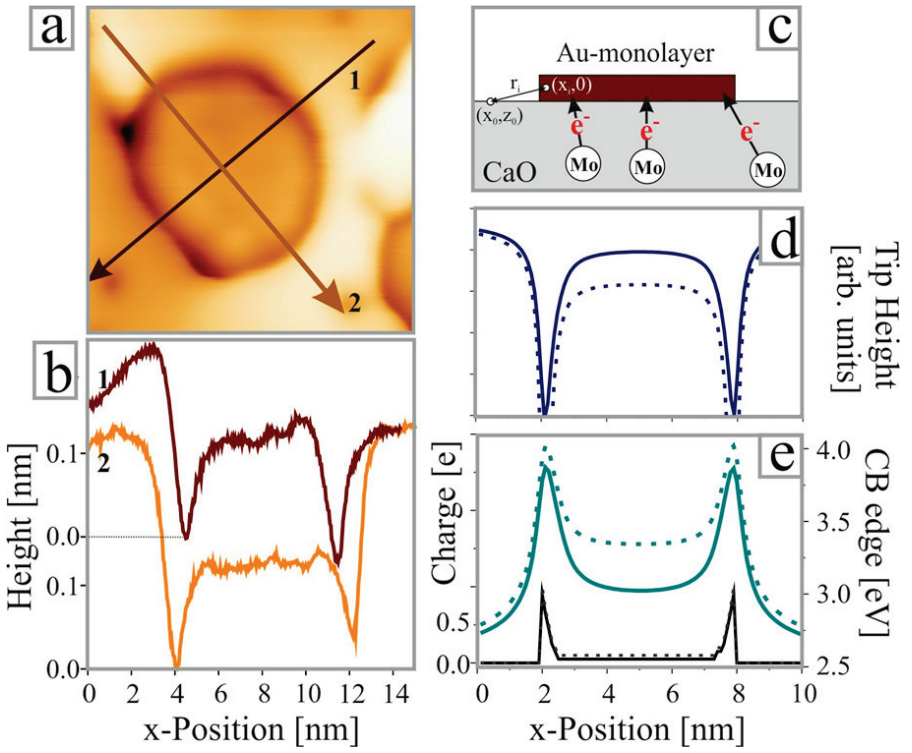

Fig. 5.8: (a) STM topographic image (12 x 12 nm^2) and (b) respective height profiles across an Au cluster. (c) Structure model of a negatively charged Au island grown on self-doped CaO/Mo(001). (d) STM tip-height calculated for the approximate charge distribution across the island as shown in (e) (black). The corresponding shift of the CaO conduction band is depicted above (blue). Solid and dashed curves are representative for a weakly and strongly charged island, respectively.

by the transferred electrons. The dark appearance of the electron-rich island perimeter now reflects a polarization effect of the oxide layer below the metal island, as it is demonstrated with the following simulation for the CaO-Au sytsem. A simple 1D model, in which edge atoms are negatively charged while inner ones are neutral, shall account for the charge distribution $q_i(x_i)$ in the island (Fig. 5.8e). Due to its poor screening ability, the electronic states of the oxide respond sensitively to the presence of extra electrons on the surface and experience an up-shift in energy [11]. The destabilizing impact of the excess electrons on the oxide bands can be modeled with a screened Coulomb interaction:

$$V(x_0) \propto \sum_i \frac{q_i}{\epsilon_0 \epsilon_{CaO} r_i} \tag{5.3}$$

Here, $r_0 = \sqrt{(x_0 - x_i)^2 + z_0}$ is the distance between the extra electron in the

gold and a position (x_0, z_0) in the oxide film. The computed up-shift of the oxide bands peaks directly below the electron-rich island edges, but further extends into the oxide film (cf. Fig. 5.8e). The impact of the band shift on the STM image contrast shall be modeled by treating the oxide conduction band as main final states for incoming electrons from the tip. This is a reasonable assumption at the elevated positive bias used in the experiment. The stabilizing current I_T in the STM is proportional to that part of the conduction band that spans from its onset valence conduction band (VCB) to the bias set point Vs inside the band:

$$I_T(V) \propto e^{-\kappa z} \rho_{tip} \int_{vcb}^{vs} \rho_{cao} dE \propto \rho_{tip} \rho_0 e(V_s - V_{cb}) e^{-\kappa z} \tag{5.4}$$

Here, ρ_{tip} is the state-density of the tip and κ the decay constant of wavefunctions in the vacuum that can be determined directly from experimental current-distance plots [47]. Solving the formula for z gives a qualitative expression for the tip-sample distance when scanning the negatively charged island (cf. Fig. 5.8d):

$$z = \frac{1}{\kappa} \ln \frac{I(V)}{\rho_{tip} \rho_0 e(V_s - V_{cb})} \tag{5.5}$$

When approaching the island, the tip-height gradually decreases, because negative excess charges on the gold shift the oxide bands to higher energies and therefore diminish the state-density that is in reach for the tunneling electrons [11]. Directly at the edge, the tip-sample distance runs through a minimum and returns to an intermediate value inside the island. The reverse sequence is revealed when the tip moves away from the metal sheet, crossing the electron-rich brim again. This simulated height profile qualitatively captures the experimental behavior, i.e. the gradual contrast reduction when approaching the island, the dark ring at the island perimeter and the plateau region in the island interior. The zone of negative contrast around the islands can thus be taken as direct evidence for a charge accumulation at the island perimeter. Evidently, the dark rings are more pronounced around gold islands on the CaO than the MgO films, reflecting the enhanced polarizability of the thicker oxide. A direct correlation between the spatial extension of the dark ring-zone and the number of excess electrons in the ad-islands can therefore only be obtained on films of equal thickness.

5.3 Conclusions

Both, a thin MgO film on Ag(001) and a thick CaO film on Mo(001) doped with Mo donor-ions were found to induce a considerable electron flow into Au nanostructures deposited on their surface. The charge transfer was unambiguously revealed from a number of experimental signatures. Gold deposition on the two oxide surfaces leads to the exclusive formation of monolayer Au islands, indicative for a reinforced metal-oxide adhesion in presence of the excess charges. In both cases, the Au electronic structure experiences lateral quantization effects, arising from electron confinement in one and the same Au 6*sp*-type band. In the MgO-case, the Au quasi-band arising from the in-plane quantization of the cluster's electronic states could be correlated to the LW band of bulk gold. Surprisingly, the electronic structure of the Au 2D material (monolayer islands) agrees already to a large extent to the one of Au 3D material (bulk) although the atoms in the third dimension are missing. Finally, a pronounced dark rim around the islands as well as a characteristic up-shift of vacuum states when approaching the island perimeter provide unique evidence for the accumulation of extra electrons in the low coordinated edge atoms delimiting the gold nanostructures. Within the accuracy of our measurements, we find identical properties of MgO and CaO-supported Au deposits, indicating that nature and magnitude of the substrate-mediated charge transfer are the same. Evidently, the two charging routes explored here, namely electron transfer from a bulk metal below an ultrathin oxide spacer and charge donation from impurity ions dispersed in a thick oxide matrix, give rise to a similar final state for gold ad-particles bound to the two oxide surfaces. On the basis of this correspondence we argue that ultrathin oxide films, as often used in surface science experiments, are well suited to model the situation in doped bulk oxides, being widely employed in real catalysis. This conclusion emphasizes the significance of fundamental, atom-scale experiments for elucidating general principles of the surface chemistry of supported metal catalysts.

Chapter 6

Changing Quantum Well States in Gold Clusters upon Molecular Adsorption

The following chapter describes for the first time the influence of molecules onto the local electronic structure of metal clusters. The model system consists of monolayer Au islands grown on MgO/Ag(001) ultrathin films that exhibit a quantized electronic structure, accessible to LT-STM imaging and spectroscopy. The alteration of the model systems after molecular adsorption has been investigated for two entities, isophorone ($C_9H_{14}O$) as weakly interacting organic molecule and CO_2 as a typical Lewis acid. The former one is a prototype oxygenate molecule which is not specifically known for a strong interaction with noble metals. Due to its relatively large size and good visibility in the STM, it serves as ideal sample molecule to monitor physisorption processes with the STM. In the second case, CO_2 as a molecule of general significance has been adsorbed on the sample surface. A nanocatalytic activation of CO_2 is of importance in chemistry because it would enable the conversion of a chemically worthless species into a precursor for further reactions, e.g. the production of hydrocarbons. The simultaneous reduction of the in abundance existing greenhouse gas is further of high environmental and political interest. The two species have a different impact on the intrinsic QWS structure of the metal nanoparticles which reflects differences in their binding behavior.

6.1 Precharacterization of the Surface

In a first step, isophorone has been deposited onto the pristine MgO/Ag(001) surface. The molecules were dosed at RT from a flask containing the liquid at 0.5 L (10^{-7} mbar for 5 s). After exposure, circular protrusions of about 8 Å diameter appeared on the clean MgO and have been correlated to isophorone. Three main observations have been realized: (i) Isophorone decorates the MgO-Ag edges (Fig. 6.1a); (ii) the first ML of MgO gets covered with molecules while the second ML remains pristine (Fig. 6.1a); and (iii) the molecules agglomerate into "magic arrangements" (Figs. 6.1b,c). Fig. 6.1d shows some of those sample agglomerations that can be observed on the surface and consist of double, triple, quadruple and hexamer clusters. Note that each configuration displays a number of isomer structures (cf. Fig. 6.1d). Contrarily, if isophorone covers the bare silver substrate it arranges in perfect hexagonal patterns (Fig. 6.1e).

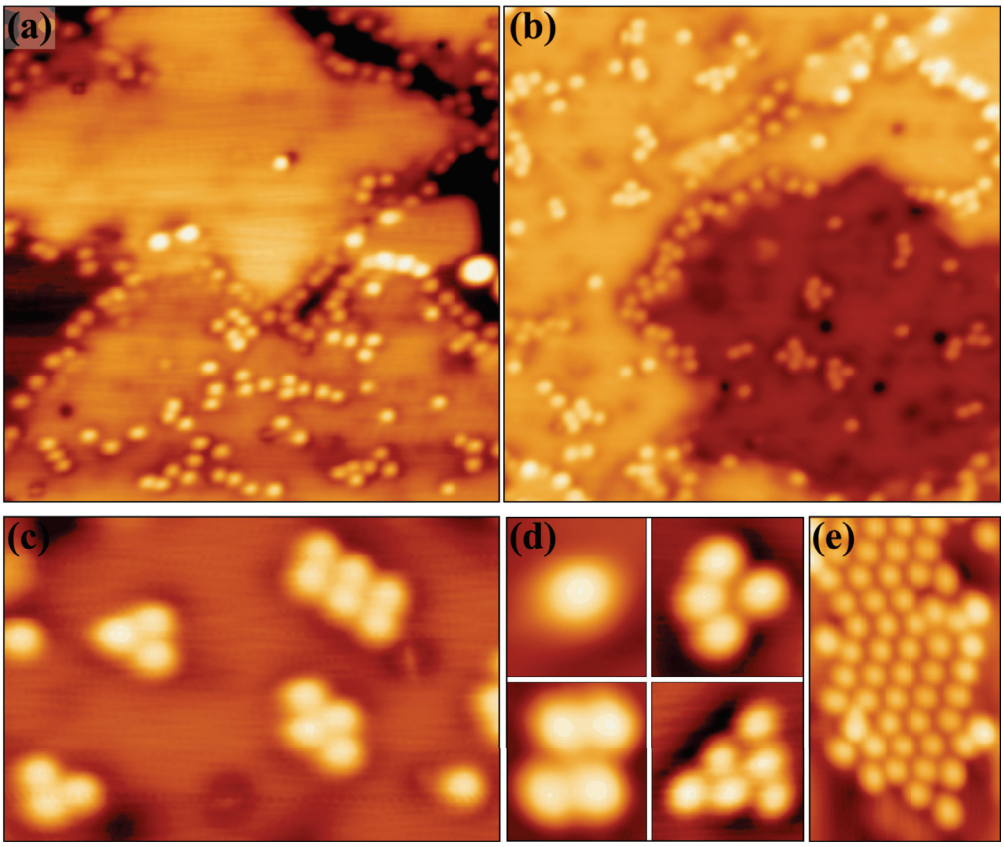

Fig. 6.1: Topographic images of (a-d) the MgO/Ag(001) ultrathin film and (e) bare Ag substrate after exposure to isophorone (a,b: 30 x 30 nm^2, c: (12 x 8 nm^2, d: 12 x 7 nm^2).

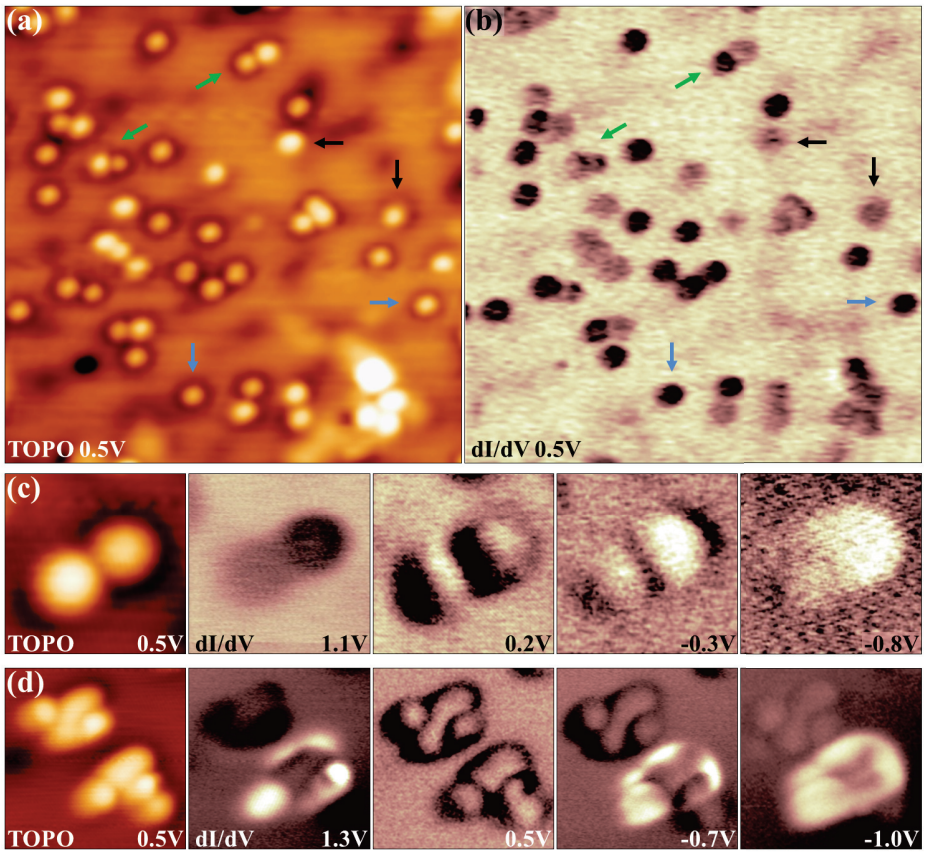

Fig. 6.2: (a) Topographic image and (b) corresponding dI/dV map of the MgO/Ag(001) ultrathin film after codeposition of Au atoms (blue arrows) and isophorone (black arrows) (18 x 18 nm^2, 50 pA). A partial formation of Au-isophorone pairs (green arrows) could be observed. Sequences of dI/dV maps at different biases of (c) single and (d) multiple Au-isophorone hybrid structures.

In a next preparation step, single Au atoms have been added to the sample surface at LT (15 K), leading to a coexistence of Au atoms and isophorone molecules. During scanning at higher bias both species appear as circular protrusions with approximately the same diameter of 6 to 8 Å and cannot be distinguished. However, when reducing the scanning bias to values between 0.5 and 0.8 V, one of the species becomes surrounded by a ringlike depression. Such a sombrero type depression has been observed before for Au atoms on 3 ML MgO/Ag(001) films [43] and on 2 ML NaCl/Cu(111) film[1] [226]. The effect is attributed to a negative charging of the atoms that are stabilized on

[1]Here, the charging of the neutral Au atoms was induced by a voltage pulse applied to the STM tip.

the surface by a strong polaronic distortion of the oxide substrate leading to the ringlike depression. The second species maintains its protrusive character and is hence related to isophorone. Beside this fact, both species are clearly distinguishable in dI/dV maps taken at 0.5 V. The Au atoms show a dark contrast whereas the isophorone shows a weak, almost negligible contrast in comparison to the oxide.

Furthermore, hybrid structures consisting of Au and isophorone could be detected. For instance Fig. 6.2c shows a single hybrid structure composed of one Au atom (upper protrusion with dark ring) and a single molecule (lower protrusion). By taking conductance maps in the range of 1 V around the Fermi energy, different behaviors of both ad-species become visible. The species associated with the Au is characterized by a fairly dark contrast at 1.1 V whereas the molecule shows a weak contrast. At -0.8 V, the upper species turns bright while the lower one keeps its weak contrast. The two dI/dV maps taken close to the Fermi energy at 0.2V and -0.3 V are characterized by a sequence of dark and bright stripes cutting perpendicular through the pair structure. This gives a strong indication for the formation of a chemical bond between both entities. In addition, multiple hybrid structures have been observed (Fig. 6.2d) consisting of roughly three Au atoms in their center and two (upper complex) and three molecules (lower complex) attached to their surface. Also here, a distinct electronic behavior is discernible in the sequence of dI/dV maps.

6.2 Isophorone-Adsorbed on Gold Clusters

In a next preparation, MgO films with Au clusters have been prepared at 300 K and were subsequently dosed with isophorone. Fig. 6.3 shows topographic and dI/dV images of a surface with Au clusters after isophorone exposure. The scans were taken at 1.7 V, as the high conductivity associated to the pronounced metal-oxide interface state at this energy clearly distinguishes MgO mono- and bi-layers from uncovered Ag and thick oxide patches. Hexagonal Au clusters of 15-35 nm^2 average sizes are found on top of the wide oxide terraces. They are readily identified due to their bright contrast in the topographic channel and a pronounced quantization pattern in the corresponding dI/dV maps [61]. After isophorone exposure, circular protrusions of 8 Å diameter appeared on the Au islands. Remarkably, the gold-bound molecules were found exclusively along the island perimeter and no features have been detected in the interior. Along the island edges, the molecules have a regular

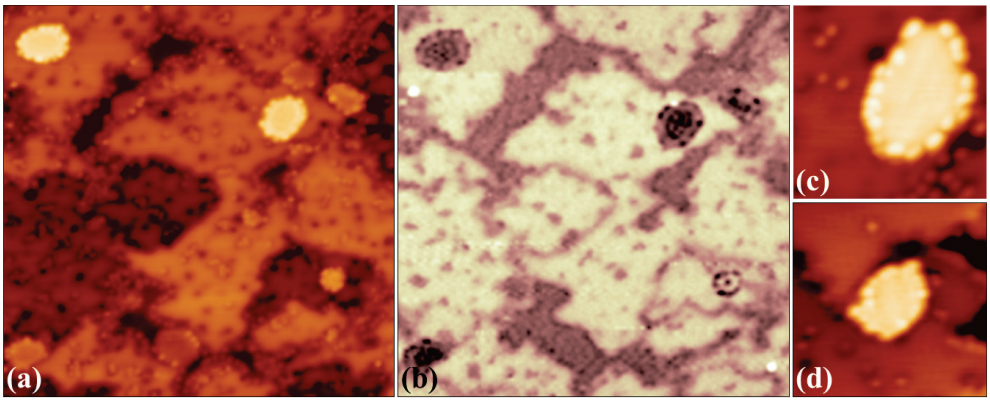

Fig. 6.3: (a) Topographic image and (b) corresponding dI/dV map of the MgO/Ag(001) ultrathin film after isophorone exposure (60 x 60 nm^2, 1.7 V, 50 pA). The quantization pattern of the monolayer islands is clearly discernible in (b). Topographic images of (c) isophorone and (d) CO_2 molecules bound to Au clusters and the MgO surface (15 x 15 nm^2, 0.3 V, 50 pA).

spacing of about 8 Å, a value that matches the diameter of isophorone. Each Au nanostructure therefore provides room for 10-15 edge-bound molecules (Fig. 6.3c).

Fig. 6.4a shows a sample cluster adsorbed with isophorone. The influence of molecular adsorption on the cluster's electronic structure is revealed by comparing dI/dV data-sets taken on one and the same Au island with molecular species and after desorbing them. The successful removal of the 15 molecules becomes evident in the topographic image in Fig. 6.4c, whereby a few undefined residuals always remained on the surface. Pronounced modifications after molecular desorption were detected in the electronic channel as well. Fig. 6.4b shows dI/dV spectra taken at two points within the isophorone-adsorbed cluster exhibiting pronounced conductance peaks. By a deconvolution of the spectra into Gaussians (not shown here) in analogy to chapter 4, five QWS could be extracted. The states are localized at 0.7, 0.8, 1.1, 1.4 and 1.6 V and were assigned to eigenstates of the Au $6p_z$ manifold. The symmetry of the quantization patterns was revealed from dI/dV maps (Fig. 6.4a). They display a series of bright and dark ellipses that appear in the island center and propagate outwards with increasing energy. While the lowest QWS at 0.7 V exhibits a uniform dI/dV intensity throughout the entire cluster, higher states are characterized by alternating dark and bright contrast in the center region and the development of up to three protruding rings when moving towards the rim. The intensity pattern of the second state shows a minimum in the center while the outer regions of the cluster remain bright. The third dI/dV map

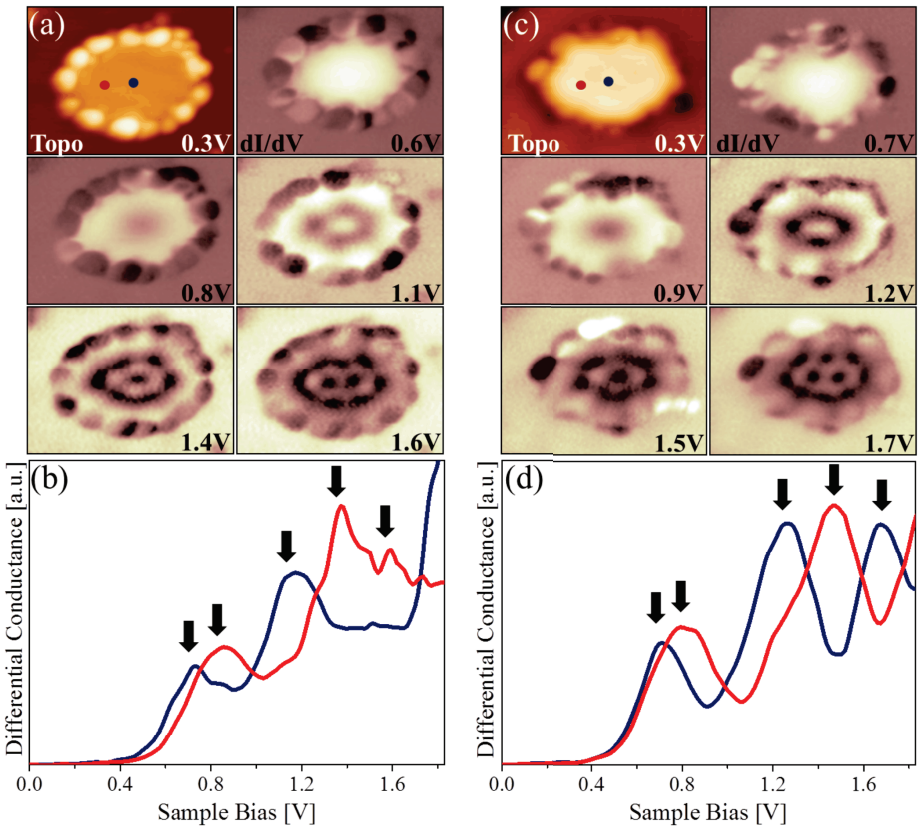

Fig. 6.4: Topographic and dI/dV maps of an Au island (a) with and (c) without isophorone molecules bound to its perimeter (11 x 8 nm^2, 70 pA). (b) and (d) associated STS spectra taken in the center (blue) and the left part (red) of the island as indicated in (a) and (c). Gaussian fitting revealed five QWS that are marked by arrows. Their bias positions match the ones used for dI/dV imaging in (a) and (c).

reveals bright inner and outer regions that are separated by a dark ring. The fourth and fifth state display one and two dark spots in the cluster center, respectively, followed by a sequence of bright-dark-bright rings towards the outside. The intensity patterns match the eigenstates of a hexagonal potential well, as it has been described in chapter 5 and ref. [201, 202]. Moreover, their bias evolution is in line with the energy of the QWS derived in the spectroscopic regime. In a second step, the molecular species have been desorbed one by one from the cluster via bias pulses applied to the STM tip. The removal of the molecules was reproducibly performed at around 4.5 V without substantial changes of the island perimeter. This procedure is rather difficult since the STM tip needs to be in stable conditions during the long period of measurements. The overall electronic behavior of the Au island, as the number and symmetry of the QWS, remains unchanged. However, a closer look

into the dI/dV data reveals a characteristic energy shift of the eigenstates. The overall trend is discernible best in the conductance maps in Fig. 6.4c. For example, the second intensity pattern, characterized by a central maximum and a single dark ring, appears at 1.1V in the presence of edge-bound isophorone, but moves to 1.2V after desorption of the molecules. Similarly, the fifth QWS, displaying two central minima, experiences an upshift from 1.6 to 1.7 V after removal of the molecules.

To analyze the adsorbate-induced electronic perturbation and quantify the respective energy shift, the QWS structure was rationalized by a PIB model for a hexagonal potential well with infinite high walls, referring to chapter 5.2. The model is obtained by cutting the hexagonal Au potential well along a characteristic line that runs through the cluster (Fig. 6.5) and describes the quantization of electronic states depending on one quantum number n. The resulting dI/dV curves can then be interpreted as standing wave patterns that result from an energy overlap of neighboring states with finite width (cf. Fig. 6.5). The obtained conductance graphs reflect amplitude modulations of the squared wave functions in the quantum well and are most pronounced when the bias voltage matches the energy of an eigenstate. Following the procedure in ref. [197], the exact bias positions of the QWSs were determined by a fit of the experimental dI/dV line plots as a function of sample bias by (with $k_n = n \cdot k = n \cdot \frac{\pi}{L}$):

$$\frac{dI}{dV}(x,V) = c_1(V)\cos^2(kx) + c_2(V)\sin^2(2kx) + \\ +c_3(V)\cos^2(3kx) + c_4(V)\sin^2(4kx) + \ldots \tag{6.1}$$

Each summand consists of a squared cosine or sine and represents one QWS depending on whether intensity maxima or minima are localized in the cluster center, respectively. The bias-dependent coefficients $c_n(V)$ account for the spectral weight of the different wave functions in the experimental spectrum [227]. The bias evolution of the coefficients $c_n(V)$ for the sample cluster with and without isophorone is shown in Fig. 6.5. It follows a Gaussian behavior

Tab. 6.1: Bias-dependent coefficients $c_n(V)$ of the squared wave function and the energy shift $\Delta U = U_{cl+mol} - U_{cl}$ for one Au cluster with and without isophorone.

	Left side of cluster					Right side of cluster				
	c_1	c_2	c_3	c_4	c_5	c_1	c_2	c_3	c_4	c_5
U_{cl+mol} [V]	0.63	0.81	1.12	1.42	1.64	0.61	0.78	1.08	1.46	1.61
U_{cl} [V]	0.53	0.84	1.1	1.54	1.79	0.53	0.84	1.19	1.51	1.74
ΔU [V]	+0.10	-0.03	-0.07	-0.12	-0.15	+0.08	-0.06	-0.11	-0.15	-0.13

with the maximum value giving the center position of the corresponding energy state E_n. The respective values, analyzed spearately for the left and right side of the cluster, are summarized in Tab. 6.1. Furthermore, the energy shift of states with the same quantum number n, $\Delta U = U_{cl+mol} - U_{cl}$, is calculated. Both sides of the cluster agree nicely with each other and therefore only the left side of the cluster is considered in the further analysis.

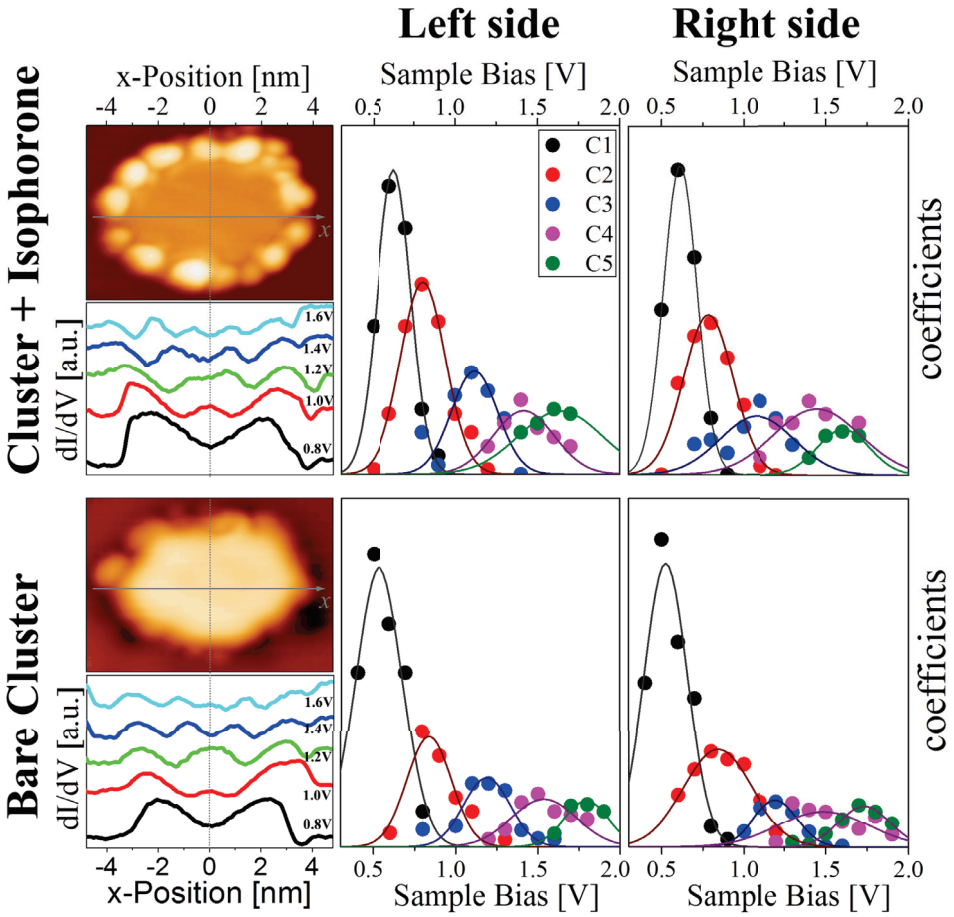

Fig. 6.5: Evolution of the bias-dependent coefficients $c_n(V)$ of the squared wave functions as obtained by fitting dI/dV plots at different bias (lower left diagram). These are analyzed separately for the left and right side of the cluster.

The E-n dispersion for the cluster's electronic system with and without isophorone is plotted in Fig. 6.6a. Moreover, the energy shift of the QWS, $\Delta E = e \cdot \Delta U = E_{cl+mol} - E_{cl}$, is visualized depending on the quantum number n (Fig. 6.6b). While the first QWS slightly lowers its energy position, the following ones shift upwards. The energy difference follows a nearly linear relationship as function of the quantum number n, according to:

$E_n = E_{n,bare} - 0.07n$. Although details of the energy shift vary slightly from cluster to cluster, the general perturbation of QWS upon molecular adsorption has been reproduced in several cases. From equation 5.1 results the general dependence of the eigenenergies for hexagonal potentials with infinite walls:

$$E_n \propto \frac{1}{\Omega^* m_{eff}} \tag{6.2}$$

The linear E-n dispersion expected for hexagonal wells is undoubtfully reproduced in the present data. Evidently, the molecular interaction affects the slope of the dispersion curve, hence either the effective electron mass or the size of the confining potential. In a qualitative picture, the observed electronic trends can thus be traced back to the impact of gold-adsorbate interaction onto these key quantization parameters as discussed in section 6.4.

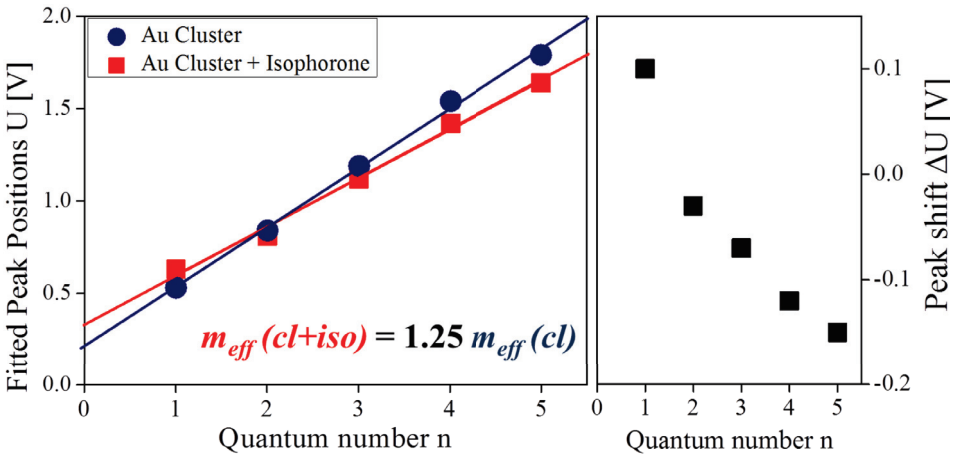

Fig. 6.6: Dispersion relation (left) and peak shift $\Delta U = U_{cl+iso} - U_{cl}$ (right) of QWS in an Au island with and without isophorone.

6.3 Carbon Dioxide-Adsorbed Gold Clusters

A similar picture as for isophorone-covered clusters emerged after dosing CO_2 onto the Au/MgO surface by filling the chamber with a back pressure of $1 \cdot 10^{-7}$ mbar for 50 s (5 L) at 250 K sample temperature (6.3d). Also here, molecular adsorbates were exclusively observed along the cluster rim, while no indication for adsorption was revealed in the interior. In contrast to isophorone, much less CO_2 was observed on the bare MgO surface, indicating a weaker adhesion to the oxide (or a fainter topographic signature of the molecule in

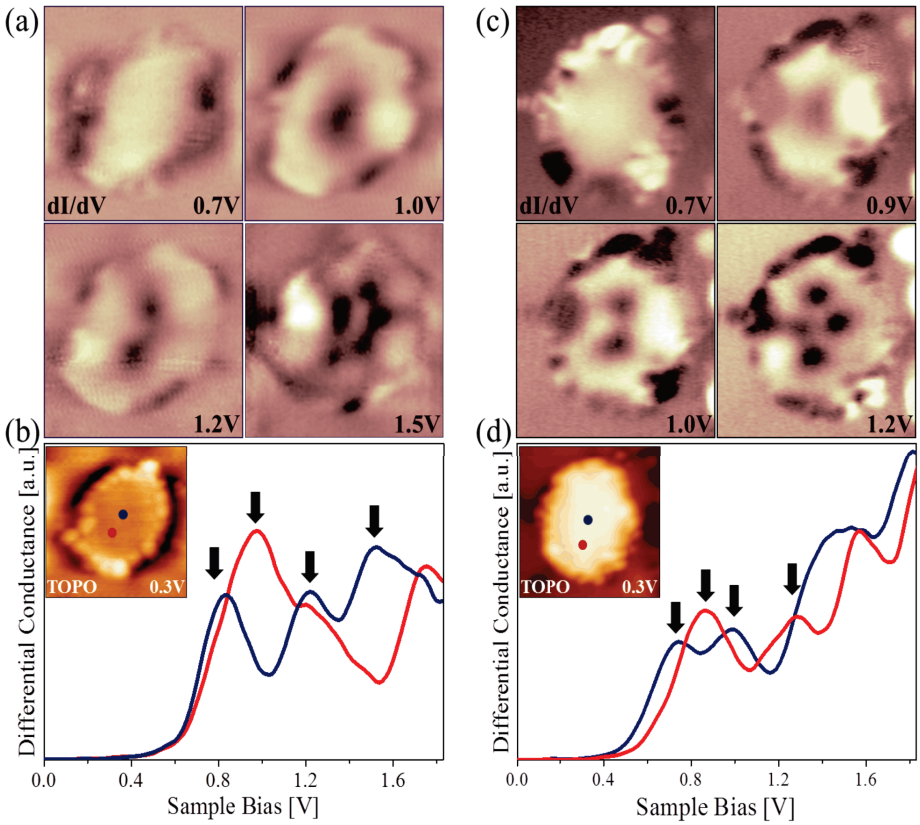

Fig. 6.7: Topographic (insets in b and c) and dI/dV images of Au islands (a) with and (c) without CO_2 molecules bound to their perimeter (8 x 8 nm^2, 70 pA). (b) and (d) respective STS spectra taken in the center (blue) and lower part (red) of the island. Gaussian fitting revealed four characteristic QWS that are marked by arrows. The identified bias positions match the ones used for dI/dV imaging in (a) and (c).

STM). The 15 CO_2 species at the Au-MgO boundary show a regular spacing, however with a reduced periodicity of about 5 Å as compared to isophorone which is in agreement with the smaller size of CO_2 molecules (cf. Fig. 6.7a). Whereas removal of isophorone was rather easily performed at 4.5 V without substantial changes of the island perimeter, a reliable tip-induced CO_2 desorption was impossible even at high bias conditions. The manipulation experiments sometimes even drastically changed the character of the island boundary. Consequently, we have referenced the dI/dV data of CO_2-covered islands to spectra taken on bare Au clusters of similar size and shape measured before the dosage of molecules. This approach is justified, as the interrelation between geometry and electronic properties of 2D Au quantum systems has been analyzed in detail in chapter 4.

Fig. 6.7b shows two dI/dV spectra taken at a CO_2 covered island. By

a deconvolution of the spectra into Guassians (not shown here), four QWS could be extracted. The QWS are localized at 0.75, 0.9, 1.2 and 1.5 V and are assigned to eigenstates of the Au $6p_z$ manifold. In spite of the lower dI/dV data quality as compared to isophorone, the symmetry of states has been recognized again from conductance maps shown in Fig. 6.7a. The lowest QWS at 0.75 V is characterized by a uniform dI/dV intensity throughout the entire cluster. The second and third state show one and two minima in the cluster center, respectively, whereas the outer region of the cluster maintain its bright contrast. The highest state exhibits an intensity maximum in the center, enclosed by a dark and bright ring. Due to the impossibility of desorbing the CO_2 molecules from the island rim, a pristine cluster of similar size and shape was chosen in order to compare the electronic structure in both nanostructures. As shown in chapter 4 and ref. [61], the electronic structure of Au clusters depends sensitively on the cluster size and shape. Therefore, the bare cluster needs to have a comparable size but also a similar shape as the CO_2-decorated island (cf. Fig. 6.8). For comparison, the cluster dimensions in the CO_2-case were determined to be 5.6x4.2nm^2, yielding a linear eccentricity of e=1.85 (cf. equation 4.4). The pristine cluster is estimated to be 5.8x4.4nm^2 in size, resulting in an eccentricity of e=1.89. A comparison of both values in the Δ-e diagram in Fig. 4.7c gives a negligible deviation of the HOMO-LUMO gap and hence of the electronic structure. However, the energy stretch of the four eigenstates of the cluster is about 0.3 V larger in presence of CO_2 than without molecules. dI/dV maps of the bare cluster reveal the same sequence and symmetry of QWS. For example, the second an third state, exhibiting one and two dark spots in their center, can be found in the pristine cluster as well but are shifted downwards about 0.1 and 0.2 V, respectively, compared to the CO_2-case. The highest state, displaying a dark ring around bright center and outer regions, shift from 1.5 to 1.2 V in the pristine case. To quantify the exact change in the electronic structure upon CO_2 adsorption, the QWS structure was rationalized again by a PIB model for ideal hexagons. In the same manner as in the previous section, the experimental dI/dV line runs along the clusters' center axes (cf. Fig. 6.8a) and was fitted as function of sample bias by equation 6.2. The extracted bias-dependent coefficients $c_n(V)$ shown in Fig. 6.8b provided the center position of the QWS and hence the E-n dispersion for both cluster as well as the energy shift ΔE depending on the quantum number (cf. Fig. 6.8c). While the first state maintains its energy position upon CO_2 adsorption, the higher states shift upwards, in contrast to the isophorone case. The energy difference follows a nearly linear relationship as function of the quantum number n, according to: $E_n = E_{n,bare} + 0.1n$.

Apparently, the CO_2 perturbs the Au quantum system in a different manner than isophorone, which provides unique insight into the nature of the gold-molecule interaction.

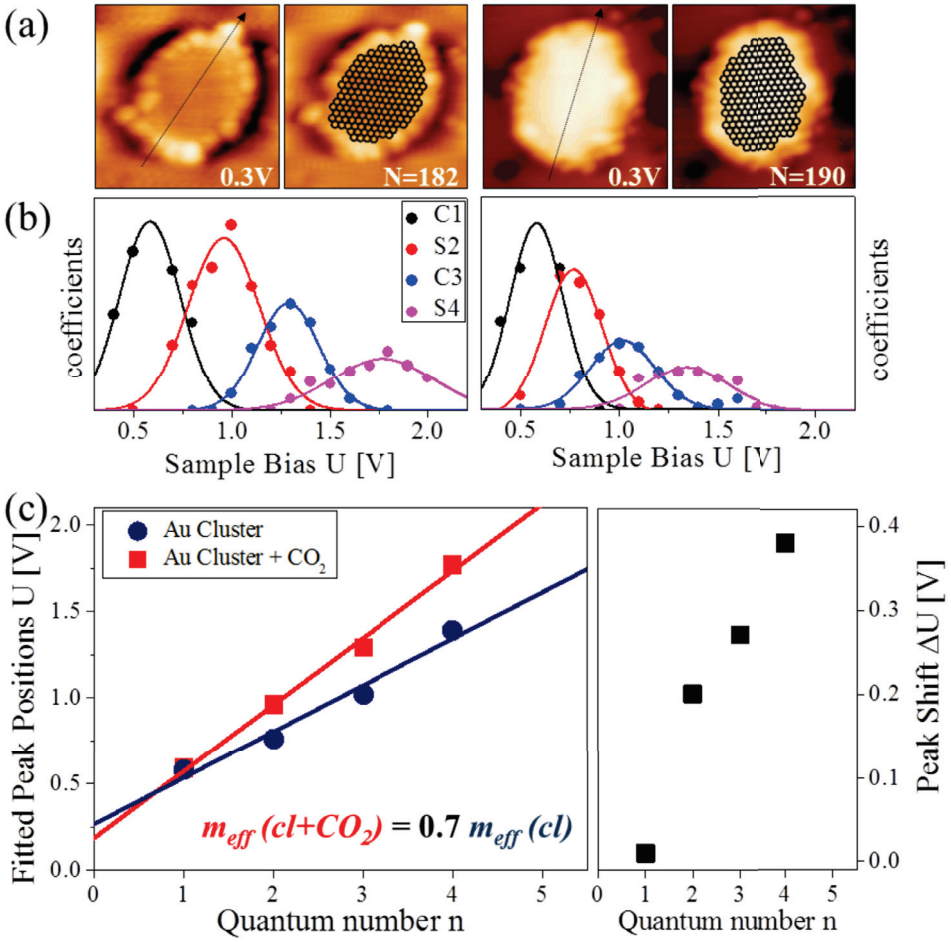

Fig. 6.8: (a) Topographic images and structure models of Au clusters with (left) and without (right) CO_2, showing the equality in shape and size the nanoislands. (b) shows the bias evolution of the coefficients $c_n(V)$ of the squared wave functions as obtained by fitting dI/dV line plots along the lines shown in (a). (c) Dispersion relations (left) and peak shift $\Delta U = U_{cl+CO2} - U_{cl}$ (right) of QWS in both islands.

6.4 Binding Behavior of the Molecules: Chemisorption versus Physisoprtion

A weak point of the STM is its missing possibility to acquire chemical information of ad-species on surfaces. In order to get a chemical fingerprint of the

molecular adsorbates on Au clusters, IRAS measurements on clean and Au nanoparticle-covered MgO/Ag(001) ultrathin films adsorbed with CO_2 and isophorone have been performed in a subgroup of the FHI's Chemical Physics department by Dr. Florencia Calaza. Thereby, the preparation procedure of the Au/MgO system has been transfered to another chamber, equipped amongst others with an IRAS spectrometer, a TPD and mass spectrometer. The film characteristics and quality have been checked by XPS and LEED. The MgO film was estimated to be 2 ML thick with 0.06 ML nominal coverage of Au cluster, being in excellent agreement to the films prepared inside the STM chamber. Subsequent DFT calculations performed in the research group of Prof. Hannu Häkkinen from the University of Jyväskylä give additional insights into the binding configurations of the molecular species to the Au nano-islands.

6.4.1 Chemisorption of Carbon Dioxide

IRAS experiments on isotope-labeled CO_2 and MgO on clean and gold-covered MgO/Ag(001) ultrathin films prove the electron transfer from Au clusters into CO_2 molecules. The top spectrum in Fig. 6.9a shows a clean MgO film exposed to CO_2 at 220 K, close to saturation coverage. The intensity of the sole band at 1295 cm^{-1} corresponds to a molecule coverage of 0.02 ML as determined by calibration measurements on CO/Pd(111) and coverage-dependent LEED data [228]. This coverage corresponds roughly to the density of color (F^+) centers on the MgO surface which are located specifically at MgO edge sites as it was independently determined by STS measurements in the past [110]. The observed frequency would be compatible with both, carbonate (CO_2 adsorbed on top of lattice oxygen) and carboxylate (CO_2 on top of oxygen vacancies or metal ions) [229]. By measuring IR spectra of ^{18}O-labeled MgO films, the formation of carbonates is ruled out as no shift of the 1295 cm^{-1} band is observed (cf. Fig. 6.9a). Molecular adsorbates which bind to heavier oxygen in the oxide film would lower the frequency band. If, on the other hand, CO_2 is either ^{18}O or ^{13}C labeled, the frequency of the carboxylate shifts to 1259 cm^{-1} and to 1275 cm^{-1}, respectively, consistent with an increased molecule mass (Fig. 6.9a). The observed frequency shifts and the possible adsorption site on top of F^+ center is in line with calculations for the CO_2 adsorption on bulk MgO(100) surfaces [230–232]. Note that the reported results on bulk MgO(001) may not be directly applicable to thin films due to the missing metal support, but a full study of CO_2 on thin MgO/Ag(001) is missing so far.

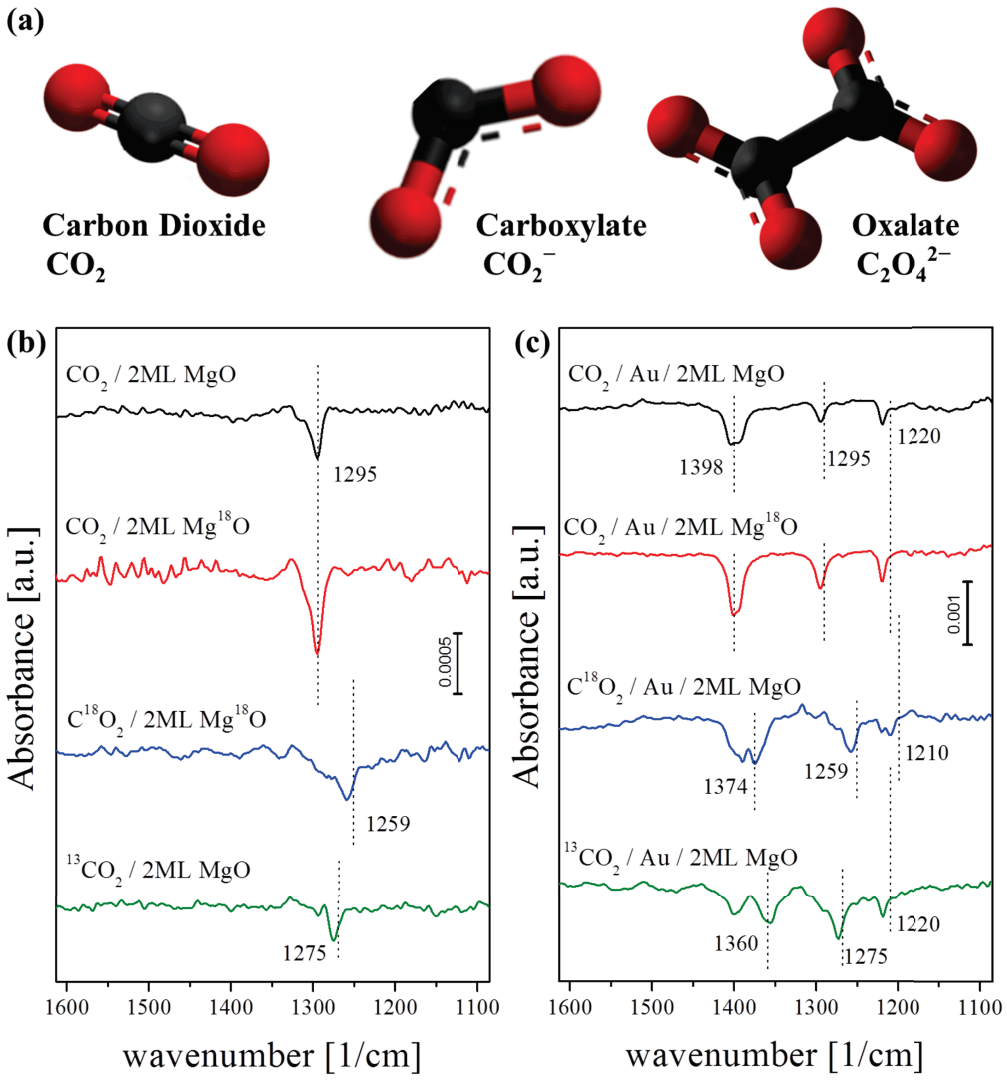

Fig. 6.9: (a) Structure of neutral CO_2 (left); carboxylate (center), and oxalate (right), i.e. two carboxylate molecules together. Note the molecular bending in the carboxylate as a result of its negative charging. IR spectrum for CO_2 adsorption onto (b) a pristine and (c) with Au clusters covered 2 ML MgO/Ag(001) films with saturation dose at 220 K.

Tab. 6.2: Adsorption energies and charge transfer for CO_2 adsorption on the Au/MgO system as calculated by DFT. Taken from ref. [234].

	$AuCO_2$ planar	$AuCO_2$ normal	Au_2CO_2 planar	Au_2CO_2 normal	$Au_2C_2O_4$ planar	$Au_2C_2O_4$ normal
E_{ads} [eV]	-0.58	-0.39	-1.24	-0.75	-0.95	-0.72
q_{Au} [|e|]	-0.73	-0.89	-1.04	-0.78	-1.59	-1.55

In a next step, CO_2 is dosed onto MgO-supported Au clusters. Thereby, two new vibrational modes, centered at 1220 cm^{-1} and 1398 cm^{-1}, are observed with respect to the bare oxide film and are assigned to oxalate (Fig. 6.9b). The unchanged carboxylate band at 1295 cm^{-1} serves as a calibration standard in the following. A certain degree of heterogeneity is inherent in those bands, as a result of the irregular rim shape of the Au clusters. The amount of adsorbed molecules, as calculated from the Au covered regions on the MgO surface with assumed cluster diameters of 4-5 nm, agrees well with the observed intensities assuming 15 molecules per cluster. The basis for assignment of the molecules to oxalate species results from a comparison with known oxalate - transition metal complexes [233], which exhibit two bands with appropriate vibrational frequencies. Further evidence comes again from isotope experiments shown in Fig. 6.9b. (i) By labeling the oxide film to $Mg^{18}O$, no band shifts are observed and thus ruling out the possibility that oxygen atoms around the cluster perimeter are responsible for anchoring of the CO_2. (ii) For $C^{18}O_2$ labeling, the calibration band (1259 cm^{-1}) remains unchanged compared to the bare MgO film, while the two oxalate bands shift to lower frequencies, i.e. 1374 cm^{-1} and 1210 cm^{-1}, respectively, consistent with a higher molecule mass. (iii) Upon $^{13}CO_2$ labeling the carboxylate standard shifts as expected to 1275 cm^{-1}, while the lower band at 1220 cm^{-1} remains unchanged, and the upper one moves to 1360 cm^{-1}. For the two oxalate modes, a normal mode analysis, performed for a planar oxalate arrangement, is available in literature [233] including calculations for the in-plane vibrational frequencies. Those calculations reveal a predominantly C-O stretch and O-C-O angle deformation character for the lower band at 1220 cm^{-1}, while the high frequency band at 1398 cm^{-1} exhibits predominant C-C stretches mixed with some contributions of C-O stretches. The observed isotopic shifts are fully consistent with the qualitative assignments and strongly support the assignment of the two peaks to oxalate species formed at the cluster perimeter.

Subsequent DFT calculations reveal the binding configurations for CO_2 and C_2O_4 species on the Au/MgO surface and corroborate the experimental results. Starting with a single Au atom on the surface, two configurations for

$AuCO_2$ complex have been identified while no stable gold-oxalate complexes could be found in the calculations. (i) The surface-planar configuration (Fig. 6.10a) is accompanied by an electron transfers of 0.7|e| from Au to CO_2, resulting in an adsorption energy of -0.58eV. (ii) In the surface-normal configuration (Fig. 6.10b), the charge transfer is slightly larger (0.9|e|) but the adsorption is reduces (-0.39eV). Similar configurations have been found for CO_2 adsorption onto Au_2 dimers (not shown) but with a clear increase of charge transfer and binding energy, suggesting an even stronger binding of CO_2 to lager clusters (see Tab. 6.2). In a next step C_2O_4 species have been investigated. Two gas-phase configurations, cross and planar, were found with C-C bond lengths of 1.61 and 1.70 Å, respectively (Fig. 6.10c,d). The species were converged to a stable minimum with a total charge of -1.8|e|, approximating closely the full double anion. The oxalate can only be stabilized in a chemical bond in the DFT calculations when using at least an Au dimer as binding partner on the surface. Again two configurations were found with adsorption energies of -0.95eV for the "C-C surface-planar"configuration (Fig. 6.10e,f) and -0.7 eV for the "C-C surface-normal"one (Fig. 6.10g,h). The adsorption process

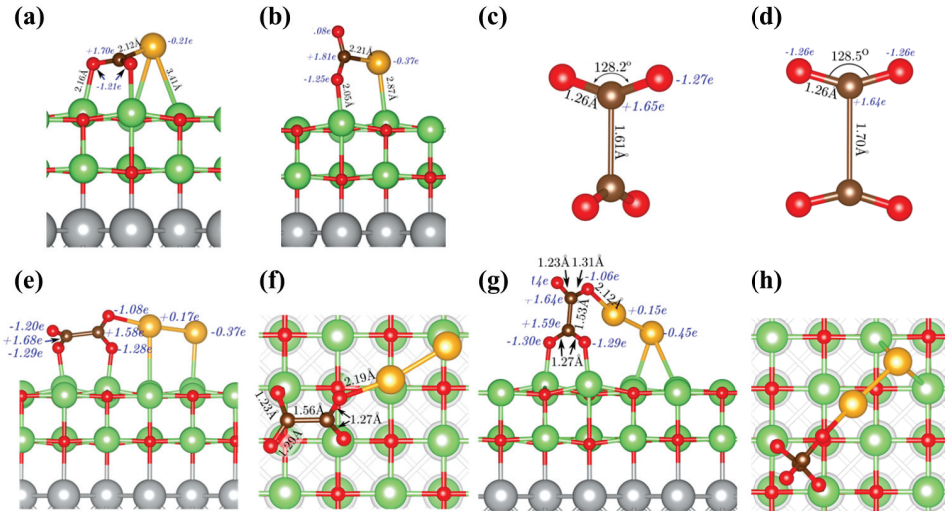

Fig. 6.10: DFT calculations of CO_2^- and $C_2O_4^{2-}$ species on a MgO/Ag(001) bilayer film [234]. Two configurations for $AuCO_2$ complexes are found in (a) surface-planar and (b) surface-normal orientations. In the gas phase, oxalate exhibits two stable configurations, (c) "cross" and (d) planar. (e,g) Side and (f,h) top views of $Au_2C_2O_4$ complexes consisting of "cross" oxalate (shown in (c)) and having their C-C bonds oriented (e,f) planar and (g,h) normal to the surface. (Colors: Mg: green, O: red, C: brown, Au: yellow, Ag: gray) The blue italics denote atomic Bader charges (in |e|) and black roman numerals interatomic bond lengths (in Å) and bond angles. The gas-phase structures in (c) and (d) were converged for the total charge of -1.8|e|.

is accompanied by a reduction of the C-C bond length to 1.56 and 1.53 Å, respectively, and a positive charging of the neighboring Au atom leading to a molecule charge of -1.59|e| and -1.55|e|, respectively (Fig. 6.10e,g). The calculations suggest the formation of oxalate as a result of an activation process, since the formation of the stable gold-oxalate complexes seem to depend sensitively on the reaction coordinate. Further vibrational analysis performed at $Au_2C_2O_4$ complexes show a good agreement between calculated (1228 cm^{-1}, 1414 cm^{-1}) and experimental values (1220 cm^{-1}, 1398 cm^{-1}) for the "C-C surface normal"configuration. This irreversible scenario can be excluded since no CO or O desorption has been detected during TPD measurements.

By TPD experiments, only CO_2 was identified as desorbing species exhibiting two desorption states. Carboxylate desorbs around RT (280 K) while oxalate desorption was measured at 320 K (Fig. 6.11), revealing an entirely reversible process:[2]

$$C_2O_4^{2-} \rightarrow 2CO_2 + 2e$$

One reason for the reversibility of the C_2O_4-CO_2 adsorption-desorption process is the low oxo-philicity of Au, which hampers the formation of adsorbed carbonate and hence an alternative reaction route. The experimental and computational results strongly suggest the following scenario taken place at the Au clusters supported on MgO/Ag(001) ultrathin films: The oxide film shuttles electrons from the metal support into flat, raft-like Au nanoislands with the transferred electrons located at the rim of the cluster: CO_2 adsorbs at the cluster rim, transforms into carboxylate by electron transfer, and reacts further with another CO_2 molecule to form oxalate. The formed oxalate desorbs from the surface as CO_2 and the electrons are shuttled back to the Au islands. The reaction is fully reversible.

$$\begin{aligned}
CO_2 + e &\rightarrow CO_2^-/Au_n \\
CO_2^-/Au_n + CO_2 &\rightarrow (CO_2)_2^-/Au_n \\
(CO_2)_2^-/Au_n + e &\rightarrow C_2O_4^{2-}/Au_n \\
C_2O_4^{2-}/Au_n &\rightarrow 2CO_2 + 2e
\end{aligned}$$

With the help of the experimental IRAS data and supporting DFT calculations discussed above, the binding mechanism of CO_2 molecules to Au clusters on MgO/Ag(001) ultrathin films has been clearly identified. Electron

[2]The desorption process is by no means self-evident, as in former studies an alternative oxalate decomposition has been proposed into carbonate, carbon monoxide and further oxygen [235–237].

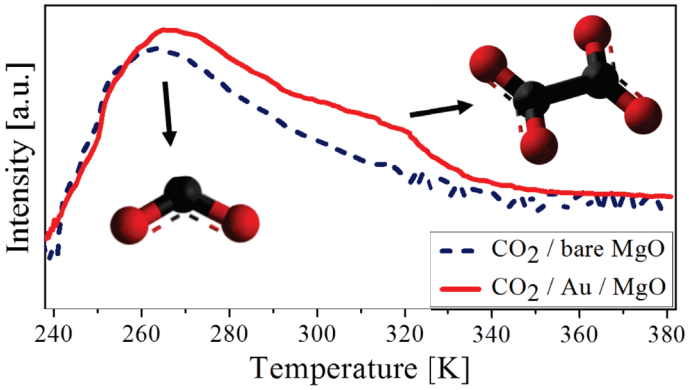

Fig. 6.11: TPD spectra (44 amu) for CO_2 desorption from the same pristine and with Au clusters-covered bilayer MgO/Ag(001) film. While CO_2 originating from carboxylate species desorbs around RT, CO_2 arising from oxalate desorbs at approximately 320 K.

transfer from perimeter Au atoms into CO_2 molecules explains the observed reorganization of the Au QWS. The excess charges in the negatively charged CO_2 ligands exert repulsive forces on the remaining electrons in the island that, in turn, adopt a positive net charge upon electron transfer. Thus the electron cloud in the gold island contracts and consequently the quantization area decreases (Fig. 6.13c). Moreover, a higher electron density in the remaining volume facilitates exchange and hopping of the delocalized electrons, which lowers the effective electron mass. Hence, the two key parameters, the quantization area Ω and the effective electron mass m_{eff}, that govern the E-n dependency (cf. Eqn. 6.2) are expected to decrease during CO_2 adsorption. Consequently the slope of the dispersion relation increases with respect to pristine islands (cf. Fig. 6.8c).

6.4.2 Physisorption of Isophorone

Isophorone has a different impact on the cluster's electronic structure than CO_2, as the slope of the dispersion curve decreases in the presence of the organic molecules. Isophorone is not expected to interact strongly with gold. Its terminal oxygen, as negative charge center of the polarized molecule, will avoid the electron-rich island perimeter in order to minimize Coulomb repulsion. Conversely, the positive charge center that would benefit from Coulomb attraction to the Au anions, is localized at the C=C double bond in the molecular ring and any significant approach of the two charge centers is therefore hindered by steric repulsion imposed by the molecular side groups. Substantial Au-isophorone interaction is only expected for a dissociated molecules, i.e.

when the molecular oxygen would be stripped off and replaced by an Au atom, for instance by dissociation with an O vacancy [238]. However, IRAS data were found to be identical on gold-covered MgO/Ag(001) ultrathin films and pristine Ru(0001) that is known to bind the molecule in an associative manner (Fig. 6.12b). All the main vibrations of isophorone are equal in both cases implying that the molecule adsorbs intact, without significant dissociations. Moreover, the frequency band at 1650 cm^{-1} is assigned to the C=O double bond and remains clearly intact on both surfaces, giving a strong evidence that the molecule does not dissociate at the terminal oxygen. In absence of pronounced chemical or electrostatic interactions, the Au-molecule binding is limited to van-der-Waals forces and hydrogen-bonding ($Au^{\delta-}-H^{\delta+}$). Supporting DFT calculations on an infinite Au stripe on a 1 ML MgO/Ag(001) film, being the first approximation of a cluster rim, corroborate the assumption

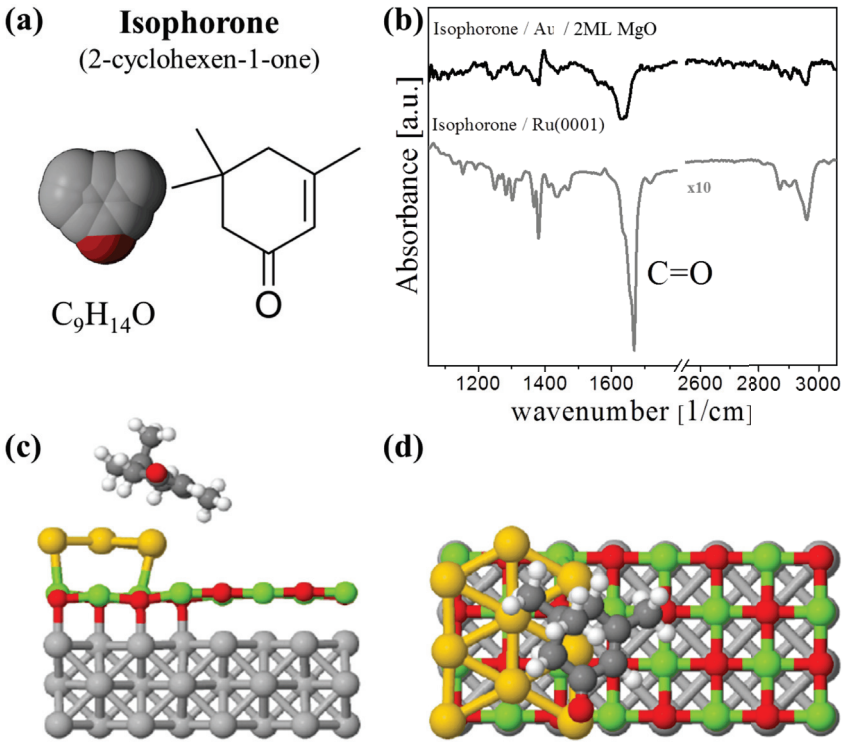

Fig. 6.12: (a) Structure and (b) IR spectra of isophorone adsorbed Au cluster on MgO/Ag(001) ultrathin films at RT (black) and Ru(0001) at liquid nitrogen temperature (gray). Similar vibrational modes are resolved in both cases, indicating that the molecule adsorbs associatively on the two surfaces. DFT calculations of isophorone on an infinite Au stripe on a 1 ML MgO/Ag(001) film in (c) top and (d) side view [238]. The orientation of the molecule in (a) corresponds to that one shown in (d). (Colors: Mg: green, O: red, C: dark gray, H: white, Au: yellow, Ag: gray)

[238]. Here, isophorone physisorbs with a large separation between Au and the molecule and its C=O double bond oriented along the infinite edge of the strip (Fig. 6.12 c,d). The adsorption energy is determined to be -0.38 eV and no charge transfer between Au and isohporone is observed.

The general weakness of such a coupling is in agreement with the easy removal of the organic molecules from the Au cluster edges, in comparison to CO_2. Furthermore, the observed alteration of the Au QWS structure points to weak, mostly dispersive coupling between isophorone and the negatively charged island rim. The decreasing slope in the *E-n* dispersion indicates a larger quantization volume or a weaker electron coupling inside the island after adsorption. Both trends can be connected to the polarization of the organic molecules that weakens the repulsive impact of the negatively-charged island perimeter and enables an expansion of the quantization region (Fig. 6.13a). As a consequence, the electron gas spreads out beyond former boundaries, i.e. the effective size of the potential well increases, which in turn reduces its effective density and closely related the probability of hopping ad exchange processes, hence the effective electron mass. Also more subtle effects may be at work, for instance a change of the potential slope at the island boundaries or a lowering

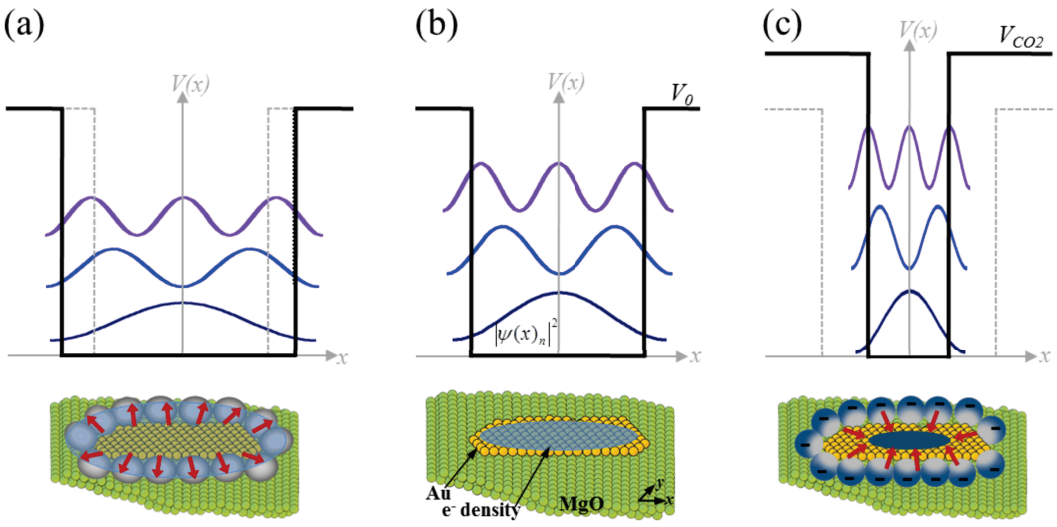

Fig. 6.13: 1D scheme showing the electron confinement in (a) an Au island with isophorone, (b) a pristine island and (c) an island with edge-bound CO_2. Attractive Au-isophorone forces promote electron spill-out in (a), which increases the size of the potential well and causes the QWS to move together. Conversely, charge transfer into the CO_2 generates a repulsive rim around the island in (c) that results in a compression of the Au electron gas and moves the QWS apart. In addition, molecular chemisorption influences the height of the confining potential.

of the potential walls that facilitates a spill-out of Au electrons in the presence of isophorone. All these concepts are well established under the synonym "interface damping" in the framework of plasmon theory, where they are used to rationalize the redshift of particle plasmons in the presence of a ligand shell [239]. The role of isophorone adsorption may thus be essentially reduced to induce a dilution of the Au electron gas, as triggered by the expansion of the confining potential. Observable consequence of this electronic perturbation is a decreasing energy separation of the Au QWS in presence of the organic entities in agreement with the decreased slope in the E-n diagram.

6.5 Conclusions

This chapter studied the binding behavior of two molecular entities to ultra-small, oxide-supported Au clusters. Thereby, the quantized electronic structure of the nanostuctures has proven to be a sensitive indicator for adsorption and charge transfer processes taking place at their surface. Strong binding of molecular ligands in the case of chemisorbed CO_2 is associated with a charge transfer out of the Au islands, resulting in a reduction of the effective confinement region of the electrons. Hence the eigenstates of the Au electronic system move apart and the dispersion of the QWS increases. Conversely, mostly dispersive coupling was observed for physisorbed isophorone, promoting electron spill out beyond former cluster boundaries. In this case, the eigenstates are squeezed together resulting in a flatter E-n dispersion relation. The perturbation of a particle electronic system by molecular adsorbates is not only of academic interest, but directly affects the understanding of heterogeneous catalysis. In many cases, ground state electronic properties are used to analyze the role of catalytic particles in chemical reactions, although their QWS structure considerably modifies during the adsorption process. The experiments demonstrate the impact of molecules on the properties of metal nanostructures on the single-particle level, providing mechanistic insight into electronically-driven chemical processes. A chemical analysis performed via IRAS elucidated further the transformation of the adsorbed gaseous CO_2 into oxalate intermediates at the rim of the nanoparticle which have got verified by supporting DFT calculations. Thus the reaction could be identified to be completely reversible which renders the investigated system as a well-suited model catalytic system to study reactions at surfaces.

Chapter 7

Summary and Outlook

In this thesis the electronic properties of oxide-supported metal nanoparticles have been exemplarily elucidated for Au clusters on MgO ultrathin films grown on a silver Ag(001) support. Starting with the investigation of the electronic structure of Au clusters with arbitrary shape, it is shown that not only the number of atoms in the cluster but also the cluster shape is of importance for the size of the HOMO-LUMO gap. Consequently, a controversially discussed question among chemists, whether the shape of nanoparticles has an influence on their reactivity, could be positively affirmed. In general, metal islands of monolayer height can be described by an approximately elliptical or parabolic shape. The linear eccentricity characterizing these mathematical objects can be used as a reliable descriptor to characterize the gap size. The energy gap decreases with increasing eccentricity and allows one to predict the gap size only by measuring the cluster's topography instead of the rather complex LT conductance traces.

The chemical reactivity of Au nanoislands on MgO/Ag(001) ultrathin films is attributed to excess charges shuttled from the underlying metal support. An alternative charging route was identified for self-doped, bulk-like CaO films containing Mo ion impurities diffused from the Mo(001) substrate. In both cases, the metal islands grow in a 2D fashion due to an enhanced metal-oxide adhesion resulting from extra electrons being localized in the cluster rim. It has been shown that, although the charge transfer to clusters arises from different origins, the overall phenomenology of clusters topography and electronic structure, e.g. the monolayer growth, the electronic quantization effects and the characteristic depression around the islands appear in a similar fashion on both oxides. Additionally, in the MgO-case the discrete electronic states in the Au nanostrcutures could be correlated to a large extent to the band structure of bulk gold. The fitted slope in the E-n dispersion of the 2D

material matches the one extracted for the LW band in the 3D band structure of bulk gold. This is quite surprising since atoms in the third dimension are completely missing in the 2D clusters. Still, the electronic properties are already equal to a large extent to 3D bulk gold. Furthermore, for the first time atomically resolved images of Au clusters on MgO/Ag(001) ultrathin films could be obtained, verifying the hexagonal arrangement of atoms in a Au(111) surface plane.

In the last chapter of the thesis, the precisely characterized QWS structure of the ad-islands were used as a "vehicle" to investigate changes in the electronic structure upon molecular adsorption. In this way, a unique insight into the nanoparticle-molecule interaction at the local level is obtained. For the first time, the electronic structure of one and the same Au cluster with and without molecules attached to its surface has been investigated. Two molecular entities were used in the experiments, weakly bound isophorone and chemisorbed CO_2. In both cases, an opposing effect on the clusters electronic structure was observed from differential conductance spectroscopy and conductance mapping data. For CO_2 adsorption, in combination with IRAS measurements and DFT calculations, the molecules were identified to be chemically activated to oxalate species. This process is driven by a charge transfer from the electron-rich cluster perimeter towards the molecules. The observed energy stretch in the QWS structure results in a reduced effective electron mass. This effect is attributed to a repulsive interaction between negatively charged adsorbates and cluster electrons, leading to a compression of the electronic density inside the nanostructure and hence to a reduction of the effective quantization area. It consequently facilitates exchange and hopping of the delocalized electrons inside the cluster and hence lowers the effective electron mass. In contrast, IRAS measurements of isophorone on MgO/Ag(001) ultrathin films covered with Au clusters and bare Ru(0001) revealed an associative adsorption of the molecule indicating a physorptive coupling of the molecules and cluster. Thereby, the molecules get polarized and increase the effective quantization area of the nanostructure. Subsequently, the spill-out of the electron cloud hinders exchange and hopping of the delocalized electron and hence increases the effective electron mass.

In a perspective one could further use scanning probe methods, such as IETS, to locally measure the vibrational modes of molecules at the clusters surface. Thereby, it should be possible to distinguish between mono-, bi- and multi-molecular species with a clear chemical fingerprint. Furthermore, also a tip-induced chemical engineering at the cluster perimeter could be accessible in the future. For example urea could be produced via co-adsorbing ammonia

and carbon dioxide having a great importance in chemical industry for the fabrication of fertilizers, feed supplements or as starting material to manufacture plastics and drugs. Moreover, the stable oxalate species may be brought in reaction with hydrogen or water to transform them into hydrocarbons. After upscaling the whole process to large scale industrial application, it would be imaginable to reduce the amount of carbon dioxide from combustion processes by transforming this unwanted greenhouse gas into useful chemicals. The proposed pathway may therefore open a possible route to solve the most dramatic environmental problem on earth in a near future.

List of Figures

List of Tables

Bibliography

[1] Bäumer, M. ; Freund, H.-J.: Metal deposits on well-ordered oxide films. In: *Progress in Surface Science* 61 (1999), S. 127

[2] Freund, H.-J.: Clusters and islands on oxides: from catalysis via electronics and magnetism to optics. In: *Surface Science* 500 (2002), S. 271

[3] Freund, H.-J.: Metal-supported ultrathin oxide film systems as designable catalysts and catalyst supports. In: *Surface Science* 601 (2007), S. 1438

[4] Freund, H.-J. ; Pacchioni, G.: Oxide ultra-thin films on metals: new materials for the design of supported metal catalysts. In: *Chemical Society Reviews* 37 (2008), S. 2224

[5] Valden, M. ; Lai, X. ; Goodman, D. W.: Onset of catalytic activity of gold clusters on titania with the appearance of nonmetallic properties. In: *Science* 281 (1998), S. 1647

[6] Haruta, M.: Catalysis of gold nanoparticles deposited on metal oxides. In: *Cattech* 6 (2002), S. 102

[7] Heer, W. A.: The physics of simple metal clusters: experimental aspects and simple models. In: *Review of Modern Physics* 65 (1993), S. 611

[8] Landman, U. ; Yoon, B. ; Zhang, Ch. ; Heiz, U. ; Arenz, M.: Factors in gold nanocatalysis: oxidation of CO in the non-scalable size regime. In: *Topics in Catalysis* 44 (2007), S. 145

[9] Hövel, H. ; Barke, I.: Morphology and electronic structure of gold clusters on graphite: scanning-tunneling techniques and photoemission. In: *Progress in Surface Science* 81 (2006), S. 53

[10] Lin, X. ; Nilius, N. ; Freund, H.-J. ; Walter, M. ; Frondelius, P. ; Honkala, K. ; Häkkinen, H.: Quantum well states in two-dimensional gold clusters on MgO thin films. In: *Physical Review Letters* 102 (2009), S. 206801

[11] Nilius, N. ; Ganduglia-Pirovano, M. V. ; Brazdova, V. ; Kulawik, M. ; Sauer, J. ; Freund, H-J.: Electronic properties and charge state of gold monomers and chains adsorbed on alumina thin films on NiAl(110). In: *Physical Review B* 81 (2010), S. 045422

[12] Ralph, D. C. ; Black, C. T. ; Tinkham, M.: Gate-voltage studies of discrete electronic states in aluminum nanoparticles. In: *Physical Review Letters* 78 (1997), S. 4087

[13] Bettac, A. ; Köller, L. ; Rank, V. ; Broer, K. H. M.: Scanning tunneling spectroscopy on deposited platinum clusters. In: *Surface Science* 402 (1998), S. 475

[14] Hövel, H. ; Barke, I.: Large noble metal clusters: electron confinement and band structure effects. In: *New Journal of Physics* 5 (2003), S. 31

[15] Libuda, J. ; Freund, H.-J.: Molecular beam experiments on model catalysts. In: *Surface Science Reports* 57 (2005), S. 157

[16] Schmid, G.: *Clusters and Colloids: From Theory to Applications*. VCH, 1994

[17] Ertl, G. ; Knoezinger, H. ; Schueth, F. ; Weitkamp, J. ; revised, 2. completly (Hrsg.) ; edition enlarged (Hrsg.): *Handbook of heterogeneous catalysis*. Wiley-VCH, 2008

[18] Sterrer, M. ; Risse, T. ; Heyde, M. ; Rust, H.-P. ; Freund, H.-J.: Crossover from three-dimensional to two-dimensional geometries of Au nanostructures on thin MgO(001) films: a confirmation of theoretical predictions. In: *Physical Review Letters* 98 (2007), S. 206103

[19] Simic-Milosevic, V. ; Heyde, M. ; Lin, X. ; König, T. ; Rust, H.-P. ; Sterrer, M. ; Risse, T. ; Nilius, N. ; Freund, H.-J. ; Giordano, L. ; Pacchioni, G.: Charge-induced formation of linear Au clusters on thin MgO films: Scanning tunneling microscopy and density-functional theory study. In: *Physical Review B* 78 (2008), S. 235429

[20] Benedetti, S. ; Myrach, P. ; Bona, A. di ; Valeri, S. ; Nilius, N. ; Freund, H.-J.: Growth and morphology of metal particles on MgO/Mo(001): a comparative STM and diffraction study. In: *Physical Review B* 83 (2011), S. 125423

[21] Shao, X. ; Prada, S. ; Giordano, L. ; Pacchioni, G. ; Nilius, N. ; Freund, H.-J.: Tailoring the shape of metal ad-particles by doping the oxide support. In: *Angewandte Chemie International Edition* 50 (2011), S. 11525–11527

[22] Shao, X. ; Nilius, N. ; Freund, H.-J.: Crossover from two- to three-dimensional gold particle shapes on CaO films of different thicknesses. In: *Physical Review B* 85 (2012), S. 115444

[23] Lemire, C. ; Meyer, R. ; S. Shaikhutdinov, H.-J. F.: CO adsorption on oxide supported Au: from small clusters to monolayer islands and three-dimensional nanoparticles. In: *Surface Science* 552 (2004), S. 27

[24] Stuck, A. ; Wartnaby, C. E. ; Yeo, Y. Y. ; Stuckless, J. T. ; Al-Sarraf, N. ; King, D. A.: An improved single crystal adsorption calorimeter. In: *Surface Science* 349 (1996), S. 229

[25] Starr, D. E. ; Campbell, C. T.: Low-temperature adsorption microcalorimetry: Pb on MgO(100). In: *Journal of Physical Chemistry B* 105 (2001), S. 3776

[26] Fischer-Wolfarth, J.-H. ; Farmer, J.A. ; Flores-Camacho, J.M. ; Genest, A. ; Yudanov, I.V. ; Rösch, N. ; Campbell, C.T. ; Schauermann, S. ; Freund, H.-J.: Particle-size dependent heats of adsorption of CO on supported Pd nanoparticles as measured with a single-crystal microcalorimeter. In: *Physical Review B* 81 (2010), S. 2414161

[27] Weinelt, M. ; Nilsson, A. ; Magnuson, M. ; Wiell, T. ; Wassdahl, N. ; Karis, O. ; Föhlisch, A. ; Martensson, N. ; Stöhr, J. ; Samant, M.: Resonant photoemission at the 2p edges of Ni: resonant raman and interference effects. In: *Physical Review Letters* 78 (1997), S. 967

[28] Weinelt, M.: Time-resolved two-photon photoemission from metal surfaces. In: *Journal of Physics - Condensed Matter* 14 (2002), S. R1099

[29] Boger, K. ; Weinelt, M. ; Fauster, T.: Scattering of hot electrons by adatoms at metal surfaces. In: *Physcal Review Letters* 92 (2004), S. 126803

[30] Binnig, G. ; Rohrer, H.: Scanning tunneling microscopy. In: *Helvetica Physica Acta* 52 (1982), S. 726

[31] Binnig, G. ; Rohrer, H.: Scanning tunneling microscopy – from birth to adolescence. In: *Review of Modern Physics* 59 (1987), S. 615

[32] Binnig, G. ; Quate, C. F. ; Gerber, C.: Atomic force microscope. In: *Physical Review Letters* 56 (1986), S. 930

[33] Rupprechter, G. ; Hayek, K. ; Hofmeister:, H.: Electron microscopy of thin-film model catalysts: activation of alumina-supported rhodium nanoparticles. In: *Journal of Catalysis* 173 (1998), S. 409

[34] Hansen, K. H. ; Worren, T. ; Stempel, S. ; Lægsgaard, E. ; M. Bäumer, H.-J. F. ; Besenbacher, F. ; Stensgaard, I.: Palladium nanocrystals on Al2O3: structure and adhesion energy. In: *Physical Review Letters* 83 (1999), S. 4120

[35] Goodman, D. W.: Model catalysts: from extended single crystals to supported particles. In: *Surface Review and Letters* 2 (1995), S. 9

[36] Campbell, C. T.: Ultrathin metal films and particles on oxide surfaces: structural, electronic and chemisorptive properties. In: *Surface Science Reports* 27 (1997), S. 1

[37] Freund, H.-J.: Introductory lecture: oxide surfaces. In: *Faraday Discussions* 114 (1999), S. 1

[38] Henry, C. R.: Surface studies of supported model catalysts. In: *Surface Science Reports* 31 (1998), S. 231

[39] Chambers, S. A.: Epitaxial growth and properties of thin film oxides. In: *Surface Science Reports* 39 (2000), S. 105

[40] Freund, H.-J. ; Kuhlenbeck, H. ; Libuda, J. ; Rupprechter, G. ; Bäumer, M. ; Hamann, H.: Bridging the pressure and materials gaps between catalysis and surface science: clean and modified oxide surfaces. In: *Topics in Catalysis* 15 (2001), S. 201

[41] Nilius, N.: Properties of oxide thin films and their adsorption behavior studied by scanning tunneling microscopy and conductance spectroscopy. In: *Surface Science Reports* 64 (2009), S. 595

[42] Freund, H.-J.: Model studies in heterogeneous catalysis. In: *Chemistry - a European Journal* 16 (2010), S. 9384

[43] Sterrer, M. ; Risse, T. ; Pozzoni, U. M. ; Giordano, L. ; Heyde, M. ; Rust, H.-P. ; Pacchioni, G. ; Freund, H.-J.: Control of the charge state of metal atoms on thin MgO films. In: *Physical Review Letters* 98 (2007), S. 096107

[44] Nilius, N. ; Ganduglia-Pirovano, M. V. ; Brazdova, V. ; Kulawik, M. ; Sauer, J. ; Freund, H.-J.: Counting electrons transferred through a thin alumina film into Au chains. In: *Physical Review Letters* 100 (2008), S. 0968021

[45] Cui, Y. ; Nilius, N. ; Shao, X. ; Baldofski, M. ; Sauer, J. ; Freund, H.-J.: Adsorption, activation and dissociation of oxygen on doped oxides. In: *Angewandte Chemie International Editon* 52 (2013), S. 11385

[46] Sauer, J.: Quantum chemistry and wavefuncwave base methods for electron correlation. In: *Block course of the International-Max-Planck-Research-School (IMPRS) "Complex Surfaces in Materials Science", Schmöckwitz, Germany*, March 1st, 2012

[47] Chen, C. J.: *Introduction to Scanning Tunneling Microscopy.* Oxford University Press, New York, Oxford, 1993

[48] Wiesendanger, R.: *Scanning Probe Microscopy and Spectroscopy: Methods and Applications.* Cambridge University Press, New York, USA, 1994

[49] Schneider, W.-D.: Scanning tunneling microscopy and spectroscopy of nanostructures. In: *Surface Science* 514 (2002), S. 74

[50] Binnig, G. ; Rohrer, H. ; Gerber, C. ; Weibel, E.: Surface studies by scanning tunneling microscopy. In: *Physical Review Letters* 49 (1982), S. 57

[51] Feenstra, R. M. ; Thompson, W. A. ; Fein, A. P.: Real-space obsevation of π-bonded chains and surface disorder on Si(111)2x1. In: *Physical Review Letters* 56 (1986), S. 608

[52] Stipe, B. C. ; Rezaei, M. A. ; Ho, W.: Single-molecule vibrational spectroscopy and microscopy. In: *Science* 280 (1998), S. 1732

[53] Coombs, J. H. ; Gimzewski, J. K. ; Reihl, B. ; Sass, J. K. ; Schlittler, R. R.: Photonemission experiments with the scanning tunneling microscope. In: *Journal of Microscopy* 152 (1988), S. 325

[54] Gimzewski, J. K. ; Reihl, B. ; Coombs, J. H. ; Schlittler, R. R.: Photon emission with the scanning tunneling microscope. In: *Zeitschrift für Physik B - Condensed Matter* 72 (1988), S. 497

[55] Berndt, R. ; Schlittler, R. R. ; Gimzewski, J. K.: Photon-emission scanning tunneling microscope. In: *Journal of Vacuum Science and Technology B* 9 (1991), S. 573

[56] Nilius, N. ; Ernst, N. ; Freund, H.-J.: Photon emission spectroscopy of individual oxide-supported silver clusters in a scanning tunneling microscope. In: *Physical Review Letters* 84 (2000), S. 3994

[57] Kliewer, J. ; Berndt, R. ; Chulkov, E.V. ; Silkin, V.M. ; Echenique, P.M. ; Crampin, S.: Dimensionality effects in the lifetime of surface states. In: *Science* 288 (2000), S. 1399

[58] Schintke, S. ; Messerli, S. ; Pivetta, M. ; Patthey, F. ; Libioulle, L. ; Stengel, M. ; Vita, A. D. ; Schneider, W. D.: Insulator at the ultrathin limit: MgO on Ag(001). In: *Physical Review Letters* 87 (2001), S. 276801

[59] Schintke, S. ; Schneider, W. D.: Insulators at the ultrathin limit: electronic structure studied by scanning tunnelling microscopy and scanning tunnelling spectroscopy. In: *Journal of Physics - Condensed Matter* 16 (2004), S. R49

[60] Repp, J. ; Meyer, G. ; Paavilainen, S. ; Olsson, F. E. ; Persson, M.: Imaging bond formation between a gold atom and pentacene on an insulating surface. In: *Science* 312 (2006), S. 1196

[61] Stiehler, C. ; Pan, Y. ; Schneider, W.-D. ; Koskinen, P. ; Häkkinen, H. ; Nilius, N. ; Freund, H.-J.: Electron quantization in arbitrarily shaped gold islands on MgO thin films. In: *Physical Review B* 88 (2013), S. 115415

[62] Crommie, M. F. ; Lutz, C. P. ; Eigler, D. M.: Imaging standing waves in a two-dimensional electron gas. In: *Nature* 363 (1993), S. 524

[63] Hasegawa, Y. ; Avouris, P.: Direct observation of standing wave formation at surface steps using scanning tunneling spectroscopy. In: *Physical Review Letters* 71 (1993), S. 1071

[64] Heller, E. J. ; Crommie, M. F. ; Lutz, C. P. ; Eigler, D. M.: Scattering and absorption of surface electron waves in qunatum corrals. In: *Nature* 369 (1994), S. 464

[65] Avouris, P. ; Lyo, I.-W.: Observation of quantum-size effects at roomtemperature on metal-surfaces with STM. In: *Science* 264 (1994), S. 942

[66] Li, J. ; Schneider, W.-D. ; Berndt, R. ; Crampin, S.: Electron confinement to nanoscale Ag islands on Ag(111): a quantitative study. In: *Physical Review Letters* 80 (1998), S. 3332

[67] Nilius, N. ; Wallis, T. M. ; Ho, W.: Development of one-dimensional band structure in artificial gold chains. In: *Science* 297 (2002), S. 1853

[68] Lee, H. J. ; Ho, W.: Single-bond formation and characterization with a scanning tunneling microscope. In: *Science* 286 (1999), S. 1719

[69] Pascual, J. I. ; Jackiw, J. J. ; Song, Z. ; Weiss, P. S. ; Conrad, H. ; Rust, H.-P.: Adsorbate-substrate vibrational modes of benzene on Ag(110) resolved with scanning tunneling spectroscopy. In: *Physical Review Letters* 86 (2001), S. 1050

[70] Pascual, J. I. ; Lorente, N. ; Song, Z. ; Conrad, H. ; Rust, H.-P.: Selectivity in vibrationally mediated single-molecule chemistry. In: *Nature* 423 (2003), S. 525

[71] Berndt, R. ; Gimzewski, J. K. ; Johansson: Inelastic tunneling excitation of tip-induced plasmon modes on noble-metal surfaces. In: *Physical Review Letters* 67 (1991), S. 3796

[72] Berndt, R. ; Gimzewski, J. K.: Injection luminescence from CdS(1120) studied with scanning tunneling microscopy. In: *Physical Review B* 45 (1992), S. 14095

[73] Qiu, X. H. ; Nazin, G. V. ; Ho, W.: Vibrationally resolved fluorescence excited with submolecular precision. In: *Science* 299 (2003), S. 542

[74] Cavar, E. ; Blüm, M.-C. ; Pivetta, M. ; Patthey, F. ; Chergui, M. ; Schneider, W.-D.: Fluorescence and phosphorescence from individual C60 molecules excited by local electron tunneling. In: *Physical Review Letters* 95 (2005), S. 196102

[75] Heinrich, A. J. ; Gupta, J. A. ; Lutz, C. P. ; Eigler, D. M.: Single-atom spin-flip spectroscopy. In: *Science* 306 (2004), S. 466

[76] Heinze, S. ; Bode, M. ; Kubetzka, A. ; Pietzsch, O. ; Nie, X. ; Blügel, S. ; Wiesendanger, R.: Real-space imaging of two-dimensional antiferromagnetism on the atomic scale. In: *Science* 288 (2000), S. 1805

[77] Wachowiak, A. ; Wiebe, J. ; Bode, M. ; Pietzsch, O. ; Morgenstern, M. ; Wiesendanger, R.: Direct observation of internal spin structure of magnetic vortex cores. In: *Science* 298 (2002), S. 577

[78] Crommie, M. F. ; Lutz, C.P. ; Eigler, D. M.: Confinement of electrons to quantum corrals on a metal surface. In: *Science* 262 (1993), S. 218

[79] Heinrich, A. J. ; Lutz, C. P. ; Gupta, J. A. ; Eigler, D. M.: Molecule cascades. In: *Science* 298 (2002), S. 1381

[80] Tersoff, J. ; Hamann, D. R.: Theory and application for the scanning tunneling Microscope. In: *Physical Review Letters* 50 (1983), S. 1998

[81] Tersoff, J. ; Hamann, D. R.: Theory of the scanning tunneling microscope. In: *Physical Review B* 31 (1985), S. 805

[82] Alemani, M.: *Low Temperature STM Investigation of Molecular Manipulation, Decoupling, and Switching*, Freie Universität Berlin, Diss., 2006

[83] Bardeen, J.: Tunneling from a many-particle point of view. In: *Physical Review Letters* 6 (1961), S. 57–59

[84] Drakova, D.: Theoretical modelling of scanning tunneling microscopy, scanning tunneling spectroscopy and atomic force microscopy. In: *Reports on Progress in Physics* 64 (2001), S. 205

[85] Castell, M. R. ; Dudarev, S. L. ; Muggelberg, C. ; Sutton, A. P. ; Briggs, G. A. D. ; Goddard, D. T.: Microscopy of metal oxide surfaces. In: *Microscopy and Microanalysis* 6 (2000), S. 324

[86] Bonnell, D. A.: Scanning tunneling microscopy and spectroscopy of oxide surfaces. In: *Progress in Surface Science* 57 (1998), S. 187

[87] Diebold, U.: The surface science of titanium dioxide. In: *Surface Science Reports* 48 (2003), S. 5

[88] Bertrams, T. ; Brodde, A. ; Neddermeyer, H.: Tunneling through an epitaxial oxide film - Al2O3 on NiAl(110). In: *Journal of Vacuum Science and Technology* 12 (1994), S. 122

[89] Bertrams, T. ; Neddermeyer, H.: Growth of NiO(100) layers on Ag(100): Characterization by scanning tunneling microscopy. In: *Journal of Vacuum Science and Technology B* 14 (1996), S. 1141

[90] Hebenstreit, W. ; Redinger, J. ; Horozova, Z. ; Schmid, M. ; Podloucky, R. ; Varga, P.: Atomic resolution by STM on ultra-thin films of alkali halides: experiment and local density calculations. In: *Surface Science* 424 (1999), S. L321

[91] Benedetti, S. ; Benia, H.M. ; Nilius, N. ; Valeria, S. ; Freund, H.-J.: Morphology and optical properties of MgO thin films on Mo(001). In: *Chemical Physics Letters* 430 (2006), S. 330

[92] Kresse, G. ; Schmid, M. ; Napetschnig, E. ; Shishkin, M. ; Köhler, L. ; Varga, P.: Structure of the ultrathin aluminum oxide film on NiAl(110). In: *Science* 308 (2005), S. 1440

[93] Kulawik, M.: *Low-Temperature Scanning Tunneling Microscopy Studies on Model Catalysis*, Humboldt-Universität zu Berlin, Diss., 2006

[94] Wu, S. W. ; Nazin, G. V. ; Chen, X. ; Qui, X. H. ; Ho, W.: Control of relative tunneling rates in single molecule bipolar electron transport. In: *Physical Review Letters* 93 (2004), S. 236802

[95] Feenstra, R. M.: Tunneling spectroscopy of the (110) surface of direct-gap III-V semiconductors. In: *Physical Review B* 50 (1994), S. 4561

[96] Viernow, J. ; Petrovykh, D.Y. ; Kirakosian, A. ; Lin, J.-L. ; Men, F. K. ; Henzler, M. ; Himpsel, F. J.: Chemical imaging of insulators by STM. In: *Physcal Review B* 59 (1999), S. 10356

[97] Raad, G. J. ; Bruls, D. M. ; Koenraad, P. M. ; Wolter, J. H.: Interplay between tip-induced band bending and voltage-dependent surface corrugation on GaAs(110) surfaces. In: *Physical Review B* 66 (2002), S. 195306

[98] Hansen, K. H. ; Worren, T. ; Laegsgaard, E. ; Besenbacher, F. ; Stensgaard, I.: Bias dependent apparent height of an Al2O3 thin film on NiAl(110) and of supported Pd clusters. In: *Surface Science* 475 (2001), S. 96

[99] Klein, J. ; Leger, A. ; Belin, M. ; Defourne, D. ; Sangster, M. J.: Inelastic-electron-tunneling spectroscopy of metal-insulator-metal junctions. In: *Physcal Review B* 7 (1973), S. 2336

[100] Li, J. ; Schneider, W.-D. ; Berndt, R. ; Bryant, O. R. ; Crampin, S.: Surface-state lifetime measured by scanning tunneling spectroscopy. In: *Physical Review Letters* 81 (1998), S. 4464

[101] Lauhon, L. J. ; Ho., W.: Effects of temperature and other experimental variables on single molecule vibrational spectroscopy with the scanning tunneling microscope. In: *Review of Scientific Instruments* 72 (2001), S. 216

[102] Pivetta, M. ; Silly, F. ; Patthey, F. ; Pelz, J. P. ; Schneider, W.-D.: Reading the ripples of confined surface-state electrons: profiles of constant integrated local density of states. In: *Physical Review B* 67 (2003), S. 193402

[103] Hong, I-P. ; Brun, C. ; Patthey, F. ; Sklyadneva, I. Y. ; Zubizarreta, X. ; Heid, R. ; Silkin, V. M. ; Echenique, P. M. ; Bohnen, K. P. ; Chulkov, E. V. ; Schneider, W.-D.: Decay mechanisms of excited electrons in quantum-well states of ultrathin Pb islands grown on Si(111): scanning tunneling spectroscopy and theory. In: *Physical Review B* 80 (2009), S. 0814091

[104] Streuer, W. ; Gross, L. ; Meyer, G.: Local thickness determination of thin insulator films via localized states. In: *Applied Physics Letters* 104 (2014), S. 231606

[105] Wachowiak, A.: *Aufbau einer 300mK Ultrahochvakuum-Rastertunnelmikroskopie-Anlage mit 14 Tesla Magnet und spinpolarisierte Rastertunnelspektroskopie an ferromagnetischen Fe-Inseln*, Universität Hamburg, Diss., 2003

[106] Haude, D.: *Rastertunnelspektroskopie auf der InAs(110)-Oberfläche: Untersuchungen an drei-, zwei- und nulldimensionalen Elektronensystemen im Magnetfeld*, Universität Hamburg, Diss., 2000

[107] Morgenstern, K. ; Braun, K.-F. ; Rieder, K.-H.: Surface-state depopulation on small Ag(111) terraces. In: *Physical Review Letters* 89 (2002), S. 226801

[108] Nilius, N. ; Wallis, T. M. ; Ho, W.: Localized molecular constraint on electron delocalization in a metallic chain. In: *Physical Review Letters* 90 (2003), S. 186102

[109] Nilius, N. ; Kulawik, M. ; Rust, H.-P. ; Freund, H.-J.: Defect-induced gap states in Al2O3 thin films on NiAl(110). In: *Physical Review B* 69 (2004), S. 121401

[110] Sterrer, M. ; Heyde, M. ; Nowicki, M. ; Nilius, N. ; Risse, T. ; Rust, H.-P. ; Pacchioni, G. ; Freundss, H.-J.: Identification of color centers on MgO(001) thin films with scanning tunneling microscopy. In: *Journal of Physical Chemistry B* 110 (2006), S. 46

[111] Hong, I.-P. ; Brun, C. ; Pivetta, M. ; Patthey, F. ; Schneider, W.-D.: Coulomb blockade phenomena observed in supported metallic nanoislands. In: *Frontiers in Physics* 1 (2013), S. 13

[112] Fulton, T. A. ; Dolan, G. J.: Observation of single-electron charging effects in small tunnel-junctions. In: *Physical Review Letters* 59 (1987), S. 109

[113] Andres, R. P. ; Bein, T. ; Dorogi, M. ; Feng, S. ; Henderson, J. I. ; Kubiak, C. P. ; Mahoney, W. ; Osifchin, R. G. ; Reifenberger, R.: Coulomb staircase at room temperature in a self-assembled molecular nanostructure. In: *Science* 272 (1996), S. 1323

[114] Mullen, K. ; Ben-Jacob, E. ; Jaklevic, R. C. ; Schuss, Z.: I-V characteristics of coupled ultrasmall-capacitance normal tunnel junctions. In: *Physical Review B* 37 (1988), S. 98

[115] Giaever, I. ; Zeller, H. R.: Superconductivity of small tin particles measured by tunneling. In: *Physical Review Letters* 20 (1968), S. 1504

[116] Lambe, J. ; Jaklevic, R. C.: Charge-quantization studies using a tunnel capacitor. In: *Physcal Review Letters* 22 (1969), S. 1371

[117] Mullen, K. ; Ben-Jacob, E. ; ; Ruggiero, S.: Charging effects in coupled superconducting tunnel junctions and their implications for tunneling measurements of high-Tc superconductors. In: *Physical Review B* 38 (1988), S. R5150

[118] Amman, M. ; Wilkins, R. ; Ben-Jacob, E. ; Maker, P. D. ; Jaklevic, R. C.: Analytic solution for the current-voltage characteristic of two mesoscopic tunnel junctions coupled in series. In: *Physical Review B* 43 (1991), S. 1146

[119] Hanna, A. E. ; Tinkham, M.: Variation of the coulomb staircase in a twojunction system by fractional electron charge. In: *Physical Review B* 44 (1991), S. 5919

[120] Wilkins, R. ; Ben-Jacob, E. ; Jaklevic, R. C.: Scanning-tunneling-microscope observations of coulomb blockade and oxide polarization in small metal droplets. In: *Physical Review Letters* 63 (1989), S. 801

[121] Averin, D. V. ; Korotkov, A. N. ; Likharev, K. K.: Theory of single-electron charging of quantum wells and dots. In: *Physical Review B* 44 (1991), S. 6199

[122] Hong, I.-P.: *Quantum Size Effects in Ultrathin Metallic Islands: A Scanning Tunneling Microscopy/Spectroscopy Study*, École Polytechnique Fedérale de Lausanne, Diss., 2009

[123] Buisset, J.: *Tieftemperatur Rastertunnelmikroskopie - Entwicklung eines hochstabilen Gerätekonzepts zur Untersuchung dynamischer Oberflächenprozesse und zur Analyse und Handhabung einzelner Atome und Moleküle zwischen 4 und 300 Kelvin*, Technische Universität Berlin, Diss., 1996

[124] Doering, M.: *Über die Abbildung und Untersuchung der Eigenschaften einzelner Adsorbate auf Metalloberflächen mittels Rastertunnelmikroskopie bei tiefen Temperaturen*, Freie Universität Berlin, Diss., 1998

[125] Rust, H.-P. ; Buisset, J. ; Schweizer, E. K. ; Cramer, L.: High precision mechanical approach mechanism for a low temperature scanning tunneling microscope. In: *Review of Scientific Instruments* 68 (1997), S. 129

[126] Rust, H.-P. ; Doering, M. ; Pascual, J. I. ; Pearl, T. P. ; Weiss, P. S.: Temperature control of a liquid helium cooled Eigler-style scanning tunneling microscope. In: *Review of Scientific Instruments* 72 (2001), S. 4393

[127] Weiss, P. S. ; Eigler, D. M. ; Binh, V. T. (Hrsg.): *What is underneath? Moving atoms and molecules to find out.* Kluwer Academic Publishers, New York, 1993

[128] Lichtenstein, Leonid: *The Structure of Two-Dimensional Vitreous Silica*, Freie Universität Berlin, Diss., 2012

[129] Melmed, A. J.: The art and science and other aspects of making sharp tips. In: *Journal of Vacuum Science and Technology* 9 (1991), S. 601

[130] Nam, A. J. ; Teren, A. ; Lusby, T. A. ; Melmed, A. J.: Benign making of sharp tips for STM and FIM: Pt, Ir, Au, Pd and Rh. In: *Journal of Vacuum Science and Technology* 13 (1995), S. 1556

[131] Henyk, M. ; Beck, K.M. ; Engelhard, M.H. ; Joly, A.G. ; Hess, W.P. ; Dickinson, J.T.: Surface electronic properties and site-specific laser desorption processes of highly structured nanoporous MgO thin films. In: *Surface Science* 593 (2005), S. 242

[132] Tegenkamp, C. ; Pfnür, H. ; Ernst, W. ; Malaske, U. ; Wollschläger, J. ; Peterka, D. ; Schröder, K.M. ; Zielasek, V. ; Henzler, M.: Defects in epitaxial insulating thin fsilms. In: *Journal of Physics: Condensed Matter* 11 (1999), S. 9943

[133] Madelung, O. ; Rössler, U. ; Schulz, M.: *Magnesium oxide (MgO) Energy Gap, Interband Transition Energies.* Bd. 41B. Landolt-Börnstein Group III: Condensed Matter, Physics and Astronomy, Springer-Verlag, 1999

[134] Colluccia, S. ; Barton, A. ; Tench, A.J.: Reactivity of low-coordination sites on the surface of magnesium oxide. In: *Journal of Chemical Society, Faraday Transactions* 77 (1981), S. 2203

[135] Hattori, H.: Solid base catalysts: generation of basic sites and application to organic synthesis. In: *Applied Catalysis A: General* 222 (2001), S. 247

[136] Bailly, M.-L. ; Chizallet, C. ; Costentin, G. ; Krafft, J.-M. ; Lauron-Pernot, H. ; Che, M.: A spectroscopy and catalysis study of the nature of active sites of MgO catalysts: thermodynamic bronsted basicity versus reactivity of basic sites. In: *Journal of Catalysis* 235 (2005), S. 413

[137] Sanchez, A. ; Abbet, S. ; Heiz, U. ; Schneider, W.-D. ; Häkkinen, H. ; Barnett, R. N. ; Landman, U.: When gold is not noble: nanoscale gold catalysts. In: *Journal of Physical Chemistry A* 103 (1999), S. 9573

[138] Abbet, S. ; Sanchez, A. ; Heiz, U. ; Schneider, W.-D. ; Ferrari, A. M. ; Pacchioni, G. ; Rösch, N.: Acetylene cyclotrimerization on supported size-selected Pd(1-30) clusters: one atom is enough! In: *Journal of American Chemical Society* 122 (2000), S. 3453

[139] Meerson, O. ; Sitja, G. ; ; Henry, C.R.: Low temperature and low pressure CO oxidation on gold clusters supported on MgO(100). In: *European Physical Journal D* 34 (2005), S. 119

[140] Yoon, B. ; Häkkinen, H. ; Landman, U. ; Wörz, A.S. ; J.-M.Antonietti ; Abbet, S. ; Judai, K. ; Heiz, U.: Charging effects on bonding and catalyzed oxidation of CO on Au8 clusters on MgO. In: *Science* 307 (2005), S. 403

[141] Hammer, B.: Special Sites at Noble and Late Transition Metal Catalysts. In: *Topics in Catalysis* 37 (2006), S. 3

[142] Volodin, A. M.: Photoinduced phenomena on the surface of wide-band-gap oxide catalysts. In: *Catalysis Today* 58 (2000), S. 103

[143] Meyerheim, H. L. ; Popescu, R. ; Kirschner, J. ; Jedrecy, N. ; Sauvage-Simkin, M. ; Heinrich, B. ; Pinchaux, R.: Geometrical and compositional structure at metal-oxide interfaces: MgO on Fe(001). In: *Physcal Review Letters* 87 (2001), S. 076102

[144] Mather, P. G. ; Read, J. C. ; Buhrman, R. A.: Disorder, defects, and band gaps in ultrathin (001) MgO tunnel barrier layers. In: *Physical Review B* 73 (2006), S. 205412

[145] Benia, H. M.: *Spatially Resolved Optical Measurements on Supported Metal Particles and Oxide Surfaces with the STM*, Humboldt-Universität zu Berlin, Diss., 2008

[146] Giordano, L. ; Cinquini, F. ; Pacchioni, G.: Tuning the surface metal work function by deposition of ultrathin oxide films: density functional calculations. In: *Physical Review B* 73 (2005), S. 045414

[147] Prada, S. ; Martinez, U. ; ; Pacchioni, G.: Work function changes induced by deposition of ultrathin dielectric films on metals: a theoretical analysis. In: *Physical Review B* 78 (2008), S. 235423

[148] Ohring, M.: *The Material Science of Thin Films.* Academic Press London, 1992

[149] Valeri, S. ; Altieri, S. ; Pennino, U. del ; Bona, A. di ; Luches, P. ; Rota, A.: Scanning Tunneling Microscopy of MgO Ultrathin Films on Ag(001). In: *Physical Review B* 65 (2002), S. 245410

[150] Ouvrard, A. ; Niebauer, J. ; Ghalgaoui, A. ; Barth, C. ; Henry, C. R. ; Bourguignon, B.: Characterization of thin MgO films on Ag(001) by low-energy electron diffraction and scanning tunneling microscopy. In: *Journal of Physical Chemistry C* 115 (2011), S. 804

[151] Wu, M.-C. ; Corneille, J.S. ; He, J.-W. ; Estrada, C.A. ; Goodman, D.W.: Synthesis and characterizations of ultrathin MgO films on Mo(001). In: *Journal of Vacuum Science and Technology A* 10 (1992), S. 1467

[152] Gallagher, M.C. ; Fyfield, M.S. ; Bumm, L.A. ; Cowin, J.P. ; Joyce, S.A.: Structure of ultrathin MgO films on Mo(001). In: *Thin Solid Films* 445 (2003), S. 90

[153] Sterrer, M. ; Fischbach, E. ; Risse, T. ; Freund, H.-J.: Geometric characterization of a singly charged oxygen vacancy on a single-crystalline MgO(001) film by electron paramagnetic resonance spectroscopy. In: *Physical Review Letters* 94 (2005), S. 186101

[154] Wollschläger, J. ; Erdös, D. ; Schröder, K.-M.: The formation of mosaics during the reactive growth of MgO films on Ag(100). In: *Surface Science* 402-404 (1998), S. 272

[155] Lide, D. R.: *Molybdenum, in CRC Handbook of Chemistry and Physics 4.* Chemical Rubber Publishing Company, 1994

[156] Chusueia, C.C. ; Meier, D.C. ; Goodman, D.W. ; Woodruff, D.P. (Hrsg.): *The Chemical Physics of Solid Surfaces: Oxide Surfaces.* Bd. 9. Elsevier, Amsterdam, 2001

[157] Kim, Y.D. ; Stultz, J. ; Goodman, D.W.: Characterization of MgO(100) thin film growth on Mo(100). In: *Surface Science* 506 (2002), S. 228

[158] Ricci, D. ; Bongiorno, A. ; Pacchioni, G. ; Landman, U.: Bonding trends and dimensionality crossover of gold nanoclusters on metal-supported MgO thin films. In: *Physical Review Letters* 97 (2006), S. 036106

[159] Pacchioni, G. ; Freund, H.-J.: Electron transfer at oxide surfaces. The MgO paradigm: from defects to ultrathin films. In: *Chemical Society Reviews* 37 (2012), S. 2224–2242

[160] Butti, G. ; Trioni, M. I. ; Ishida, H.: Electronic properties calculation of MgO thin films adsorbed on semi-infinite Ag(001). In: *Physical Review B* 70 (2004), S. 195425

[161] Smoluchowski, R.: Anisotropy of the electronic work function of metals. In: *Physical Review* 60 (1941), S. 661

[162] Lopez, N. ; Valeri, S.: MgO/Ag(001) interface structure and STM images from first principles. In: *Physical Review B* 70 (2004), S. 125428

[163] Flank, A. M. ; Delaunay, R. ; Lagarde, P. ; Pompa, M. ; Jupille, J.: Epitaxial silver layer at the MgO(100) surface. In: *Physical Review B* 53 (1996), S. 1737

[164] Giovanardi, C. ; Bona, A. di ; Moia, T. S. ; Valeri, S. ; Pisani, C. ; Sgroi, M. ; Busso, M.: Experimental and theoretical study of the MgO/Ag(001) interface. In: *Surface Science* 505 (2002), S. 209–214

[165] König, T.: *Investigation of Defects on MgO Films grown on Ag(001) - A Combined Dynamic Force and Scanning Tunneling Microscopy Study*, Technische Universität Berlin, Diss., 2010

[166] Goniakowski, J. ; Noguera, C.: Relaxation and rumpling mechanisms on oxide surfaces. In: *Surface Science* 323 (1995), S. 129

[167] Valeri, S. ; Altieri, S. ; Bona, A. D. ; Giovanardi, C. ; Moia, T. S.: Structural study of thin MgO layers on Ag(001) prepared by either MBE or sputter deposition. In: *Thin Solid Films* 400 (2001), S. 16

[168] Altieri, S. ; Tjeng, L. H. ; Sawatzky, G. A.: Electronic structure and chemical reactivity of oxide-metal interfaces: MgO(100)/Ag(100). In: *Physical Review B* 61 (2000), S. 16948

[169] Baumann, S. ; Rau, I. G. ; Loth, S. ; P., C. ; Heinrich, A. J.: Measuring the three-dimensional structure of ultrathin insulating films at the atomic scale. In: *ACS Nano* 8 (2014), S. 1739

[170] Sgroi, M. ; Pisani, C. ; ; Busso, M.: Ab initio density functional simulation of structural and electronic properties of MgO ultra-thin adlayers on the (001) Ag surface. In: *Thin Solid Films* 400 (2001), S. 64ï¿½70

[171] Tjeng, L. H. ; Vos, A. R. ; Sawatzky, G. A.: Electronic structure of MgO studied by angle-resolved ultraviolet photoelectron spectroscopy. In: *Surface Science* 235 (1990), S. 269

[172] Henrich, V. E. ; Dresselhaus, G. ; Zeiger, H. J.: Energy-dependent electron-energy-loss spectroscopy: application to the surface and bulk electronic structure of MgO. In: *Physical Review B* 22 (1980), S. 4764

[173] Cox, P.A. ; Williams, A.A.: Surface excitons on ionic crystals. In: *Surface Science* 175 (1986), S. L782

[174] Schönberger, U. ; Aryasetiawan, F.: Bulk and surface electronic structures of MgO. In: *Physical Review B* 52 (1995), S. 8788–8793

[175] Shluger, A. L. ; Sushko, P. V. ; Kantorovich, L. N.: Spectroscopy of low-coordinated surface sites: theoretical study of MgO. In: *Physical Review B* 59 (1999), S. 2417

[176] Noguera, C.: *Physics and Chemistry at Oxide Surfaces*. Cambridge University Press, 1996

[177] Finnis, M. W.: The theory of metal - ceramic interfaces. In: *Journal of Physics: Condensed Matter* 8 (1996), S. 5811

[178] Benedetti, S. ; Torelli, P. ; Valeri, S. ; Benia, H. M. ; Nilius, N. ; Renaud, G.: Structure and morphology of thin MgO films on Mo(001). In: *Physical Review B* 78 (2008), S. 195411

[179] Bordier, G. ; Noguera, C.: Electronic structure of a metal-insulator interface: Towards a theory of nonreactive adhesion. In: *Physcal Review B* 44 (1991), S. 6361

[180] Overhauser, A. W.: Bandedge detection in insulators by tunneling spectroscopy. In: *Applied Physics Letters* 54 (1989), S. 2490

[181] Ferrari, A.M. ; Casassa, S. ; Pisani, C. ; Altieri, S. ; Rota, A. ; Valeri, S.: Polar and non-polar domain borders in MgO ultrathin films on Ag(001). In: *Surface Science* 588 (2005), S. 160

[182] Benia, H. M. ; Myrach, P. ; Nilius ; Freund, H.-J.: Structural and electronic characterization of the MgO/Mo(001) interface using STM. In: *Surface Science* 604 (2010), S. 435

[183] König, T. ; Simon, G. H. ; Rust, H.-P. ; Heyde, M.: Work function measurements of thin oxide films on metals - MgO on Ag(001). In: *Journal of Physical Chemistry C* 113 (2009), S. 11301

[184] König, T. ; Simon, G.H. ; Martinez, U. ; Giordano, L. ; Pacchioni, G. ; Heyde, M. ; Freund, H.-J.: Direct measurement of the attractive interaction forces on F0 color centers on MgO(001) by dynamic force microscopy. In: *ACS Nano* 4 (2010), S. 2510

[185] Hansen, K. H. ; Sljivancanin, Z. ; Laegsgaard, E. ; Besenbacher, F. ; Stensgaard, I.: Adsorption of O2 and NO on Pd nanocrystals supported on Al2O3/NiAl(110): overlayer and edge structures. In: *Surface Science* 505 (2002), S. 25

[186] Goodman, D. W.: Catalysis: from single crystals to the real world. In: *Surface Science* 299-300 (1994), S. 837

[187] Diebold, U. ; Pan, J.-M. ; Madey, T. E.: Ultrathin metal film growth on TiO2(110): an overview. In: *Surface Science* 331-333 (1995), S. 845

[188] Freund, H.-J.: Adsorption of gases on complex solid surfaces. In: *Angewandte Chemie International Editon* 36 (1997), S. 452

[189] Wulff, G.: Zur Frage der Geschwindigkeit des Wachstums und der Auflösung der Kristallflächen. In: *Zeitschrift für Kristallographie und Mineralogie* 34 (1901), S. 449

[190] Yoon, J. G. ; Oh, H. K. ; Lee, S. J.: Growth characteristics and surface roughening of vapor-deposited MgO thin films. In: *Physical Review B* 60 (1999), S. 2839

[191] Chatain, D. ; Rivollet, I. ; Eustathopoulos, N.: Thermodynamic adhesion in nonreactive liquid metal-alumina systems. In: *Journal of Chemical Physics B* 1986 (1986), S. 561

[192] Ekardt, W.: *Metal Clusters*. Wiley, Chichester, 1999

[193] Lin, X. ; Nilius, N. ; Sterrer, M. ; Koskinen, P. ; Häkkinen, H. ; Freund, H.-J.: Characterizing low-coordinated atoms at the periphery of MgO-supported Au islands using scanning tunneling microscopy and electronic structure calculations. In: *Physical Review B* 81 (2010), S. 153406

[194] Barke, I. ; Zheng, F. ; Bockenhauer, S. ; Sell, K. ; Oeynhausen, V. v. ; Meiwes-Broer, K. H. ; Erwin, S. C. ; Himpsel, F. J.: Coverage-dependent faceting of Au chains on Si(557). In: *Physical Review B* 79 (2009), S. 155301

[195] Pacchioni, G. ; Giordano, L. ; Baistrocchi, M.: Charging of metal atoms on ultrathin MgO/Mo(100) films. In: *Physical Review Letters* 94 (2005), S. 226104

[196] Fölsch, S. ; Hyldgaard, P. ; Koch, R. ; Ploog, K. H.: Quantum confinement in monatomic Cu chains on Cu(111). In: *Physical Review Letters* 92 (2004), S. 0568031

[197] Nilius, N. ; Wallis, T. M. ; Ho, W.: Realization of a particle-in-a-box: electron in an atomic Pd chain. In: *Journal of Physical Chemistry B* 109 (2005), S. 20657

[198] Nilius, N. ; Wallis, T. M. ; Ho, W.: Tailoring electronic properties of atomic chains assembled by STM. In: *Applied Physics A* 80 (2005), S. 951

[199] Braun, K.-F. ; Rieder, K.-H.: Engineering Electronic Lifetimes in Artificial Atomic Structures. In: *Physical Review Letters* 88 (2002), S. 0968011

[200] Schouteden, K. ; Haesendonck, C. V.: Lateral quantization of two-dimensional electron states by embedded Ag nanocrystals. In: *Physical Review Letters* 108 (2012), S. 0768061

[201] Li, J. ; Schneider, W.-D. ; Crampin, S. ; Berndt, R.: Tunnelling spectroscopy of surface state scattering and confinement. In: *Surface Science* 422 (1999), S. 95

[202] Stiehler, C. ; Cui, Y. ; Nilius, N. ; Freund, H.-J.: Probing the electronic properties and charge state of gold nanoparticles on ultrathin MgO versus thick doped CaO films. In: *Physical Review B* 92 (2015), S. 075444

[203] Griffiths, D. J.: *Introduction to Quantum Mechanics*. Prentice Hall, Upper Saddle River, New Jersey, 2004

[204] Robinett, R. W.: Visualizing the solution for the circular infinite well in quantum and classical mechanics. In: *American Journal of Physics* 64 (1996), S. 440

[205] Robinett, R. W.: Quantum mechanics of the two-dimensional circular billiard plus baffle system and half-integral angular momentum. In: *European Journal of Physics* 24 (2003), S. 231

[206] Lin, X. ; Yang, B. ; Benia, H.-M. ; Myrach, P. ; Yulikov, M. ; Aumer, A. ; Brown, M.A. ; Sterrer, M. ; Bondarchuk, O. ; Kieseritzky, E. ; Rocker, J. ; Risse, T. ; Gao, H.-J. ; Nilius, N. ; Freund, H.-J.: Charge-mediated adsorption behavior of CO on MgO-supported Au clusters. In: *Journal of the American Chemical Society* 132 (2010), S. 7745–7749

[207] Koskinen, P. ; Mäkinen, V.: Density-functional tight-binding for beginners. In: *Computational Materials Science* 47 (2009), S. 237

[208] Seifert, G. ; Joswig, J.-O.: Density-functional tight binding - an approximate density-functional theory method. In: *Wiley Interdisciplinary Reviews: Computational Molecular Science* 2 (2012), S. 456

[209] *private communication with P. Koskinen and H. Häkkinen, University of Jyväkylä, Finland*

[210] Walter, M. ; Frondelius, P. ; Honkala, K. ; Häkkinen, H.: Electronic structure of MgO-supported Au clusters: quantum dots probed by scanning tunneling microscopy. In: *Physcal Review Letters* 99 (2007), S. 096102

[211] Repp, J. ; Meyer, G. ; Paavilainen, S. ; Olsson, F. E. ; Persson, M.: Scanning tunneling spectroscopy of Cl vacancies in NaCl films: strong electron-phonon coupling in double-barrier tunneling junctions. In: *Physcal Review Letters* 95 (2005), S. 225503

[212] Shell, S. L. ; Dougall, B. A. M. ; Jensen, E.: Spin splitting of an Au(111) surface state band observed with angle resolved photoelectron spectroscopy. In: *Physcal Review Letters* 77 (1996), S. 3419

[213] Li, W.-K.: A particle in an isoceles right triangle. In: *Journal Chemical Education 61, 1034* 61 (1984), S. 1034

[214] Chen, M. ; Goodman, D. W.: Catalytic active gold: From nanoparticles to ultrathin films. In: *Accounts of Chemical Research* 39 (2006), S. 739

[215] Röhlisberger, U. ; Andreoni, W.: Structural and electronic properties of sodium microclusters (n=2-20) at low and high temperatures: New insights from ab initio molecular dynamics studies. In: *Journal of Chemical Physics* 94 (1991), S. 8129

[216] *private communication with Y. Cui, Fitz-Haber-Institut der Max-Planck-Gesellschaft, Berlin*

[217] Shao, X. ; Myrach, P. ; Nilius, N. ; Freund, H. J.: Growth and morphology of calcium-oxide films grown on Mo(001). In: *Journal of Physical Chemistry C* 115 (2011), S. 8784

[218] Shao, X. ; Nilius, N. ; Myrach, P. ; Freund, H. J. ; Martinez, U. ; Prada, S. ; Giordano, L. ; Pacchioni, G.: Strain-induced formation of ultrathin mixed-oxide films. In: *Physical Review B* 83 (2011), S. 245407

[219] Binnig, G. ; Frank, K. H. ; Fuchs, H. ; Garcia, N. ; Reihl, B. ; Rohrer, H. ; Salvan, F. ; Williams, A. R.: Tunneling spectroscopy and inverse photoemission: image and field states. In: *Physcal Review Letters* 55 (1985), S. 991

[220] Häkkinen, H.: Charging of atoms, clusters, and molecules on metal-supported oxides: A general and long-ranged phenomenon. In: *Chemical Society Reviews* 37 (2008), S. 1847

[221] Repp, J. ; Meyer, G. ; Rieder, K.-H.: Snell's law for surface electrons: refraction of an electron gas imaged in real space. In: *Physical Review Letters* 92 (2004), S. 036803

[222] Pan, Y. ; Benedetti, S. ; Nilius, N. ; Freund, H.-J.: Change of the surface electronic structure of Au(111) by a monolayer MgO(001) film. In: *Physical Review B* 84 (2011), S. 075456

[223] Shaikhutdinov, S. ; Freund, H.-J.: Ultrathin oxide films on metal supports: structure-reactivity relations. In: *Annual Review of Physical Chemistry* 63 (2012), S. 619

[224] Mammen, N. ; Narasimhan, S. ; Gironcoli, S. de: Tuning the morphology of gold clusters by substrate doping. In: *Journal American Chemical Society* 133 (2011), S. 2801

[225] Stavale, F. ; Shao, X. ; Nilius, N. ; Freund, H. J. ; Prada, S. ; Giordano, L. ; Pacchioni, G.: Donor characteristics of transition-metal-doped oxides: Cr-doped MgO versus Mo-doped CaO. In: *Journal American Chemical Society* 134 (2012), S. 11380

[226] Repp, J. ; Meyer, G. ; Olsson, F. E. ; Persson, M.: Controling the charge state of individual gold atoms. In: *Science* 305 (2004), S. 493

[227] Kittel, C.: *Introduction to Solid States Physics*. Wiley, 1996

[228] Calaza, F. ; Stiehler, C. ; Fujimori, Y. ; ; Sterrer, M. ; Beeg, S. ; Ruiz-Oses, M. ; Nilius, N. ; Heyde, M. ; Parvianinen, T. ; Honkala, K. ; Häkkinen, H. ; Freund, H.-J.: Carbon dioxide activation and reduction induced by electron transfer at an oxide-metal interface. In: *Angewandte Chemie International Edition* 54 (2015), S. 1

[229] Seiferth, O ; Wolter, K. ; Dillmann, B. ; Klivenyi, G. ; Freund, H.-J. ; Scarano, D. ; Zecchina, A.: IR investigation of CO2 adsorption on chromia surfaces: Cr2O3(0001)/Cr(110) versus polycrystalline alpha-Cr2O3. In: *Surface Science* 421 (1999), S. 176

[230] Pacchioni, G.: Oxygen vacanices: the invisible agent on oxide surfaces. In: *ChemPhysChem* 4 (2003), S. 1041

[231] Preda, G. ; Pacchioni, G. ; Chiesa, M. ; Giamello, E.: Formation of CO2- radicals anions from CO2 adsorption on an electron-rich MgO surface: combined ab initio and pulse EPR study. In: *Journal of Physical Chemistry* 112 (2008), S. 19568

[232] Downing, C. A. ; Sokol, A. A. ; Catlow, C. R. A.: The reactivity of CO2 on the MgO(100) surface. In: *Physical Chemistry Chemical Physics* 16 (2014), S. 184

[233] Fujita, J. ; Martell, A. E. ; Nakamoto, K.: Infrared spectra of metal chelate compounds. VIII. Infrared spectra of Co(III) carbonato complexes. In: *Journal of Physical Chemistry* 36 (1962), S. 339

[234] *private communication with T. Parviainen, K. Honkala and H. Häkkinen, University of Jyväkylä, Finland*

[235] Paul, J. ; Hoffmann, F. M. ; Robbins, L. L.: CO and CO2 decomposition on bulk polycrystalline alkali metals. In: *Journal of Physical Chemistry* 92 (1988), S. 6967

[236] Hoffmann, F. M. ; Weisel, M. D. ; Paul, J.: The activation of CO2 by potassium-promoted Ru(001)I. FT-IRAS and TDMS study of oxalate and carbonate intermediates. In: *Surface Science* 316 (1994), S. 277

[237] R. L. Toomes, D. A. K.: Coadsorption and surface compound formation in the interaction of CO2 with K on Co1010. In: *Surface Science* 349 (1996), S. 65

[238] *private communication with J. Nevalaita, K. Honkala and H. Häkkinen, University of Jyväkylä, Finland*

[239] Kreibig, U. ; Vollmer, W.: *Optical Properties of Metal Clusters.* Springer, Berlin, 1995

Curriculum Vitae

Der Lebenslauf ist in der Online-Version aus Gründen des Datenschutzes nicht enthalten.

List of Publications

1. **C. Stiehler**, Y. Pan, W.-D. Schneider, P. Koskinen, H. Hakkinen, N. Nilius, H.-J. Freund: *Electron quantization in arbitrarily shaped gold islands on MgO thin films*, Physical Review B 88, 115415 (2013)

2. Y. Pan, Y. Cui, **C. Stiehler**, N. Nilius, H.-J. Freund: *Gold adsorption on CeO2 thin films grown on Ru(0001)*, Journal of Physical Chemistry C 116, 21879 (2013)

3. Y. Pan, N. Nilius, **C. Stiehler**, H.-J. Freund, J. Goniakowksi, C. Noguera: *Ceria nanocrystals exposing wide (100) facets: Structure and polarity compensation*, Advanced Materials Interfaces 1, 1400404 (2014)

4. Y. Cui, Y. Pan, L. Pascua, H. Qiu, **C. Stiehler**, H. Kuhlenbeck, N. Nilius, H.-J. Freund: *Evolution of the electronic structure of CaO thin films following Mo inter-diffusion at high temperature*, Physical Review B 91, 035418 (2015)

5. **C. Stiehler**, Y. Cui, N. Nilius, H.-J. Freund: *Probing the electronic properties and charge state of gold nanoparticles on ultrathin MgO versus thick doped CaO films*, Physical Review B 92, 075444 (2015)

6. F. Calaza, **C. Stiehler**, Y. Fujimori, M. Sterrer, S. Beeg, M. Ruiz-Oses, N. Nilius, M. Heyde, T. Parvianinen, K. Honkala, H. Häkkinen, H.-J. Freund: *Carbon dioxide activation and reaction induced by electron-transfer at an oxide-metal interface*, Angewandte Chemie International Edition 54, 1 (2015)

7. F. Calaza, **C. Stiehler**, Y. Fujimori, M. Sterrer, S. Beeg, M. Ruiz-Oses, N. Nilius, M. Heyde, T. Parvianinen, K. Honkala, H. Häkkinen, H.-J. Freund: *Aktivierung und Elektronentransfer-induzierte Reaktion von Kohlendioxid an einer Oxid-Metall-Grenzfläche*, Angewandte Chemie 127, 1 (2015)

8. **C. Stiehler**, F. Calaza, W.-D. Schneider, N. Nilius, H.-J. Freund: *Molecular adsorption changes the quantum structure of oxide-supported gold nanoparticles: Chemisorption versus physisorption*, Physical Review Letters 115, 0368041 (2015)

9. H.-J. Freund, C. P. O'Brien, K.H. Dostert, M. Hollerer, **C. Stiehler**, F. Calaza, S. Schauermann, S. Shaikhutdinov, M. Sterrer: *Supports and modified nano-particles in designing model catalysts*, Faraday Discussion, submitted (2015)

10. **C. Stiehler**, N. Nilius, H.-J. Freund: *Adsorption of isophorone molecules on MgO/Ag(001) thin films*, in preparation

11. **C. Stiehler**, N. Nilius, H.-J. Freund: *Gold-isophorone hybrid structures on MgO/Ag(001) thin films*, in preparation

Danksagung

Mein besonderer Dank gilt Prof. Dr. Hans-Joachim Freund für die einmalige Möglichkeit meine Doktorarbeit über ein hervorragendes Forschungsprojekt am Fritz-Haber-Institut zu verfassen. Darüber hinaus danke ich ihm zutiefst für seine persönliche Führung, für zahlreiche wissenschaftliche Diskussionen und für die ausgezeichneten Arbeitsbedingungen in einem fruchtbaren, interdisziplinären und internationalen Arbeitsumfeld.

Bei Prof. Dr. Matin Weinelt möchte ich mich ganz herzlich für die Betreuung meiner Dissertation, für die Möglichkeit meine Ergebnisse im Rahmen von Seminarvorträgen präsentieren zu können, sowie für sehr konstruktive Anregungen und Diskussionen bedanken.

Prof. Dr. Niklas Nilius bin ich zu tiefstem Dank verpflichtet für die engagierte Unterstützung meiner Forschungsarbeit, für seine sehr gute Ideen bezüglich der Messungen und Interpretation der Ergebnisse, die er trotz seines Umzuges zum Antritt einer Professur außerhalb Berlins nicht abreißen ließ und mich mit voller Leidenschaft weiter unterstützte.

Prof. Dr. Wolf-Dieter Schneider danke ich herzlichst für seine engagierte, offene und begeisterte Art und Weise wissenschaftliche Ergebnisse zu betrachten und zu präsentieren. Er stellte für mich eine wichtige Konstante in der Betreuung meiner Promotion dar, hatte immer ein offenes Ohr für mich und von seiner immensen Erfahrung im Wissenschaftszirkus konnte ich sehr viel lernen.

Dr. Markus Heyde danke ich für die Übernahme der Betreuung nach Niklas Umzug, für das mir entgegengebrachte Vertrauen sowie für die mir gegebene Freiheit mein Forschungsprojekt an der Maschine uneingeschränkt weiterführen zu können.

Dr. Fernando Stavale danke ich für die sehr gute Betreuung während meines Forschungsaufenthaltes in Rio de Janeiro, für die Einführung in neue experimentelle Techniken, für den herzlichen Empfang mit offenen Armen sowie das Nahebringen der brasilianische Arbeitsweise und Kultur.

Prof. Dr. Hannu Häkkinen und seiner Arbeitsgruppe von der University of Jyväkylä danke ich für die Unterstützung meiner Forschung durch theoretische Berechnungen.

Dr. Florencia Calaza, Dr. Yi Cui und Dr. Yi Pan danke ich für ihre unterstützenden Messungen, die mir dabei geholfen haben wichtige Erkenntnisse bezüglich meines Projektes zu erlangen. Darüber hinaus danke ich Manuela Misch für ihre Kompetenz und sehr gutes Organisationstalent und Klaus-Peter Vogelgesang für seinen technischen support und die stets rasche Anfertigung von Bauteilen in hervorragender Qualität. Ebenfalls gilt mein Dank allen Arbeitsgruppen der Abteilung Chemische Physik des Fritz-Haber-Instituts, die an dem Magnesiumoxideprojekt beteiligt waren.

Ich danke der Studienstiftung des deutschen Volkes für ein Promotionsstipendium und der International Max Planck Research School “Functional Interfaces in Physics and Chemistry” für ideelle Unterstützung.

Ich danke meinen PhD-Kollegen, Che Leandro Pascua und Arkadashim Emre Emmez, die über die Länge der Promotion mit mir gemeinsam gelitten, gezweifelt und sich immer wieder aufgerafft haben und durch das Teilen dieser Lebensphase zu engen Freunden wurden.

Zu guter Letzt möchte ich mich bei meiner Familie und Freunden bedanken, allen voran meinen Eltern, Heidi und Fritz Stiehler, die mich stets auf meinem Lebensweg begleitet, mich unterstützt und mir Türen geöffnet haben, sowie meinen Schwestern Ina-Maria, Jana, Annett und Susann. Für moralische Unterstützung während meiner Arbeit, das Teilen von Freud und Leid, danke ich meinen Freunden und Wegbegleitern Thomas, Tommy und Albina.

Selbständigkeitserklärung

Hiermit erkläre ich, dass ich die vorliegende Arbeit selbständig und nur unter Verwendung der angegebenen Quellen und Hilfsmittel angefertigt habe.

Berlin, den 16. April 2015

Christian Stiehler